博士論文（要約）

High order hyperbolic approach for diffusion dominated flows

（拡散が支配的な流れに対する高次精度双曲型解法）

CHAMARTHI AMARESHWARA SAINADH
チャマーシー　アメーレシュワーラー　サイナド

東京大学大学院工学系研究科
航空宇宙工学専攻

ACKNOWLEDGEMENTS

I am heartily thankful to my academic advisor and mentor, Prof. Kimiya Komurasaki, for his guidance and support. His unwavering support and guidance through the successes and the setbacks has made this work possible. Komurasaki Sensei's trust in my abilities has been a major contributor to my success. Thank you.

I would also like to thank my dissertation committee members: Prof. Kojiro Suzuki, Prof. Takehiro Himeno and Prof. Ikkoh Funaki for agreeing to examine my thesis and provide critical feedback on my work. I sincerely thank them for their time and assistance in refining this work.

I would also like to take this opportunity to thank Dr. Hiroyuki Koizumi, Dr. Tony Schönherr and Dr. Rei Kawashima for their suggestions during seminars, assistance, and encouragement with my research work. I sincerely thank Dr. Hiroaki Nishikawa from National Institute of Aerospace, and Prof. Taku Nonomura from Tohoku University for all the support they provided during our discussions regarding numerical schemes. Their time and effort is sincerely appreciated.

Thanks to my lab members, Florian, Bak, Wang, Hamada and Ito for numerous discussions and their valuable suggestions during the seminars. Special thanks to my friend Abhishek from India, who patiently listened to my ramblings about CFD, for the invaluable discussions. It was great sharing ideas with you.

Most of all, I want to acknowledge my parents for all their support, and my wonderful wife, Jyothi. Thank you for putting up with my constant 'I have to code or derive', late nights, and weekends. You gave up tropical climate for cold and harsh

Tokyo winters and was always on my side during these three years even when we were squeaking through at poverty level. Thank you.

Finally, I owe special thanks to Monbukagakusho Scholarship (MEXT) for sponsoring my research in Japan. It would be very difficult to complete my dissertation work without this financial assistance.

TABLE OF CONTENTS

LIST OF APPENDICES

Appendix

LIST OF FIGURES

Figure

LIST OF TABLES

Table

CHAPTER I

Introduction

In this chapter, background, previous studies in the past and the objectives of this thesis are described along with the outline.

1.1 Background

The consensus in the field of Computational Fluid Dynamics (CFD) is that the low-order methods are robust and reliable and therefore frequently employed in practical calculations. On the other hand, one can obtain a significant increase in efficiency by using the high-order method and attain better results than the low order method on a coarse and under-resolved grid but they are considered complicated and less robust.

Boundary conditions are one of the significant issues with higher-order methods as it is difficult to obtain stable and accurate boundary treatment that can work for variety of test cases. Developing a numerical scheme for anisotropic diffusion that is independent of degree of anisotropy and positivity preserving, even for moderate anisotropies, on a cartesian mesh is a considered a significant challenge.

The objective is to elucidate the advantages of higher order schemes with appropriate boundary conditions and WENO methodology for diffusion, anisotropic diffusion and advection-diffusion equations that can serve as a robust and efficient framework for other systems like incompressible and compressible Navier - Stokes, non-neutral

plasma simulations, multi-phase flows, etc. in future.

1.2 Review of Previous Work

In this section, studies carried out in the literature that are related to the current work are summarized. Numerical modeling developed for first order hyperbolic approach and anisotropic diffusion are discussed.

1.2.1 First order hyperbolic approach

Consider the one-dimensional convection-diffusion in non-dimensional form,

$$\frac{\partial u}{\partial t} + u\frac{\partial u}{\partial x} = \nu\frac{\partial^2 u}{\partial x^2}, \tag{1.1}$$

where the first-order spatial derivatives, concerning the convection process, are typically are evaluated by upwind schemes and second-order spatial derivatives, modelling the diffusion process, are computed by central schemes. A simple second order finite difference scheme for computing the second order derivatives is given by the following equation,

$$\left.\frac{\partial^2 u}{\partial x^2}\right|_{i,j} = \frac{u_{i+1,j} - 2u_{i,j} + u_{i-1,j}}{\Delta x^2} + O(\Delta x^2). \tag{1.2}$$

A radically new approach of upwind formulation for diffusion equation is introduced by Nishikawa [2] based on residual-distribution (RD) method. The mathematical strategy of this approach is to split the second order partial differential equation into a set of first-order differential equations by adding new variables, typically solution gradients, and pseudo-time advancement terms and the diffusion equation is computed as a hyperbolic system. As the equation is reformulated as a hyperbolic system, the numerical methods developed for convection process are directly applicable to the diffusion terms. This novel approach has been shown to offer several advantages over

conventional methods, like accelerated convergence for steady state solution, higher order of accuracy for both primary and gradient variables. The original approach of Nishikawa has been applied to edge-based finite volume schemes [1] and Lee et al. [3] have introduced fourth order cell-centered finite volume approach. This approach is further extended to various applications, including advection-diffusion equation by Nishikawa [4, 5, 6], compressible Navier-Stokes equation [7], magnetohydrodynamics [8], high Reynolds-number flows [9] and discontinuous coefficients [10]. The main focus of the research in literature is to obtain efficient and high-order accurate solutions on unstructured-grids.

1.2.2 Numerical methods for anisotropic diffusion

Anisotropic diffusion occurs in many physical applications in which the rate of diffusion in a certain direction can be orders of magnitude higher than the other. Thermal conductivity in fusion plasmas [11], image processing [12], biological process, and medical imaging [13] are some of the examples. Diffusion tensors can be extremely anisotropic in magnetized and high temperature plasma process, which is the area of interest in current work, and it poses a challenging problem for computational simulations. Due to extreme anisotropy, the diffusion phenomenon is effectively aligned with the magnetic field lines. Such alignment may lead to the parallel diffusion, along the magnetic field lines, coefficients being orders of magnitude, up to 10^9 in fusion plasmas, larger than perpendicular diffusion coefficient. Anisotropic thermal diffusion equation can be described as

$$\frac{\partial T}{\partial t} = \nabla.(\mathbf{D}\nabla T) + S, \tag{1.3}$$

where **T** represents temperature, **S** source term and **D** the diffusion tensor. For a two-dimensional problem the diffusion tensor is given by

$$D = \begin{bmatrix} D_{||}\cos^2(\beta) + D_{\perp}\sin^2(\beta) & \frac{1}{2}\left(D_{||} - D_{\perp}\right)\sin(2\beta) \\ \frac{1}{2}\left(D_{||} - D_{\perp}\right)\sin(2\beta) & D_{||}\sin^2(\beta) + D_{\perp}\cos^2(\beta) \end{bmatrix},$$

where β is the angle between the grid and the magnetic field lines and $D_{\perp}$ and $D_{||}$ are the perpendicular and parallel diffusion coefficients, shown in Fig. 1.1, respectively.

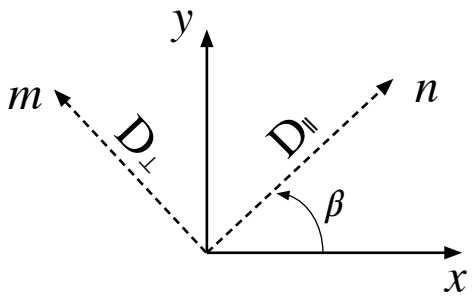

Figure 1.1: Anisotropic diffusion with parallel and perpendicular diffusion coefficients on a non-aligned grid.

These extreme anisotropies can have strict requirements on the numerical methods used to model the anisotropic diffusion and magnetohydrodynamics equations since any misalignment of the grid can lead to significant numerical diffusion in the direction perpendicular to the magnetic field lines. One approach is to solve the equations on a computational grid that is aligned with the applied magnetic field which can automatically take care of the directionality of the diffusion coefficients. This approach, known as magnetic field-aligned mesh (MFAM), has been successfully used in modeling plasma propulsion devices and fusion plasmas [14, 15]. This approach can have problems in the case of crossing field lines where local non-alignment unavoidable. Also, one has to reconstruct the mesh for problems involving time varying field lines or magnetic field induce flow and it can be cumbersome task. It is benefi-

cial to develop numerical methods that are applicable even on non-aligned grids with minimal numerical diffusion.

Gunter et al. [16] has developed "Symmetric" and "asymmetric" scheme which are simple and easy to implement with low perpendicular numerical pollution. Sovinec et al. [17] has used higher-order finite element method in the direction of larger diffusion coefficient to reduce the numerical diffusion. Van Es et al. [18] has developed second-accurate aligned finite difference method for anisotropic diffusion problems. Another important aspect of the anisotropic diffusion equation is the positivity of the temperature or space potential. A numerical scheme should be robust against the development of nonphysical negative temperatures during the simulation and must satisfy positivity and monotonicity. For example negative temperatures, in Hall thruster modeling can lead to decreased electron currents and negative Joule power density near the cathode region. Positivity has been attained by nonlinear schemes proposed in literature, imposed via limiters by Kuzmin et al.[19] and Sharma and Hammett [20], but limiters can lead to low-order spatial accuracy and are also limited to moderate anisotropies of the order $\approx 10^3$. Recently, Asymptotic preserving schemes are also proposed in literature to mitigate the issue of positivity [21, 22].

1.2.3 Hall Thruster electron fluid modelling

Electron fluid modelling in Hall thruster, an electric propulsion device shown in Fig. 1.2, is another instance where extreme anisotropies can occur. In a Hall thruster, the emitted electrons from cathode are used to ionize the neutral propellant inside the discharge chamber and also to neutralize the ion beam downstream of the thruster. A fraction of the emitted electrons enter the thruster channel and an applied magnetic field traps the electrons heading toward the anode and impedes their axial drift. These electrons ionize the neutral propellant that is fed into the annular discharge chamber through the anode. The ions are accelerated by the axial electric field thereby

producing thrust.

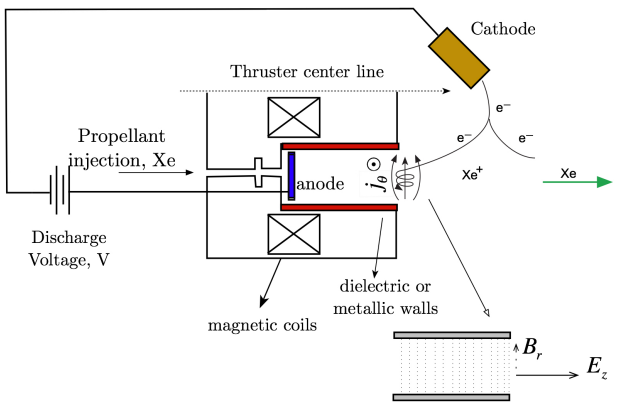

Figure 1.2: Schematic of Hall thruster working.

The applied magnetic field in Hall thruster is in such a way the that electrons are highly magnetized and constrained to the magnetic field whereas the ions are effectively unmagnetized. This important feature is the key for the design of a Hall thruster which improves the propellant utilization efficiency. Therefore, an understanding of the electron physics is important in the study of Hall thrusters [23]. The gyrating electrons that are trapped in magnetic field can have parallel mobility, $\mu_{||}$, four to five orders of magnitude larger than that is perpendicular,$\mu_{\perp}$, to the magnetic field lines [24]. Conventional approach of modelling electron fluids is by using a quasi-one-dimensional model proposed Fife [25]. Due to its limited applicability a two-dimensional field aligned approach has been developed by Mikellides et al.[26] for simulation of magnetic-shielded Hall thruster. Recently, electron fluid equations in two-dimensions are being solved by central schemes [27, 28] on a non-aligned grid. It is a well known fact that the central scheme can lead to numerical oscillations if sharp gradients are present in the flow and also this approach also suffers from poor iterative convergence due to the large disparity between $\mu_{||}$ and $\mu_{\perp}$.

As an alternative to these methods, an upwind hyperbolic-equation-system ap-

proach for two-dimensional computations has been proposed by Kawashima et al. [29] for robust calculation on a vertical-horizontal uniform mesh. While this work is a novel attempt for such problems, there are few drawbacks. The underlying scheme for the original thesis was first order upwind scheme which was highly diffusive and might require extremely fine mesh which can be computationally expensive. Their main focus was on improving diagonal dominance by avoiding cross-diffusion terms and speed of the computation and did not specifically address the issue of spurious oscillations due to misalignment of the grid and magnetic field that may occur with highly anisotropic diffusion problems on non-aligned meshes. However, mesh convergence carried out by evaluating the transverse electron flux for both the hyperbolic approach and field-aligned approach indicated that the numerical diffusion, which can be inferred as spurious oscillations, is reduced on very fine meshes. It has been proven that the hyperbolic approach attains good efficiency and accuracy in the presence of strong magnetic confinement. Kawashima et al. [30] had later extended their approach to non-isothermal system by including energy equation. They considered 3^{rd} order TVD scheme to reduce the numerical diffusion, but it will be shown in this thesis that the TVD scheme will reduce to third order linear scheme and can still have considerable numerical errors.

1.3 Objectives and Outline of this thesis

The objective of this thesis is to develop a robust and efficient hyperbolic approach for diffusion equation which can solve wide range of diffusion dominated flows. Especially, the following improvements are sought:

1. Hyperbolic approach for Diffusion and Advection-Diffusion equations:

    - Attain high-order accuracy for wide range of problems on cartesian meshes.

- Suitability of shock-capturing schemes for diffusion and numerical analysis of various boundary treatments.
- Capture sharp gradients without oscillations on under-resolved grids for advection-diffusion.

2. Development of Hyperbolic approach for Anisotropic Diffusion:

   - Extension of the hyperbolic approach and develop a robust approach.
   - Formulation that is independent of degree of anisotropy as well as angle of misalignment.
   - Verification of accuracy, order of convergence and resolution for various test cases and applicability to complex magnetic field shapes.
   - Reduce spurious oscillations due to misalignment of the grid and magnetic field
   - Non-positivity due to high-gradients and implementation of boundary conditions.

The rest of the thesis is organized as follows. In chapter-2, numerical methods employed in this study are described. A brief overview of the high order cell-centered explicit and compact upwind schemes along with shock-capturing schemes are presented.

In chapter-3, hyperbolic approach and upwind formulation of diffusion equation along with the implementation of boundary conditions are presented. The adequacy of linear upwind schemes for diffusion equation, and the effects of shock-capturing scheme like WENO and TVD methods is presented. Finally, the effects of length scale and relaxation time are investigated.

In chapter-4, the ideas developed for isotropic diffusion equation are extended to anisotropic diffusion equation and magnetized electrons. First, the test calculations

for magnetized electron equations are discussed. Effect of boundary conditions and advantages of WENO schemes over TVD schemes are clearly brought out. Numerical results are compared with those calculated by field aligned mesh and good agreement is observed. Later, an alternate and generalized hyperbolic approach along with local preconditioning approach for anisotropic diffusion equation is described. Several test cases are presented to validate the methodology, especially problems with variable diffusion tensor are investigated in detail.

In chapter-5, the first oder hyperbolic approach is extended to advection-diffusion equation. WENO approach is implemented to advection-diffusion equation by using the split hyperbolic method to demonstrate the advantage of non-oscillatory schemes to capture sharp gradients in boundary layer type problems without spurious oscillations.

Finally in chapter-6, the results of this thesis are summarized with the conclusions along with future works that can lead to further improvement and extension of the current ideas are also presented.

CHAPTER II

Numerical methods for hyperbolic conservation laws

In this chapter, a brief review of numerical methods employed in this thesis are described. Various linear and non-linear upwind schemes that are used to model the hyperbolic conservation laws are presented. Finally, the time integration scheme is explained.

2.1 Introduction

System of partial differential equations in the form of hyperbolic conservation laws are used to model many physics problems such as shallow water equations, fluid dynamics and plasma dynamics. It is difficult obtain a closed form solution of the governing equations due to their complexity, especially for applications in engineering problems. Numerical methods are often used to model these equations and among them high order conservative finite volume and finite difference schemes are most popular. Finite difference methods solve the governing equations in differential form as opposed to the finite volume methods which solve the integral form.

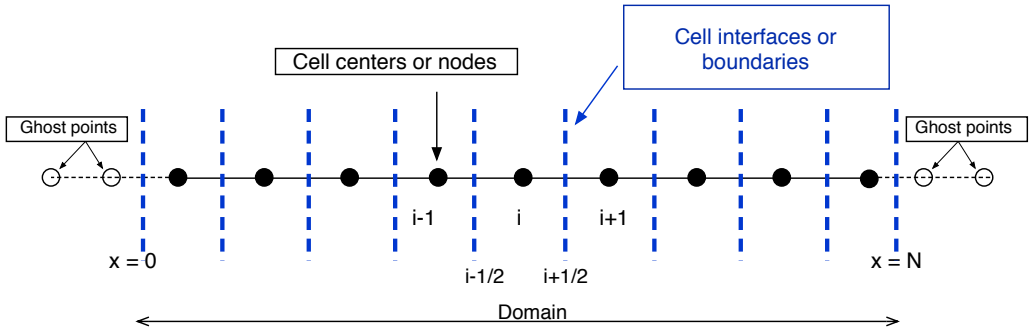

Figure 2.1: Domain discretization illustrating cell nodes, cell interfaces and ghost cells.

In the finite volume method (FVM) the cell averages are updated by computing the numerical fluxes through reconstruction polynomials. The accuracy of these numerical fluxes, computed at the cell interfaces, $i + \frac{1}{2}$, shown in Fig. 2.1, defines the accuracy of the scheme. These numerical fluxes are evaluated based on the flux Jacobian matrices and variables defined at the cell-centers. For a hyperbolic equation the upwind fluxes at the cell interfaces are constructed either by a Godunov type approximate Riemann solver(Roe [31], HLLC [32], etc.) or Boltzmann type solver, also known as flux vector splitting method (AUSM [33], Steger-Warming [34] etc.). According to the Godunov's theorem [35]: "For simulations of flows involving discontinuities and sharp gradients, Gibbs phenomenon or spurious oscillations appear in the solutions near the discontinuities if the computations are carried out by linear numerical schemes that are greater than first-order accurate".

In the last three decades, several high-order accurate schemes were developed to satisfy this criterion, and among these methods, TVD and WENO are most popular. The total-variation diminishing monotone upstream scheme for conservation laws (TVD-MUSCL) [36] is one of the popular high-order space accuracy schemes to compute the fluxes because of its simplicity and robustness. A well-known drawback

of the slope limiters that are associated with these methods is that they tend to 'clip' smooth extrema of the flow and the accuracy necessarily degenerates to first order. On the other end, WENO schemes first introduced by Jiang and Shu [37] to capture discontinuities without spurious oscillations and are also able to achieve an arbitrarily high formal order of accuracy in smooth flows. Various versions, like WENO-5M [38], WENO-3YC [39] and WENO-5Z [40], of the WENO scheme, are proposed over the years to improve the accuracy and reduce their dissipative nature. Tan and Shu [41] had also proposed high-order boundary conditions based on the WENO idea to prevent numerical oscillations contaminating the solution due to shockwaves near the boundary. Another well-known high-order method is the family of central compact schemes developed by Lele [42]. Unfortunately, the compact central schemes cannot be used in the current 'upwind' formulation for diffusion and also cannot capture the discontinuities without oscillations. Pirozzoli [43] had proposed a conservative compact upwind method in combination with WENO scheme in-order to capture discontinuities.

Recently, Ghosh and Baeder [44] has developed a class of upwind biased compact-reconstruction finite difference WENO schemes called CRWENO. This concept was extended in [45] where a positivity-preserving fifth-order finite volume compact-WENO (FVCW) scheme was developed. On the other side, an alternative approach is developed by Deng et al. [46] known as weighted compact non-linear schemes (WCNS) with similar discontinuity capturing abilities of WENO. These schemes are more flexible that we can interpolate not only fluxes [47], but also conservative variables [48], primitive variables or variables that are projected to the characteristic fields [49]. The other advantages of WCNS are that they can be used with flux difference splitting methods like Roe and HLLC and still maintain high-order of accuracy and also have good freestream and vortex preservation capabilities on curvilinear grids [50]. A comparison of WENO and WCNS is beyond the scope of this thesis and only

WENO schemes are considered for all the simulations.

2.2 Upwind Schemes

In this section, the procedures of TVD, WENO and linear upwind schemes are briefly explained. The following one-dimensional first-order partial differential equations are used for discussing the numerical schemes,

$$\frac{\partial \mathbf{Q_i}}{\partial t} + \left(\frac{\partial \mathbf{E}}{\partial x}\right)_i = 0, \tag{2.1}$$

where Q and E denote denote vector of conserved quantities and physical fluxes respectively. The subscript i denotes the variable at the ith cell center. The semi-discrete approximation, in conservative numerical method, of Eq. (2.1) is given by

$$\frac{d}{dt}Q_i^n = \frac{1}{\Delta x}\Big[\hat{E}_{i+\frac{1}{2}} - \hat{E}_{i-\frac{1}{2}}\Big], \tag{2.2}$$

where $\hat{E}_{i+\frac{1}{2}}$ are the numerical fluxes which are an approximation of physical fluxes. The numerical fluxes $E_{i+\frac{1}{2}}$ are interpolated at cell interfaces by various linear and nonlinear methods are discussed in the following sections.

2.2.1 Weighted Essentially Non-Oscillatory Schemes

The numerical fluxes requires knowledge of the values Q^R and Q^L at the cell interface. The values of Q^R and Q^L can be obtained by upwind interpolation to the same order of accuracy and also $Q^{(L)}_{i+\frac{1}{2}}$ should be biased to left and similarly $Q^{(R)}_{i+\frac{1}{2}}$ has to be biased to the right for correct upwinding as shown in Fig. 2.2. In the WENO scheme, the fifth order upwind-biased interpolation is nonlinearly weighted from three different third order interpolations on sub-stencils, S_0, S_1 and S_2, shown in Fig. 2.2.

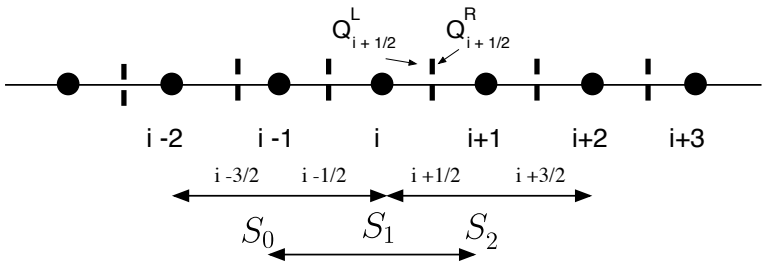

Figure 2.2: Left and right states at the cell interfaces and interpolation stencils for WENO.

For simplicity, the interpolation polynomials to the left side of the cell interface at $x_{i+\frac{1}{2}}$ are only presented here. The three third order reconstruction polynomials for variable Q are given by

$$\begin{aligned}
\bar{Q}^{(0)}_{i+\frac{1}{2}} &= \frac{1}{6}\left(2Q_{i-2} - 7Q_{i-1} + 11Q_i\right) \\
\bar{Q}^{(1)}_{i+\frac{1}{2}} &= \frac{1}{6}\left(-Q_{i-1} + 5Q_i + 2Q_{i+1}\right) \\
\bar{Q}^{(2)}_{i+\frac{1}{2}} &= \frac{1}{6}\left(2Q_i + 5Q_{i+1} - Q_{i+2}\right)
\end{aligned} \tag{2.3}$$

where $\bar{Q}^{(k)}_{i+\frac{1}{2}}$ are approximated values at cell interfaces from different sub-stencils and Q_i are the values at cell centers. In WENO literature, the variable Q can either be fluxes [47, 51], conservative variables [52], primitive variables or characteristic variables [53]. In this current work the conservative variables ($\mathbf{Q}$) are directly interpolated. The three third order upwind approximation polynomials in Eq. (2.3), are chosen dynamically by a nonlinear convex combination which adapts either to a higher order approximation in smooth regions of the solution, or to a lower-order spatial discretization that avoids reconstruction across discontinuities and provides the necessary numerical dissipation for shock capturing. The fifth order WENO scheme can be expressed as

$$\bar{Q}_{i+\frac{1}{2}} = \sum_{k=0}^{2} \omega_k Q^{(k)}_{i+\frac{1}{2}}, \tag{2.4}$$

where ω_k are the nonlinear weights which are given by,

$$\omega_k = \frac{\alpha_k}{\sum_{k=0}^{2} \alpha_k}, \; \alpha_k = \frac{\gamma_k}{(\beta_k + \epsilon)^m}, \; k = 0, 1, 2, \tag{2.5}$$

where m, γ_k and β_k are a positive integer, ideal linear weights, and smoothness indicators, respectively. $\epsilon = 10^{-6}$ is a small constant to prevent division by zero. The non-linear weights of the convex combination are based on local smoothness indicators β_k, which measure the sum of the normalized squares of the scaled L^2 norms of all derivatives of the lower order polynomials. The basic weighting strategy is to assign small weights to those lower order polynomials whose underlying stencils contain discontinuities so that an essentially non-oscillatory solution is obtained. The traditional smoothness indicators for fifth order WENO are given by Jiang, and Shu [37] denoted as WENO-JS.

$$\beta_i = \sum_{l=1}^{k} \Delta x^{2l-1} \int_{x_{i-\frac{1}{2}}}^{x_{i+\frac{1}{2}}} \left(\frac{d^l}{dx^l} p_j(x) \right)^2 dx \tag{2.6}$$

where k is the polynomial degree of $p_j(x)$. Evaluating of each k, one can obtain the following equations

$$\begin{aligned}
\beta_0 &= \frac{1}{4}\left(Q_{i-2} - 4Q_{i-1} + 3Q_i\right)^2 + \frac{13}{12}\left(Q_{i-2} - 2Q_{i-1} + Q_i\right)^2 \\
\beta_1 &= \frac{1}{4}\left(Q_{i-1} - Q_{i+1}\right)^2 + \frac{13}{12}\left(Q_{i-1} - 2\bar{Q}_i + Q_{i+1}\right)^2 \\
\beta_2 &= \frac{1}{4}\left(3Q_i - 4Q_{i+1} + Q_{i+2}\right)^2 + \frac{13}{12}\left(Q_i - 2Q_{i+1} + Q_{i+2}\right)^2
\end{aligned} \tag{2.7}$$

Borges et al. [40] proposed a new approach, denoted as WENO-5Z in this thesis, for the nonlinear weights obtained by WENO-JS as they are known to lose accuracy at critical points and are also excessively dissipative in smooth regions. The improved

non-linear weights are as follows:

$$\omega_k^z = \frac{\alpha_k^z}{\sum_{k=0}^{2} \alpha_k^z}, \quad \alpha_k^z = \gamma_k \left(1 + \left(\frac{\tau_5}{\epsilon + \beta_k}\right)^p\right), \tag{2.8}$$

where the smoothness indicators β_k's are the same as those given in Eq. (2.7), $\epsilon = 10^{-40}$, and τ_5 is the smoothness indicator of the large stencil given by,

$$\tau_5 = |\beta_0 - \beta_2| = \frac{13}{12}(Q_i'' Q_i''' \Delta x^5) + O(\Delta x^6) \tag{2.9}$$

The variable p is used to tune the dispersive and dissipative properties of the scheme. It is reported by Borges et al. [40] that the scheme becomes more dissipative when p is increased. In this thesis, $p = 2$ is employed in all test problems for diffusion and advection-diffusion equations and $p = 1$ for magnetized electron fluids. Through spectral and approximate dispersion relation (ADR) analysis, Jia et al. [54] found that the anti-dissipation of the WENO-5Z scheme is less than that of the WENO-JS scheme. They also demonstrated that the WENO-5Z scheme is not only less dissipative and dispersive but also relatively more accurate and safer. These properties of the scheme were found to be useful for magnetized electron fluid simulations discussed later.

Another variant of WENO scheme, denoted as WENO-M, that can prevent WENO-JS from losing accuracy is proposed by Henrick et al. [38]. They introduced a mapping function $g_k(\omega)$ which is defined as,

$$g_k(\omega) = \frac{\omega(\gamma_k + \gamma_k^2 - 3\gamma_k\omega + \omega^2)}{\gamma_k^2 + \omega(1 - 2\gamma_k)}, k = 0, 1, 2, \tag{2.10}$$

where γ_k's are the ideal weights and non-linear weights, ω_k, are computed by the smoothness indicators of WENO-JS. WENO-M is known to be more expensive, about 25%, than the standard WENO-JS as well as WENO-5Z scheme.

2.2.2 Linear Explicit and Compact reconstruction polynomials

For a smooth function, the fifth order WENO scheme is theoretically equivalent to the optimal fifth order linear upwind scheme, denoted as U-5E in this thesis, that is, the nonlinear weights, ω_k, are equal to the ideal linear weights, γ_k. The fifth order reconstruction formulas for left and right interfaces are given by,

$$\bar{Q}_{i+\frac{1}{2}} = \sum_{k=0}^{2} \gamma_k Q^{(k)}_{i+\frac{1}{2}},\ \gamma_0 = \frac{1}{10},\ \gamma_1 = \frac{6}{10},\ \gamma_2 = \frac{3}{10} \tag{2.11}$$

$$\begin{aligned} \bar{Q}^{(L)}_{i+\frac{1}{2}} &= \frac{1}{60}\left(2Q_{i-2} - 13Q_{i-1} + 47Q_i + 27Q_{i+1} - 3Q_{i+2}\right), \\ \bar{Q}^{(R)}_{i+\frac{1}{2}} &= \frac{1}{60}\left(-3Q_{i-1} + 27Q_i + 47Q_{i+1} - 13Q_{i+2} + 2Q_{i+3}\right). \end{aligned} \tag{2.12}$$

Similarly, third order reconstruction formulas, same as that of in Eq. (2.3), denoted as U-3E in this thesis, are given by,

$$\begin{aligned} \bar{Q}^{(L)}_{i+\frac{1}{2}} &= \frac{1}{6}\left(-Q_{i-1} + 5Q_i + 2Q_{i+1}\right) \\ \bar{Q}^{(R)}_{i+\frac{1}{2}} &= \frac{1}{6}\left(2Q_i + 5Q_{i+1} - Q_{i+2}\right). \end{aligned} \tag{2.13}$$

Finally, compact upwind reconstruction polynomials are also implemented the, denoted as U-5C in this thesis, given by Eq. (2.14). Compact schemes are a family of reconstruction schemes which are implicit in space and therefore requires an inversion of a tridiagonal matrix. They are characterized by high spectral resolution and have significantly lower dispersion errors compared to that of non-compact schemes. Implementation of the boundary conditions is same as that of the non-compact schemes.

$$\frac{1}{2}\bar{Q}^L_{i-\frac{1}{2}} + \bar{Q}^L_{i+\frac{1}{2}} + \frac{1}{6}\bar{Q}^L_{i+\frac{3}{2}} = \frac{1}{18}Q_{i-1} + \frac{19}{18}Q_i + \frac{5}{9}Q_{i+1} \tag{2.14a}$$

$$\frac{1}{6}\bar{Q}^R_{i-\frac{1}{2}} + \bar{Q}^R_{i+\frac{1}{2}} + \frac{1}{2}\bar{Q}^R_{i+\frac{3}{2}} = \frac{5}{9}Q_i + \frac{19}{18}Q_{i+1} + \frac{1}{18}Q_{i+2} \tag{2.14b}$$

In general, the integrals of the fluxes are discretized using a high-order Gaussian quadrature with suitable Gaussian integration points over the faces of the control volume[55, 56] to achieve higher order accuracy in, third order or more, multidimensional finite volume method. In the present hyperbolic approach, the fluxes are no longer non-linear and are same as that of the conservative variables. Due to this, finite volume method can also obtain higher order accuracy by using point values and reconstruction of the fluxes at Gaussian quadrature points is not necessary. Therefore, we cannot distinguish the difference between cell-centered finite volume and finite difference schemes for the flux computation. In fact, we also computed the fluxes by WCNS in [57] and the results are identical.

2.2.3 Total variation diminishing schemes

Several TVD schemes are proposed in the literature for shock-capturing and preventing Gibbs oscillations. Two of the popular approaches are considered here. First one is the van Leer's standard TVD-MUSCL [36] reconstruction for the left and right interfaces, $\bar{Q}^L_{i+\frac{1}{2}}$ and $\bar{Q}^R_{i+\frac{1}{2}}$, are given by,

$$\begin{aligned}
\bar{Q}^L_{i+\frac{1}{2}} &= Q_i + \frac{1}{4}\left((1-\kappa)\phi(r^L)(Q_i - Q_{i-1}) + (1+\kappa)\phi\left(\frac{1}{r^L}\right)(Q_{i+1} - Q_i)\right), \\
\bar{Q}^R_{i+\frac{1}{2}} &= Q_{i+1} - \frac{1}{4}\left((1-\kappa)\phi(r^R)(Q_{i+2} - Q_{i+1}) + (1+\kappa)\phi\left(\frac{1}{r^R}\right)(Q_{i+1} - Q_i)\right),
\end{aligned} \tag{2.15}$$

where κ is a free parameter which is set to 1/3 for the third-order limiter and

$$\begin{aligned} r_i^L &= \frac{Q_{i+1} - Q_i}{Q_i - Q_{i-1} + \epsilon}, \\ r_i^R &= \frac{Q_{i+1} - Q_i}{Q_{i+2} - Q_{i+1} + \epsilon}, \end{aligned} \tag{2.16}$$

where ϵ is a small value 10^{-16}. In this thesis we considered minmod and van Leer limiters which are given by

$$\begin{aligned} \phi_{minmod} &= min(r, 1), \\ \phi_{vanLeer} &= \frac{2r}{1+r}. \end{aligned} \tag{2.17}$$

Second approach is that of Cockburn and Shu [58] which can be considered as Generalized MUSCL and is popular in discontinuous Galerkin methods. For $k = \frac{1}{3}$, the Eq. (2.15) will reduce to third order linear recosntruction formula, Eq. (2.13), if limiters are not considered. Now we define,

$$\tilde{Q}_i = Q^-_{i+1/2} - Q_i, \quad \tilde{Q}_{i+1} = Q^+_{i+1/2} - Q_{i+1}. \tag{2.18}$$

Then, by using the definition of minmod limiter we can obtained a generalized limiter for 3 points

$$\tilde{Q}_i^{mod} = \text{minmod}\left(\tilde{Q}_i, Q_i - Q_{i-1}, Q_{i+1} - Q_i\right), \tag{2.19}$$

where the minmod function defined as

$$\text{minmod}(a,b,c) = \begin{cases} sign(a)\min(|a|,|b|,|c|) & \text{if } sign(a) = sign(b) = sign(c) \\ 0 & \text{otherwise} \end{cases} \tag{2.20}$$

2.3 Time discretization

After discretizing the spatial derivative, the set of ordinary differential equations obtained are,

$$\mathbf{Q_t} = \mathbf{Res}(\mathbf{Q}), \tag{2.21}$$

where the operator $Res(Q) = E'_x$ and E'_x is approximated by linear upwind polynomials or WENO scheme. For time integration the following third order TVD Runge-Kutta method [37] is used

$$\begin{aligned} \mathbf{Q^{(1)}} &= \mathbf{Q^n} + \Delta t Res(\mathbf{Q^n}) \\ \mathbf{Q^{(2)}} &= \frac{3}{4}\mathbf{Q^n} + \frac{1}{4}\mathbf{Q^{(1)}} + \frac{1}{4}\Delta t Res(\mathbf{Q^{(1)}}) \\ \mathbf{Q^{n+1}} &= \frac{1}{3}\mathbf{Q^n} + \frac{2}{3}\mathbf{Q^{(2)}} + \frac{2}{3}\Delta t Res(\mathbf{Q^{(2)}}). \end{aligned} \tag{2.22}$$

A fourth order non-TVD Runge-Kutta scheme can also be employed for the computations. Numerical results obtained by Eq. (2.22) are only presented in this thesis. The verification of numerical schemes presented in this chapter are discussed in Appendix. A.

CHAPTER III

Hyperbolic approach for Diffusion equation

In this chapter, the construction of first order hyperbolic approach for diffusion and the implementation of high-order numerical schemes on uniform cartesian meshes is presented. Schemes are validated for different types of boundary conditions and problem settings. Implementation of numerical boundary conditions through ghost cells is the key idea. Results indicate that the significant improvement in accuracy and speed can be obtained through hyperbolic approach.

3.1 Governing equation and construction of hyperbolic scheme

In this section, the construction of hyperbolic approach for diffusion equation is explained. Consider the following diffusion equation in two dimensions,

$$\frac{\partial u}{\partial t} - \nu \left(\frac{\partial^2 u}{\partial x^2} + \frac{\partial^2 u}{\partial y^2} \right) = -S, \tag{3.1}$$

where ν is the diffusion coefficient and S is the source term. In the original idea of Nishikawa [2], new variables representing the gradients of the primary variable are introduced, and the original diffusion equation has been converted into a system of three coupled first-order equations. By defining new variables $p = \frac{\partial u}{\partial x}$ and $q = \frac{\partial u}{\partial y}$, and introducing pseudo-time terms one can obtain the following first order hyperbolic

system:

$$\begin{aligned} \frac{\partial u}{\partial \tau} - \nu\frac{\partial p}{\partial x} - \nu\frac{\partial q}{\partial y} &= -S, \\ \frac{\partial p}{\partial \tau} - \frac{\partial u}{\partial x} &= -p, \\ \frac{\partial q}{\partial \tau} - \frac{\partial u}{\partial y} &= -q. \end{aligned} \tag{3.2}$$

It is important to state the fact that the first-order system reduces to the diffusion equation at the steady state, i.e. the pseudo-time terms will be zero at steady state,

$$\begin{cases} \cancel{\frac{\partial u}{\partial \tau}} - \nu\frac{\partial p}{\partial x} - \nu\frac{\partial q}{\partial y} = -S, \\ \cancel{\frac{\partial p}{\partial \tau}} - \frac{\partial u}{\partial x} = -p, \\ \cancel{\frac{\partial q}{\partial \tau}} - \frac{\partial u}{\partial y} = -q. \end{cases} \rightarrow \begin{cases} 0 = \nu\left(\frac{\partial p}{\partial x} + \frac{\partial q}{\partial y}\right) - S, \\ \frac{\partial u}{\partial x} = p, \\ \frac{\partial u}{\partial y} = q. \end{cases} \rightarrow 0 = \nu\left(\frac{\partial^2 u}{\partial x^2} + \frac{\partial^2 u}{\partial y^2}\right) - S. \tag{3.3}$$

The equations (3.2) can be represented in vector form as,

$$\frac{\partial \mathbf{Q}}{\partial \tau} + \frac{\partial \mathbf{E_x}}{\partial x} + \frac{\partial \mathbf{E_y}}{\partial y} = \mathbf{S}, \tag{3.4}$$

where the conservative variables, fluxes in x and y-direction and source terms are,

$$\mathbf{Q} = \begin{bmatrix} u \\ p \\ q \end{bmatrix}, \quad \mathbf{E_x} = \begin{bmatrix} -\nu p \\ -u \\ 0 \end{bmatrix}, \quad \mathbf{E_y} = \begin{bmatrix} -\nu q \\ 0 \\ -u \end{bmatrix}, \quad \mathbf{S} = \begin{bmatrix} -S \\ -p \\ -q \end{bmatrix}, \tag{3.5}$$

respectively. The Jacobian matrices, $\mathbf{J_x}$ and $\mathbf{J_y}$, in the x- and y-directions and the corresponding eigenvalues,λ, are given by

$$\mathbf{J}_x = \sqrt{\nu}\begin{pmatrix} 0 & -1 & 0 \\ -1 & 0 & 0 \\ 0 & 0 & 0 \end{pmatrix}, \quad \mathbf{J}_y = \sqrt{\nu}\begin{pmatrix} 0 & 0 & -1 \\ 0 & 0 & 0 \\ -1 & 0 & 0 \end{pmatrix}, \quad \lambda = \pm\sqrt{\nu}, 0. \tag{3.6}$$

In steady state, the diffusion equation will reduce to Laplace's or Poisson's equation. By replacing the primary variable u with ϕ, space potential, the hyperbolic formulation can be used to model many physics problems that are time independent. By using the right, $\mathbf{R}$, and left, $\mathbf{L}$, eigenvectors of Jacobian matrices, and the diagonal eigenvalue matrix, $|\mathbf{\Lambda}|$, the absolute Jacobian or the Roe matrix in x-direction, $|\mathbf{J_{dx}}|$, can be written as,

$$|\mathbf{J}_{dx}| = \mathbf{R_x}|\mathbf{\Lambda}|\mathbf{L_x} = \sqrt{\nu}\begin{pmatrix} 1 & 0 & 0 \\ 0 & 1 & 0 \\ 0 & 0 & 0 \end{pmatrix}. \tag{3.7}$$

Finally, the upwind flux in the x-direction can be expressed as Eq. (3.8),

$$\begin{aligned} \hat{E}_{i+\frac{1}{2},j} &= \frac{1}{2}(\mathbf{E_L} + \mathbf{E_R}) - \frac{1}{2}|\mathbf{J_{dx}}|(\mathbf{Q_R} - \mathbf{Q_L}) \\ &= \frac{1}{2}\begin{pmatrix} -(p_R + p_L) \\ -(u_R + u_L) \\ 0 \end{pmatrix} - \frac{\sqrt{\nu}}{2}\begin{pmatrix} 1 & 0 & 0 \\ 0 & 1 & 0 \\ 0 & 0 & 0 \end{pmatrix}\begin{pmatrix} u_R - u_L \\ p_R - p_L \\ q_R - q_L \end{pmatrix}. \end{aligned} \tag{3.8}$$

where the left and right fluxes, $\mathbf{E_L}$ and $\mathbf{E_R}$, are defined at the cell interfaces which are evaluated by the interpolation polynomials that are discussed later.

3.1.1 Homogeneity and flux vector splitting

Interestingly, the hyperbolic form of the diffusion equation (3.2) satisfy the homogeneity property,

$$\mathbf{E}(Q) = \frac{\partial \mathbf{E}}{\partial \mathbf{Q}}Q = J(\mathbf{Q})Q. \tag{3.9}$$

The proof of this property is easy to notice. By multiplying the Jacobian matrices shown in Eq. (3.6) by the vector Q one can reproduce the flux vector E(Q). This remarkable property of the hyperbolic form can be used to solve the diffusion equation by employing Flux vector splitting schemes. For example, in the hyperbolic approach

of Kawashima et al. [29] the upwind fluxes are computed by using Steger-Warming [34] flux vector splitting scheme, shown in Eq. (3.10)

$$\mathbf{E} = \mathbf{E}^{+} + \mathbf{E}^{-}, \tag{3.10}$$

with,

$$\begin{aligned} \mathbf{E}^{+} &= \mathbf{J}^{+}Q = (R\Lambda^{+}L)Q, \\ \mathbf{E}^{-} &= \mathbf{J}^{-}Q = (R\Lambda^{-}L)Q. \end{aligned} \tag{3.11}$$

where $\mathbf{J}^{+}$ and $\mathbf{J}^{-}$ in x-direction are expressed as follows,

$$\mathbf{J}_x^{+} = \begin{pmatrix} \frac{1}{2} & \frac{1}{2} & 0 \\ \frac{1}{2} & \frac{1}{2} & 0 \\ 0 & 0 & 0 \end{pmatrix}, \quad \mathbf{J}_x^{-} = \begin{pmatrix} \frac{-1}{2} & \frac{1}{2} & 0 \\ \frac{1}{2} & \frac{-1}{2} & 0 \\ 0 & 0 & 0 \end{pmatrix}. \tag{3.12}$$

$$\mathbf{J}_y^{+} = \begin{pmatrix} \frac{1}{2} & 0 & \frac{1}{2} \\ \frac{1}{2} & 0 & \frac{1}{2} \\ 0 & 0 & 0 \end{pmatrix}, \quad \mathbf{J}_y^{-} = \begin{pmatrix} -\frac{1}{2} & 0 & \frac{1}{2} \\ \frac{1}{2} & 0 & -\frac{1}{2} \\ 0 & 0 & 0 \end{pmatrix}. \tag{3.13}$$

and Λ^{+} is the diagonal matrix of positive eigenvalues, and Λ^{-} is the diagonal matrix of negative eigenvalues. The Jacobian matrices satisfy, $\mathbf{J}^{+} + \mathbf{J}^{-} = \mathbf{J}$ and the reconstruction for $\mathbf{E}^{+}$ uses a biased stencil with one more point to the left, and that for $\mathbf{E}^{-}$ uses a biased stencil with one more point to the right, to obey correct upwinding. In the current upwind formulation for diffusion equation, there is no difference between flux vector splitting and Roe solver. Other Riemann solvers generally used for Euler equations like HLL and Rusanov can also be used for the simulations. For the first order approach for diffusion, HLL scheme is same as that of the Rusanov scheme and would lead to less accurate results than Roe method due to too much dissipation, especially in gradient variables $\mathbf{p}$ and $\mathbf{q}$. All the simulations are carried out by Roe fluxes unless otherwise stated.

3.2 Boundary Conditions

In this section, the implementation of boundary conditions for the hyperbolic system is described. Two different approaches are employed for the numerical boundary conditions: weak and strong boundary condition. Strong boundary conditions are employed through ghost cells. In the hyperbolic approach the Neumann boundary conditions are also implemented as Dirichlet boundary condition through the gradient variables, and therefore only Dirichlet boundary conditions are described.

3.2.1 Weak boundary formulation

The Dirichlet boundary condition $u = u_0$ at, say, $x = 0$ can be implemented through the numerical flux by weak boundary condition as described by Nishikawa and Roe [59]. For a one-dimensional problem, the upwind flux in **x**-direction is given by,

$$\begin{aligned} E_{i+\frac{1}{2},j} &= \frac{1}{2}(\mathbf{E_L} + \mathbf{E_R}) - \frac{1}{2}|\mathbf{J_{dx}}|(\mathbf{Q_R} - \mathbf{Q_L}) \\ &= \frac{1}{2}\begin{pmatrix} -(p_R + p_L) \\ -(u_R + u_L) \end{pmatrix} - \frac{1}{2}\begin{pmatrix} 1 & 0 \\ 0 & 1 \end{pmatrix}\begin{pmatrix} u_R - u_L \\ p_R - p_L \end{pmatrix}. \end{aligned} \tag{3.14}$$

$$E_{x=0} = E_{\frac{1}{2}} = \frac{1}{2}(E_L + E_R) - \frac{1}{2}|J_x|(Q_R - Q_L), \tag{3.15}$$

where $(u_R,\ p_R)$ are given by a higher order interpolation from the interior of the domain, and the left state $(u_L,\ p_L)$ is specified by the boundary condition:

$$(u_L, p_L) = (u_0, p_R). \tag{3.16}$$

Set $p_L = p_R$, since the value of gradient variable is not known . This approach is consistent with the characteristic condition at $x = 0$. One can specify only one condition in hyperbolic approach only one wave enters the domain as shown in Fig.

3.1. For a Neumann boundary condition, say $p = p_0$, the value of p is specified instead of u:

$$(u_L, p_L) = (u_R, p_0). \tag{3.17}$$

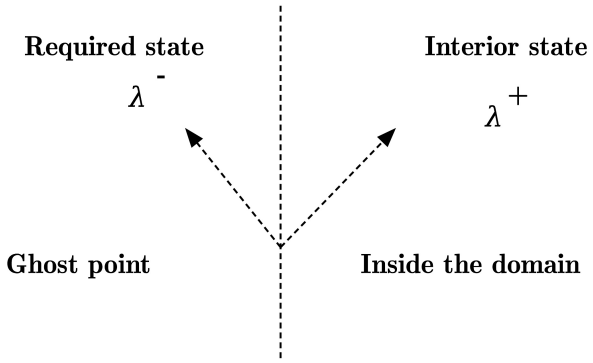

Figure 3.1: Characteristic waves at the boundary for hyperbolic approach.

3.2.2 Strong boundary: Lagrange type extrapolation for ghost cells

In this approach, an additional "ghost cells" are introduced by extending the physical domain. Unlike the weak boundary condition, the Dirichlet boundary condition is employed at the cell interface as shown in Fig. 3.2. The number of ghost-cells depends on the interior interpolation scheme and cell-interface to cell-center Lagrange extrapolation formula given by Eq. (3.18) is used to compute the values in ghost cells:

$$u^{(r)}_{\frac{1}{2}}(x) = \sum_{j=0}^{k} u_{i-r+j} C_{rj}(x), \tag{3.18}$$

where r is the order of the Lagrange polynomial and the constants C_{rj} are obtained by,

$$C_{rj}(x) = \prod_{\substack{l=0 \\ l \neq j}}^{k} \frac{x - x_{i-r+l}}{x_{i-r+j} - x_{i-r+l}}. \tag{3.19}$$

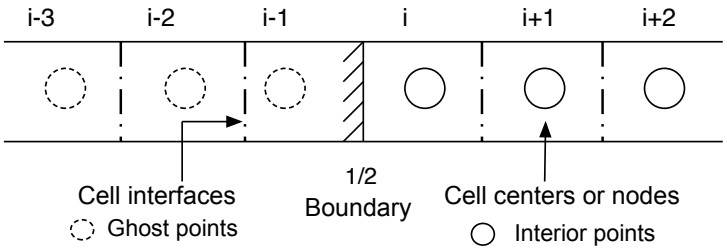

Figure 3.2: Ghost cell approach showing Dirichlet boundary condition.

Primary variable u

For Dirichlet boundary condition, where the value of u is prescribed at the cell interface, say $u_{\frac{1}{2}}$, one can extrapolate the ghost cell values by using third order accurate polynomial given by Eq. (3.20).

$$u_0 = -2u_1 + \frac{1}{3}u_2 + \frac{8}{3}u_{\frac{1}{2}}. \tag{3.20}$$

Similarly, fifth order extrapolation formula is given by Eq. (3.21).

$$u_{i+1/2} = \frac{1}{128}\left(35u_i + 140u_{i+1} - 70u_{i+2} + 28u_{i+3} - 5u_{i+4}\right), \tag{3.21}$$

where $i = 0$.

Gradient variables p **and** q

For the gradient variable, p and q, the values in ghost cells are extrapolated by using the interior points by cell-center to cell-center extrapolation [60, 61]. Such extrapolation is also consistent with the outgoing characteristics at the boundary as shown in Figure. 3.1. Lagrange extrapolation can be approximated by a (s-k)th order Taylor expansion

$$u_j = \sum_{k=o}^{s-1} \frac{(x_j - 1)^k}{k!} u_R^{(k)}, \tag{3.22}$$

where $u_R^{(k)}$ is a (s-k)th order approximation of $\frac{\partial^k u}{\partial x^k}$ at x = 1. If $u(x)$ is smooth near

the boundary, $u_R^{(k)}$ can be obtained by

$$u_R^{(k)} = \frac{d^k P_{s-1}(x)}{dx^k} \tag{3.23}$$

where $P_{s-1}(x)$ is a Lagrange polynomial of degree at most $s-1$. A general formula is given by Eq. (3.24)

$$\sum_{k=0}^{r} \frac{r!}{k!(r-k)!}(-1)^k p_{j-k} = 0, \quad j = N+1, ..., N+3 \tag{3.24}$$

For example, At the boundary, say $x = 0$, the values of ghost cell p_0 approximated by 3^{rd} and 5^{th} order extrapolations are given by equations (3.25),

$$\begin{aligned} p_0 &= 3p_1 - 3p_2 + p_3 \\ p_0 &= 5p_1 - 10p_2 + 10p_3 - 5p_4 + p_5 \end{aligned} \tag{3.25}$$

3.3 Numerical tests

In the chapter only linear problems are considered and therefore the fluxes are no longer non-linear and are same as that of the conservative variables. Due to this, finite volume schemes can also obtain higher order accuracy by using point values and reconstruction of the fluxes at Gaussian quadrature points is not necessary. Therefore, one cannot distinguish the difference between cell-centered finite volume and finite difference schemes for the flux computation. In this chapter only on the standard finite volume schemes are considered unless otherwise stated.

For the examples considered here, the numerical solutions are computed by the standard 2^{nd} order central scheme using successive over relation for comparison. For the linear upwind schemes, depending on the order of the interior scheme the corresponding r^{th} order extrapolation polynomial is used for the numerical boundary

conditions. Only strong and weak boundary procedures are implemented for the hyperbolic form of diffusion equation. The implementation of interpolation polynomials beyond 5^{th} order are straightforward and are not presented here.

3.3.1 One-dimensional test cases

Example 3.1. To investigate the implementation and accuracy of the numerical schemes the following one-dimensional diffusion equation including a source term is considered with the domain size of $x \in [0,1]$.

$$\frac{\partial u}{\partial \tau} = \nu \frac{\partial^2 u}{\partial x^2} + A \cos\left(2\pi N \frac{x}{L}\right), \tag{3.26}$$

where $\nu = 1$ and Dirichlet boundary conditions, $u_1 = 2, u_N = 1$, are considered. The exact solution for u is given by:

$$u_e = -\left(\frac{L}{2\pi C}\right)^2 A \cos\left(2\pi C \frac{x}{L}\right) + \frac{u_N - u_1}{L} x + A\left(\frac{L}{2\pi C}\right)^2 + u_1. \tag{3.27}$$

where the constants and A and C are assumed to be 10.0 and 3.0 respectively. The equivalent first order hyperbolic equation system can be written as follows:

$$\begin{aligned} \frac{\partial u}{\partial \tau} - \frac{\partial p}{\partial x} &= -A cos(\frac{2\pi N x}{L}), \\ \frac{\partial p}{\partial \tau} - \frac{\partial u}{\partial x} &= -p. \end{aligned} \tag{3.28}$$

where the conservative variables are denoted by $\mathbf{Q} = [\ u,\ p]$ and the flux vector is denoted by $\mathbf{E} = [-p, -u]$ respectively. The Jacobian matrix and the corresponding eigenvalues for the above system of equations is,

$$A(\underline{\mathbf{Q}}) = \frac{\partial \mathbf{E}}{\partial \mathbf{Q}} = \begin{bmatrix} \frac{\partial f_1}{\partial q_1} & \frac{\partial f_1}{\partial q_2} \\ \frac{\partial f_2}{\partial q_1} & \frac{\partial f_2}{\partial q_2} \end{bmatrix} = \begin{bmatrix} 0 & -1 \\ -1 & 0 \end{bmatrix} \quad ; \lambda_1 = -1, \lambda_2 = 1. \tag{3.29}$$

The right and left eigenvectors can be used to compute the absolute flux Jacobian

$$|\mathbf{J}_x| = R|\Lambda|L = \begin{bmatrix} 1 & 0 \\ 0 & 1 \end{bmatrix} \tag{3.30}$$

The simulations are conducted with grid refinements from $N = 24$ to 384 by second-order central, and all the upwind schemes which includes TVD and WENO schemes. For upwind schemes, the numerical solution is computed by an explicit time-marching until the residuals are dropped below 10^{-12} in L_1 norm with a constant CFL $= 0.65$. Figure 3.3 shows the solutions contours of various schemes in comparison with the analytical solution for both primary and gradient variable. L_2 error convergence results are shown in Fig. 3.4(a) and Fig. 3.4(b) for the solution and the gradient variables respectively.

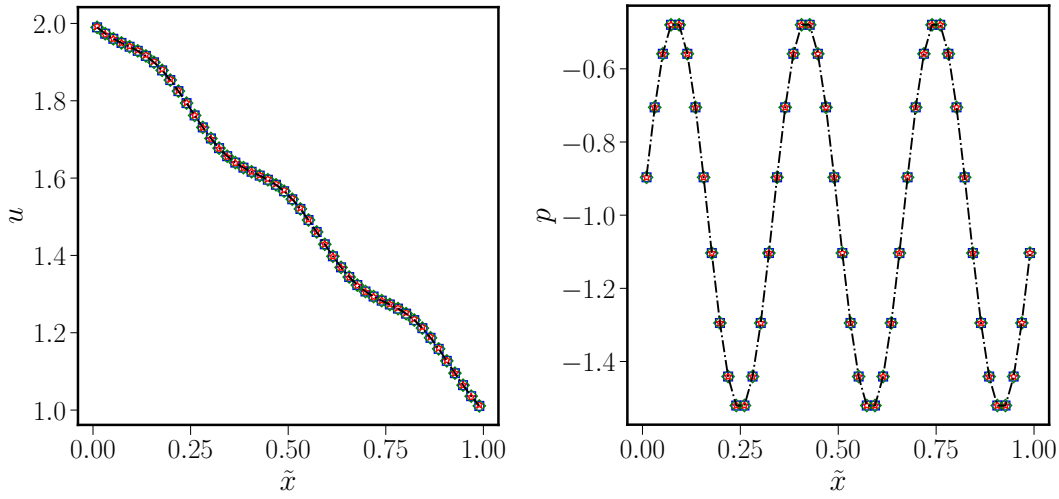

(a) Primary variable

(b) Gradient variable

Figure 3.3: Example 3.1 using different schemes. Dashed line: analytical; red stars: U-3E; blue squares: U-5C; magenta diamonds: U-5E.

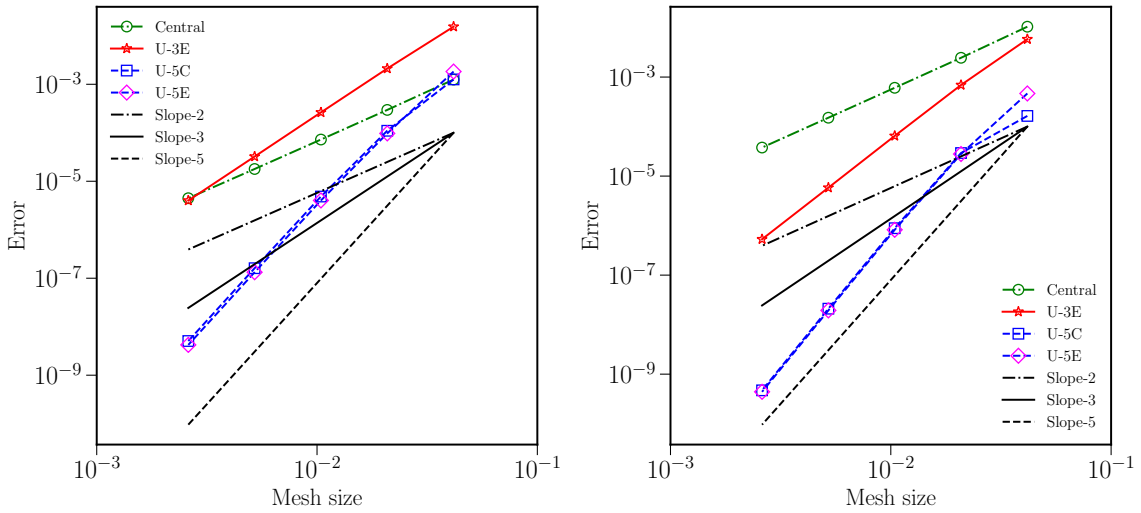

(a) Primary variable (b) Gradient variable

Figure 3.4: Example 3.1 L_2 convergence errors for one-dimensional test case using central scheme,U-3E, U-5C, U-5E, and WENO-5Z.

Table 3.1 shows the L_2 error for the velocity and the order of accuracy for the U-3E, U-5E, U-5C and WENO-5Z schemes respectively and design order of accuracy is obtained for all the schemes. Table 3.2 shows the L_2 error for the gradient variable, p, and the order of accuracy for the U-3E, U-5E,U-5C and WENO-5Z schemes respectively.

Table 3.1: L_2 errors and order of convergence of u, primary variable, by 3^{rd}, 5^{th} order explicit and compact and WENO schemes for Example 3.1.

Number of points	Upwind-3E		Upwind-5E		Upwind-5C		WENO-5Z	
	error	order	error	order	error	order	error	order
24	1.54E-02		1.83E-03		1.26E-03		2.64E-03	
48	2.11E-03	2.87	9.70E-05	4.24	1.10E-04	3.52	7.70E-05	5.10
96	2.63E-04	3.01	4.02E-06	4.59	4.84E-06	4.50	3.99E-06	4.27
192	3.23E-05	3.02	1.33E-07	4.91	1.61E-07	4.91	1.33E-07	4.90
384	4.00E-06	3.02	4.22E-09	4.98	5.07E-09	4.99	4.22E-09	4.98

Table 3.2: L_2 errors and order of convergence of gradient variable by 3^{rd}, 5^{th} order explicit and compact and WENO schemes one-dimensional diffusion problem for Example 3.1.

Number of points	Upwind-3E		Upwind-5E		Upwind-5C		WENO-5Z	
	error	order	error	order	error	order	error	order
24	5.82E-03		4.66E-04		1.64E-04		1.44E-03	
48	6.91E-04	3.07	2.79E-05	4.06	2.92E-05	2.48	2.73E-05	5.72
96	6.48E-05	3.42	8.23E-07	5.08	8.86E-07	5.04	8.23E-07	5.05
192	5.83E-06	3.47	1.94E-08	5.40	2.10E-08	5.40	1.94E-08	5.40
384	5.31E-07	3.46	4.40E-10	5.47	4.71E-10	5.48	4.40E-10	5.46

Figure 3.5 shows the comparison of ghost cell approach and weak boundary implementation, and it can be observed that ghost cell approach represents the solution more accurately on coarse meshes. Weak boundary implementation was unstable beyond 3^{rd} order accuracy whereas the ghost cell approach was found to be stable until 6th order accuracy. It may be noted that the ghost cell approach may be complicated to implement on an unstructured mesh compared to the weak formulation and also the difference between these approaches is minimal on finer meshes. Based on these observations only ghost cell approach has been employed for the all the test cases in the next subsections.

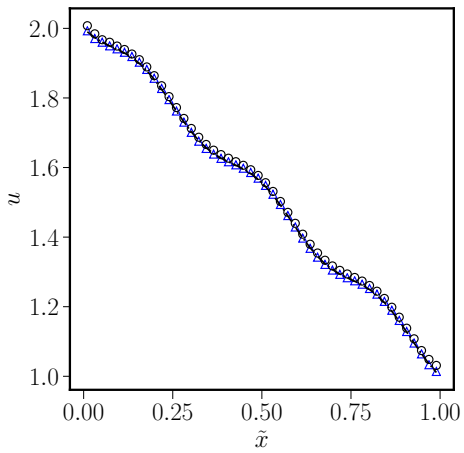

Figure 3.5: Example 3.1 Effect of boundary conditions. blue triangles: ghost cells; black circles - weak boundary.

3.3.2 Effect of shock capturing schemes

In Fig. 3.6(a), one can observe the difference between the shock-capturing schemes, TVD-MUSCL and Generalized-MUSCL. TVD-MUSCL formulation has not contaminated the solution and it is reduced to the linear third order scheme. On the other hand, the Generalized-MUSCL approach resulted in unnecessary oscillations and is only first order accurate, shown in Fig. 3.6(b), and it may not be appropriate for the diffusion equation in hyperbolic form.

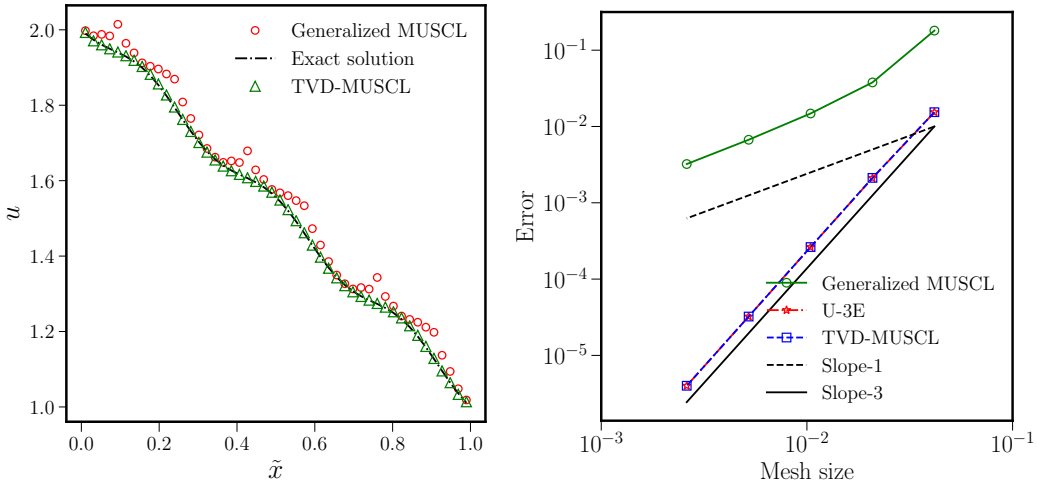

(a) Solution obtained by TVD schemes (b) Accuracy of TVD schemes

Figure 3.6: Example 3.1 Effect of TVD schemes.

Figure 3.7(a) shows the solution obtained by weighted essentially non-oscillatory schemes, WENO-JS, WENO-M and WENO-Z respectively. As expected, WENO-Z and WENO-M schemes have better accuracy than WENO-JS. WENO-M and WENO-Z gave similar results but it is well known that WENO-M scheme is more computationally intensive. Based on this analysis WENO-Z is considered for all the simulations in following sections. Order of accuracy for WENO schemes is shown in Fig. 3.7(b). From this analysis, shock-capturing schemes can be considered unnecessary for diffusion equation in hyperbolic approach. TVD schemes contaminated the solution depending on the type of the scheme considered whereas the WENO scheme did

not show any unnecessary oscillations for all the variations. It was also mentioned by Nishikawa [2] that no discontinuity capturing mechanism is required for the upwind formulation of the diffusion equation.

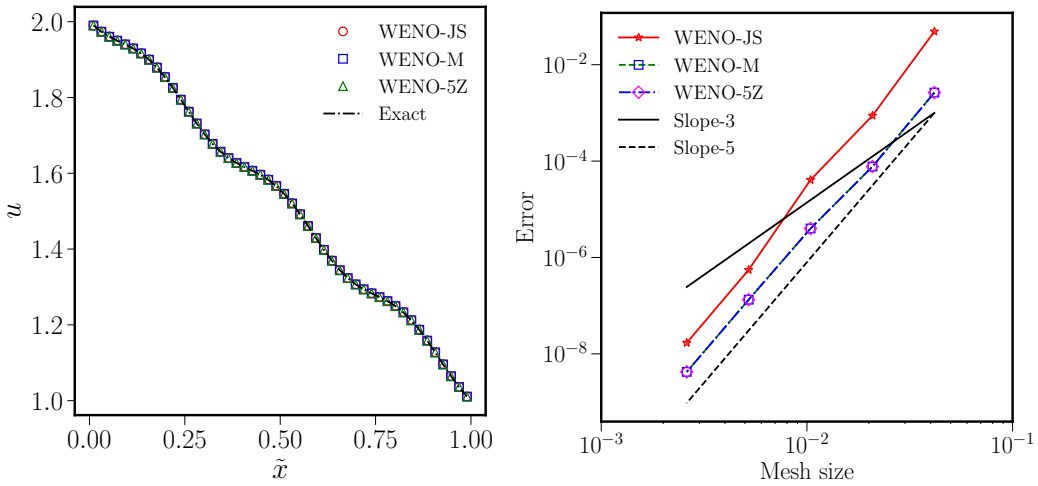

(a) Simulations by WENO schemes (b) Accuracy of WENO schemes

Figure 3.7: Example 3.1 Effect of WENO schemes.

3.3.3 Comparison with existing schemes

Example 3.2. In this test case the numerical schemes are compared with upwind schemes proposed by Nishikawa[1]. The following one-dimensional diffusion equation, [2], including a source term is considered with the domain size of $x \in$ [0,1].

$$\frac{\partial u}{\partial \tau} = \nu \frac{\partial^2 u}{\partial x^2} + \nu \pi^2 sin(\pi x), \tag{3.31}$$

where $\nu = 1$ and Dirichlet boundary conditions, $u_1 = 0, u_N = 0$, are considered. The exact solution for u and p are given by:

$$\begin{aligned} u_{exact} &= x(x-1), \\ p_{exact} &= 2(x-1). \end{aligned} \tag{3.32}$$

The simulations are conducted with grid refinements from $N = 16$ to 256 by 3^{rd} order upwind schemes proposed Nishikawa, U-3E and U-5E respectively. The numerical solution is computed by an explicit time-marching until the residuals are dropped below 10^{-12} in L_1 norm with a constant CFL $= 0.5$. Fig. 3.8(a) shows the solution contour obtained by U-3E and Nishikawa. The difference between the solutions is due to the fact that the current schemes are cell centered whereas Ref.[1] are node-based schemes. Fig. 3.8(b) shows the L_2 error for the velocity for U-3E, U-5E and Nishikawa's schemes respectively and the design order of accuracy is obtained for all the schemes.

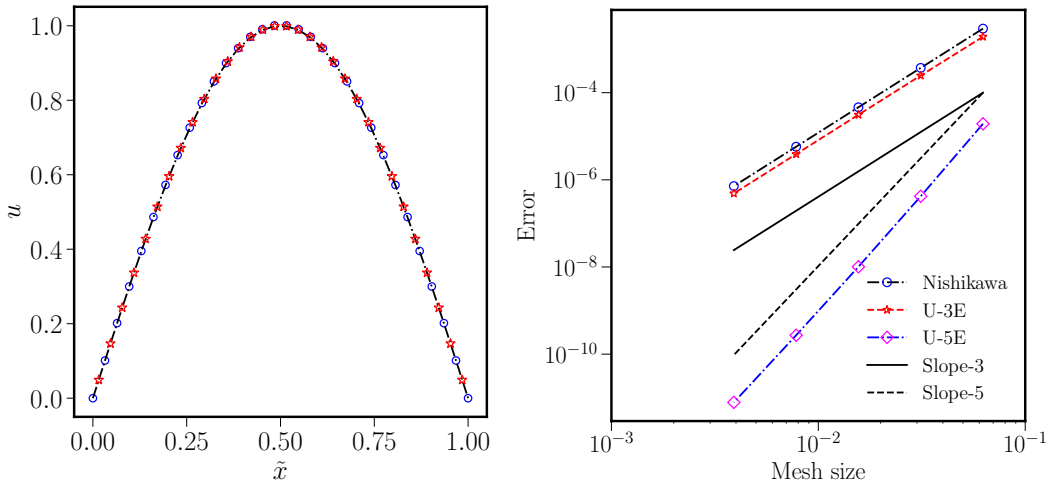

(a) Comparison

(b) Order of Accuracy

Figure 3.8: Example 3.2 Comparison of current approach and schemes proposed in Ref.[1] Dashed line: analytical; blue circles: Nishikawa; red stars: U-3E.

The current numerical schemes are based on uniform meshes and can be extended to arbitrary order of accuracy for the interior schemes. Numerical schemes employ ghost boundary approach whereas Nishikawa primarily considered weak boundary approach. Nishikawa's schemes are specifically developed for unstructured meshes and are at most third order accurate.

3.3.4 Two-dimensional test cases

Example 3.3. First test case is the following two-dimensional diffusion equation considered by Nishikawa [2]

$$\frac{\partial u}{\partial \tau} = \nu(\frac{\partial^2 u}{\partial x^2} + \frac{\partial^2 u}{\partial y^2}) \tag{3.33}$$

with a spatial domain of $[0,1]\times[0,1]$, where ν=1 and the following Dirichlet boundary conditions are considered:

$$u = \begin{cases} 0, & x = 0 \\ \sin(\pi y), & x = 1 \end{cases} \qquad u = \begin{cases} 0, & y = 0 \\ \sin(\pi x), & y = 1 \end{cases} \tag{3.34}$$

The exact steady state solution is given by,

$$u_{exact}(x,y) = \frac{\sinh(\pi x)\sin(\pi y) + \sinh(\pi y)\sin(\pi x)}{\sinh(\pi)}. \tag{3.35}$$

The simulations are conducted with grid refinements from 16×16 to 256 × 256 by second-order central, and all the upwind schemes. For upwind schemes, the numerical solution is computed by an explicit time-marching until the residuals are dropped below 10^{-12} in L_1 norm with a constant CFL = 0.5. The exact solution and numerical solution contours computed by the U-5E scheme are shown in Fig. 3.9(a) and Fig. 3.9(b). Computed values of u for various schemes along the geometric center line along the horizontal axis are shown in 3.10(a). L_2 error convergence results are shown in Fig. 3.10(b) for the primary variable and one can observe that the design order of accuracy is obtained for all the schemes.

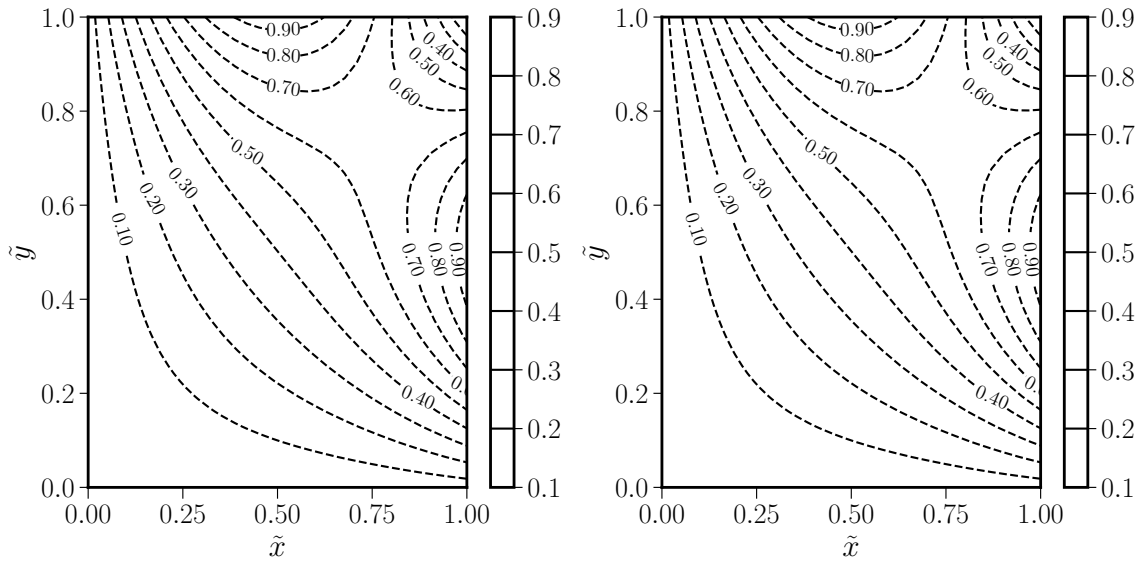

(a) Exact solution

(b) Numerical solution

Figure 3.9: Example 3.3 Comparison of analytical solution and by upwind scheme U-5E for diffusion equation are shown in (a) and (b) respectively.

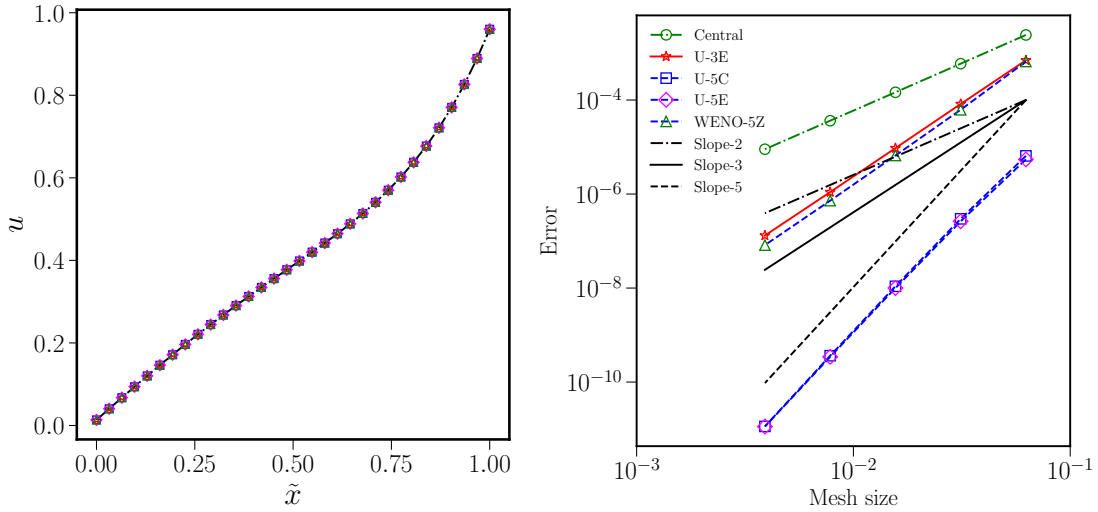

(a) Solution along geometric center line

(b) Convergence of the L_2 error

Figure 3.10: Computed values at geometric center and L_2 convergence errors for various schemes are shown in (a) and (b) respectively for Example 3.3. Dashed line: analytical; red stars: U-3E; blue squares: U-5C; magenta diamonds: U-5E; green triangles: WENO-5Z.

Table 3.3 shows the L_2 error for the primary variable, u, and the order of accuracy for the U-3E, U-5E,U-5C and WENO-5Z schemes respectively. Design order of accu-

racy is obtained for the velocity for all the linear upwind schemes. For the WENO scheme, the 5^{th} order boundary conditions are found to be unstable, and only 3^{rd} order boundary conditions are considered. TVD-MUSCL has once again reduced to 3rd order linear scheme and is not discussed henceforth for diffusion problems.

Table 3.3: L_2 errors and order of convergence of primary variable, u, by 3^{rd} order explicit, 5^{th} order explicit and compact and WENO schemes one-dimensional diffusion problem, Example 3.3.

Number of points	Upwind-3E		Upwind-5E		Upwind-5C		WENO-5Z	
	error	order	error	order	error	order	error	order
16	7.01E-04		5.46E-06		6.48E-06		6.59E-04	
32	8.24E-05	3.09	2.63E-07	4.37	2.97E-07	4.45	6.20E-05	3.41
64	9.47E-06	3.12	1.00E-08	4.72	1.09E-08	4.77	6.60E-06	3.23
128	1.10E-06	3.10	3.44E-10	4.86	3.64E-10	4.90	7.23E-07	3.19
256	1.31E-07	3.07	1.13E-11	4.93	1.14E-11	5.00	8.19E-08	3.14

Example 3.4 In this test case, the verification of Neumann boundary condition which is also implemented as Dirichlet boundary condition in the hyperbolic formulation for diffusion equation is considered. The following two-dimensional Laplace equation with the spatial domain of [0, 1] $\times$ [0, 1], Eq. (3.36), has been considered.

$$\frac{\partial^2 \phi}{\partial x^2} + \frac{\partial^2 \phi}{\partial y^2} = 0 \tag{3.36}$$

which has the following Neumann and Dirichlet boundary conditions

$$\begin{matrix} \phi = 0, x = 0 \\ \dfrac{\partial \phi}{\partial x} = 0, x = L \end{matrix} \qquad \phi = \begin{cases} 0, & y = 0 \\ \sin\left(\frac{\frac{3}{2}\pi x}{L}\right), & y = M, \end{cases} \tag{3.37}$$

where $L = 1$ and $M = 1$ and the analytical solution is given by Eq. (3.38)

$$\phi_{exact}(x, y) = \frac{\sinh\left(\frac{\frac{3}{2}\pi y}{L}\right)}{\sinh\left(\frac{\frac{3}{2}\pi M}{L}\right)} \sin\left(\frac{\frac{3}{2}\pi x}{L}\right) \tag{3.38}$$

The simulations are conducted with grid refinements from 16×16 to 256 × 256 for the test case. For the upwind schemes, the numerical solution is again computed by an explicit time-marching until the residuals are dropped below 10^{-12} in L_1 norm with a constant CFL = 0.5. Computed values of ϕ for various schemes along the geometric center line along the horizontal axis are shown in Fig. 3.11 for a 32 × 32 grid.

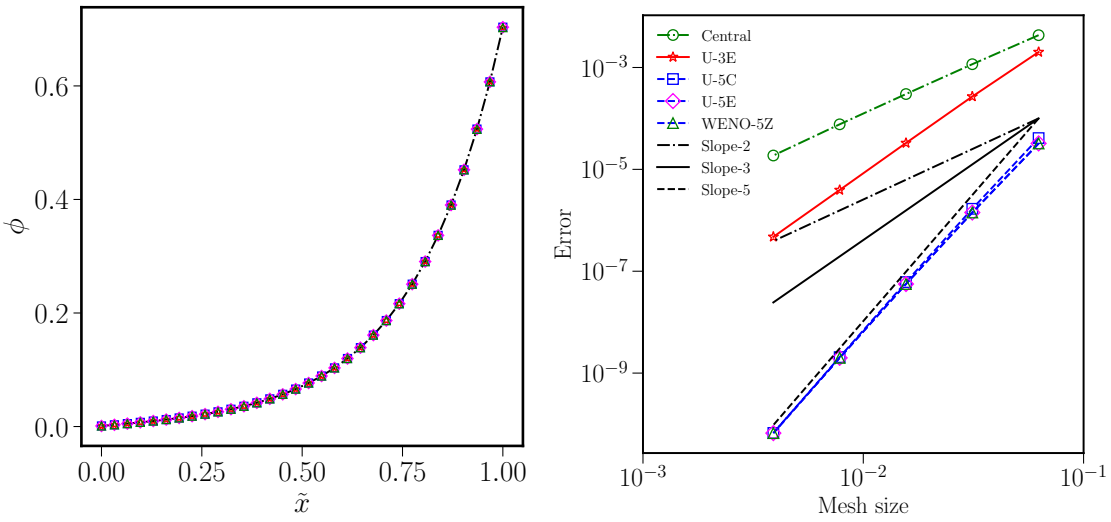

(a) Solution along geometric center line

(b) Convergence of the L_2 error

Figure 3.11: Computed values at geometric center and L_2 convergence errors for various schemes for Neumann boundary condition, Example 3.4. Dashed line: analytical; red stars: U-3E; blue squares: U-5C; magenta diamonds: U-5E; green triangles: WENO-5Z.

Table 3.4 show the L_2 norms for all the schemes and the advantage of high-order methods over lower-order methods can be seen as they need less number of computational cells to get a solution with the same accuracy. This advantage enables high-order methods to use coarse meshes, in comparison with the lower-order methods. Design accuracy is obtained for all the schemes, and the implementation of Neumann boundary condition is successfully verified through this test case. Unlike the previous test case, WENO scheme also shows 5^{th} order accuracy.

Table 3.4: L_2 errors and order of convergence of potential by 3^{rd} order explicit, 5^{th} order explicit and compact and WENO schemes for Example 3.4.

Number	Upwind-3E		Upwind-5E		Upwind-5C		WENO-5Z	
of points	error	order	error	order	error	order	error	order
16^2	2.01E-03		3.23E-05		4.11E-05		3.22E-05	
32^2	2.69E-04	2.90	1.42E-06	4.50	1.68E-06	4.61	1.42E-06	4.50
64^2	3.29E-05	3.03	5.61E-08	4.67	6.12E-08	4.78	5.61E-08	4.67
128^2	3.93E-06	3.06	1.99E-09	4.82	2.06E-09	4.89	1.99E-09	4.82
256^2	4.73E-07	3.06	6.63E-11	4.91	6.68E-11	4.95	6.62E-11	4.91

Example 3.5. For the previous test cases and the given numerical grids, one could not distinguish the numerical results by different methods. In this example, the following Poisson equation, i.e., with a source term, given by Eq. (3.39) is considered

$$\frac{\partial^2 \phi}{\partial x^2} + \frac{\partial^2 \phi}{\partial y^2} = 32\pi^2 \sin(4\pi x) \sin(4\pi y) \tag{3.39}$$

where the domain is [0, 1] $\times$ [0, 1] and $\phi = 0$ at all the boundaries. The exact solution for this test case is given by

$$\phi_{exact}(x, y) = \sin(4\pi x) \sin(4\pi y) \tag{3.40}$$

In this test case, the advantage of 5^{th} order schemes can be observed. The simulations are conducted with grid refinements from 16$\times$16 to 256 $\times$ 256 for the test case. For the upwind schemes, the numerical solution is deemed to have reached a steady state when the residuals are dropped below 10^{-12} in L_1 norm and constant CFL = 0.5 is used. Table 3.5 shows the L_2 error for the primary variable, ϕ, and the order of accuracy for the U-3E, U-5E,U-5C and WENO-5Z schemes respectively. Compact schemes show better accuracy for problems with source term with increasing grid size in comparison with the explicit scheme.

Table 3.5: L_2 errors and order of convergence for two-dimensional Poisson problem, Example 3.5, by 3^{rd} order explicit, 5^{th} order explicit and compact and WENO schemes.

Number	Upwind-3E		Upwind-5E		Upwind-5C		WENO-5Z	
of points	error	order	error	order	error	order	error	order
16^2	2.466E-01		3.06E-02		2.65E-02		6.15E-02	
32^2	3.221E-02	2.94	1.16E-03	4.72	7.32E-04	5.18	1.30E-03	5.56
64^2	4.006E-03	3.01	3.42E-05	5.09	1.35E-05	5.76	3.52E-05	5.21
128^2	4.985E-04	3.01	1.01E-06	5.09	2.30E-07	5.87	1.01E-06	5.12
256^2	6.218E-05	3.00	3.03E-08	5.05	4.01E-09	5.84	3.01E-08	5.07

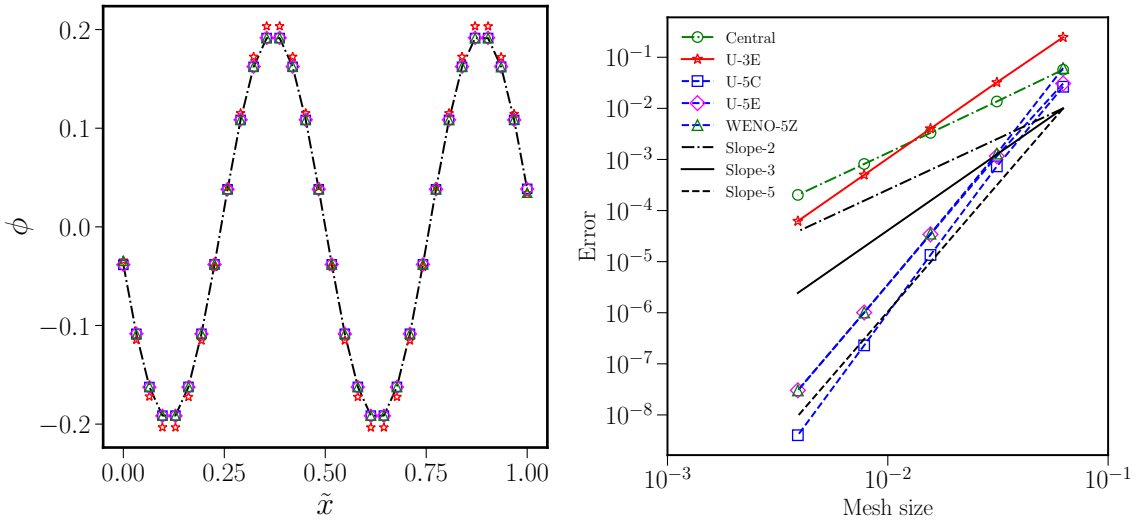

(a) Solution along geometric center line

(b) Convergence of the L_2 error

Figure 3.12: Computed values at geometric center and L_2 convergence errors for various schemes for Poisson equation, Example 3.5, are shown here. Dashed line: analytical; red stars: U-3E; blue squares: U-5C; magenta diamonds: U-5E; green triangles: WENO-5Z.

In Figure 3.12(a) the computed results at geometric center on a 32 × 32 grid is shown and one can observe that the third order explicit scheme has deviated considerably from the exact solution in comparison with the other schemes. It can be seen from the L_2 norms shown in the Fig. 3.12(b) that even though third order accuracy is obtained for the upwind scheme, U-3E, the solution is inferior to standard second

order case on coarse meshes. Such results are also observed in edge based methods proposed by Nishikawa in [Ref. [1], Figs. 4 and 5]. The source term may have a significant effect on the solution accuracy for the upwind formulation.

3.3.5 Effect of Length scale L_r and Relaxation time T_r

Re-consider the diffusion equation (3.1) in two dimensions, and the hyperbolic formulation

$$\begin{aligned} \frac{\partial u}{\partial \tau} &= \nu \left(\frac{\partial p}{\partial x} - \frac{\partial q}{\partial y} \right), \\ \frac{\partial p}{\partial \tau} &= \frac{1}{T_r} \left(\frac{\partial u}{\partial x} - p \right), \\ \frac{\partial q}{\partial \tau} &= \frac{1}{T_r} \left(\frac{\partial u}{\partial y} - q \right), \end{aligned} \tag{3.41}$$

where a new variable T_r may be called a relaxation time has been introduced. For the steady state computation, the relaxation time T_r is a free parameter. For the all the earlier examples T_r is considered as 1. For the sake of dimensional consistency T_r is defined in [2] as

$$T_r = \frac{L_r^2}{\nu}, \tag{3.42}$$

where L_r is the length scale. The value of L_r may be taken as **1** but it may not be the best possible value. The optimum value of L_r depends on the type and order of the scheme and also on the purpose for which the scheme is employed. Through Fourier analysis an optimum value of L_r is derived for the finite volume first order upwind schemes in Ref. [1, 62] and is defined as,

$$L_r \geq \frac{2h}{(\pi h + 4)\pi h}, \tag{3.43}$$

where h is the grid size. As $h \to 0$, $L_r = \frac{1}{2\pi}$. Example 3.1 and Example 3.4 are reevaluated by using the new variable T_r and the results are shown in Figs. 3.13(a) and 3.13(b). It can be seen that T_r effects the error of the primary variable and also

the convergence speed but does not effect the consistency and order of accuracy. The length scale, L_r, could significantly effect when solving dimensional equations, which is discussed in next example, and anisotropic diffusion equation discussed in next chapter.

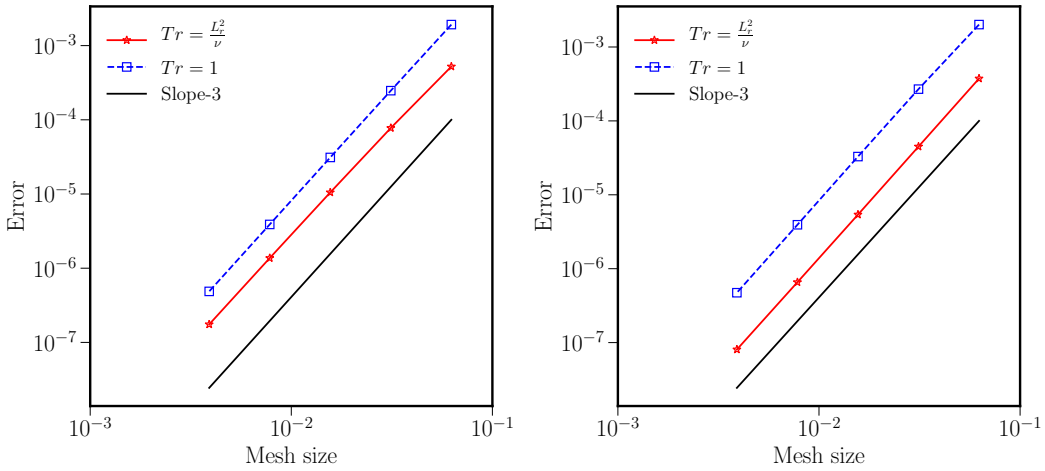

(a) One-dimensional test (b) Two-dimensional test

Figure 3.13: Effect of relaxation length for the diffusion equation. Fig. (a) Example 3.1 and Fig. (b) Example 3.4.

3.3.6 Effect of dimensions

Example 3.7. In this final example problem with dimensions, i.e the domain L_x and L_y may not be equal to unity, is considered. In the previous examples smooth isotropic solutions are considered, but if numerical schemes are to be applied to practical problems with high-Reynolds number viscous simulations, they must be tested for anisotropic solutions and one such problem is given by Eq. (3.44)

$$\frac{\partial^2 \phi}{\partial x^2} + \frac{\partial^2 \phi}{\partial y^2} = -(1 + 2000^2)\pi^2 \sin(\pi x) \sin(2000\pi y), \tag{3.44}$$

where the domain is [0, 1] × [0, 0.005] and $\phi = 0$ at all the boundaries. The exact solution for this test case is given by

$$\phi_{exact}(x, y) = \sin(\pi x) \sin(2000\pi y). \tag{3.45}$$

One can see that $L_y = 0.005$, which is not unity, and for such problems the optimum formula for length scale L_r given in Ref. [62], which is given by Eq. (3.46)

$$L_r = \frac{1}{2\pi} \frac{L_x L_y}{\sqrt{(L_x^2 + L_y^2)}}. \tag{3.46}$$

The simulations are conducted with grid refinements from 20 × 20 to 320 × 320 for the test case. For the upwind schemes, the numerical solution is deemed to have reached a steady state when the residuals are dropped below 10^{-14} in L_1 norm and constant CFL = 0.45 is used. The solution contours for U-5E are shown in Fig. 3.14(a). The L_2 norms shown in the Fig. 3.14(b) and design order of accuracy is obtained for all the schemes. It has been observed that if an optimum L_r is not considered the solution will diverge and may not reach steady state results. L_2 errors for various schemes is shown in Table 3.6. It can be observed that the 5^{th} order schemes are significantly more accurate for anisotropic solutions even on coarse meshes and 3^{rd} order schemes are once again inferior to 2^{nd} order central schemes on coarse meshes.

Table 3.6: L_2 errors and order of convergence of u, primary variable for Example 3.7 by 2^{nd} order central, 3^{rd} order explicit, 5^{th} order explicit and compact schemes.

Number of points	Central-2		Upwind-3E		Upwind-5E		Upwind-5C	
	error	order	error	order	error	order	error	order
20	0.1894305		0.8729564		0.2893233		0.286379	
40	5.04E-02	1.91	8.90E-02	3.29	2.06E-02	3.81	2.26E-02	3.66
80	1.28E-02	1.98	9.68E-03	3.20	4.88E-04	5.40	4.91E-04	5.53
160	3.21E-03	1.99	1.17E-03	3.05	1.02E-05	5.57	6.80E-06	6.17
320	8.03E-04	2.00	1.47E-04	3.00	2.67E-07	5.26	7.44E-08	6.51

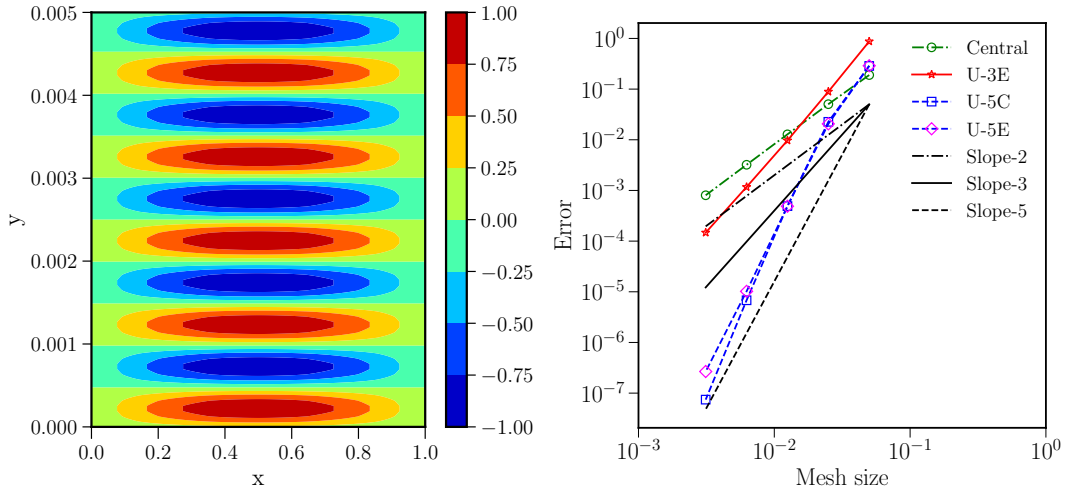

(a) Solution contours U-5E

(b) Order of accuracy

Figure 3.14: Example 3.7 Simulation results for equations with dimensions on a grid size of 80×80 and order of accuracy of upwind schemes.

3.4 Summary

The important findings of this chapter are summarized as follows:

1. Efficient and accurate demonstration of the hyperbolic method for the steady diffusion equation using the cell-centered finite volume or difference framework is shown.

2. High-order and high-resolution methods are implemented successfully for the diffusion equation in the hyperbolic form on uniform meshes. Design order of accuracy is obtained for all the schemes for all the test problems considered.

3. Shock-capturing schemes are found to be unnecessary for diffusion equation, and by various test cases, the inapplicability of certain TVD schemes is explained. Even though the WENO scheme is a shock-capturing scheme the steady-state solutions are not contaminated and are similar to the linear schemes.

4. Ghost cell approach is found to be more accurate and stable than the weak boundary implementation, especially on coarse meshes. Linear upwind schemes

are consistently stable with the corresponding higher order boundary conditions whereas WENO is stable only with 3^{rd} order boundary conditions due to their inherent non-linearity.

5. Relaxation time and length scales are important for dimensional equations and design accuracy is also achieved such problems.

CHAPTER IV

Hyperbolic approach for Anisotropic Diffusion

In this chapter the hyperbolic approach is extended to anisotropic diffusion equation. A key distinction between the present methodology and the earlier efforts based on first order upwind [29] and third order accurate monotonicity preserving TVD discretization is in the implementation of high-order finite-volume WENO discretization and implementation of WENO extrapolation for boundary conditions. The gain in accuracy and reduction in numerical oscillations are significantly more pronounced for the WENO schemes when compared with TVD discretization. An alternate hyperbolic approach for anisotropic diffusion is also constructed and the merits are discussed.

4.1 Governing equations

Magnetized electron fluid simulations can have the features like sharp gradients in the flow field, strongly diffusion dominated flow with anisotropic diffusion and also have the convection aspect of the flow. The system of equations, electron mass and momentum equations, for the magnetized electron fluid in quasi-neutral flow described by Kawashima et al. [29] are given by

$$\nabla \cdot (n_{\mathrm{e}} \vec{u}_{\mathrm{e}}) = n_{\mathrm{e}} \nu_{\mathrm{ion}}, \tag{4.1}$$

$$n_{\mathrm{e}}\left[\mu\right]\nabla\phi - \left[\mu\right]\nabla\left(n_{\mathrm{e}}T_{\mathrm{e}}\right) = n_{\mathrm{e}}\vec{u}_{\mathrm{e}}, \tag{4.2}$$

where n_{e}, $\vec{u}_{\mathrm{e}}$, ϕ, ν_{ion}, and T_{e}, are the electron number density, electron velocity, space potential, ionization collision frequency, and electron temperature respectively. The electron mobility tensor $[\mu]$ can be expressed as follows,

$$\left[\mu\right] = \begin{bmatrix} \mu_x & \mu_{\mathrm{c}} \\ \mu_{\mathrm{c}} & \mu_y \end{bmatrix} = \Theta^{-1}\begin{bmatrix} \mu_{||} & \\ & \mu_{\perp} \end{bmatrix}\Theta, \qquad \Theta = \begin{bmatrix} \cos\theta & -\sin\theta \\ \sin\theta & \cos\theta \end{bmatrix} \tag{4.3}$$

$$\mu_{||} = \frac{e}{m_{\mathrm{e}}\nu_{\mathrm{col}}}, \quad \mu_{\perp} = \frac{\mu_{||}}{1 + \left(\mu_{||}B\right)^2}$$

where e, B, and ν_{col} are the elemental charge, magnetic flux density, and electron-neutral total collision frequency, respectively. Also, Θ is the rotation matrix, and θ is the angle between the magnetic lines of force and the grid, shown in Fig. 4.1. The electron flux in parallel ($||$) and perpendicular ($\perp$) directions of the magnetic lines of force are described by using the electron mobility $\mu_{||}$ and $\mu_{\perp}$ respectively. Assuming

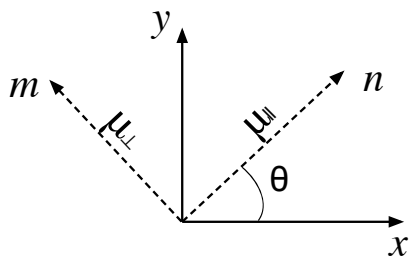

Figure 4.1: Illustration of symbols, $\mu_{||}$, $\mu_{\perp}$ and θ.

steady state, the following plasma diffusion equation can be obtained by substituting momentum equation 4.2 in to continuity equation 4.1

$$\nabla\cdot\left(n_{\mathrm{e}}\left[\mu\right]\nabla\phi - \left[\mu\right]\nabla\left(n_{\mathrm{e}}T_{\mathrm{e}}\right)\right) = n_{\mathrm{e}}\nu_{\mathrm{ion}}. \tag{4.4}$$

For a given electron number density and temperature distribution, this equation can then be solved for plasma potential, ϕ, using a general Poisson's equation solver [24, 63]. Equation (4.4) is usually solved by a central scheme [27, 28] and it is a well known fact that the central scheme can lead to numerical oscillations if sharp gradients are present in the flow. This approach also suffers from poor iterative convergence due to the large disparity between $\mu_{||}$ and $\mu_{\perp}$. To avoid these difficulties Kawashima et al. [29] has proposed hyperbolic approach by introducing pseudo-time terms in the continuity and momentum equations. This approach is similar to the artificial compressibility method utilized in solving incompressible Navier-Stokes [64], where a pseudo-time derivative of the pressure is added to the continuity equation. Similarly, a pseudo-time derivative of plasma potential is added in the continuity equation and the corresponding equations are as follows,

$$\begin{aligned} \frac{n_\mathrm{e}}{T_\mathrm{e}}\frac{\partial \phi}{\partial \tau} - \nabla\cdot\left(n_\mathrm{e}\vec{u}_\mathrm{e}\right) &= -n_\mathrm{e}\nu_\mathrm{ion}, \\ \frac{1}{\nu_\mathrm{col}}\frac{\partial}{\partial \tau}\left(n_\mathrm{e}\vec{u}_\mathrm{e}\right) - n_\mathrm{e}\left[\mu\right]\nabla\phi + \left[\mu\right]\nabla\left(n_\mathrm{e}T_\mathrm{e}\right) &= -n_\mathrm{e}\vec{u}_\mathrm{e}. \end{aligned} \tag{4.5}$$

For the simulations, the equations are expressed in non-dimensional form. The non-dimensionalization procedure of the equation system (4.5) and the definitions of dimensionless quantities are same as that of Ref. [29] which are as follows:

$$\tilde{n}_\mathrm{e} = \frac{n_\mathrm{e}}{n_\mathrm{e}^*}, \qquad \tilde{T}_\mathrm{e} = \frac{T_\mathrm{e}}{T_\mathrm{e}^*}, \qquad \tilde{\phi} = \frac{\phi}{\phi_\mathrm{a}}, \qquad (\tilde{x},\tilde{y})^T = \frac{1}{\lambda_\mathrm{m}^*}(x,y)^T, \tag{4.6}$$

$$\tilde{t} = \frac{1}{\lambda_\mathrm{m}^*}\sqrt{\frac{2eT_\mathrm{e}^*}{m_\mathrm{e}}}t, \qquad \tilde{\vec{u}}_\mathrm{e} = \frac{\vec{u}_\mathrm{e}}{c_\mathrm{s}^*} = \frac{\vec{u}_\mathrm{e}}{\sqrt{\frac{\gamma eT_\mathrm{e}^*}{m_\mathrm{e}}}}, \qquad \tilde{\nu}_\mathrm{col} = \tau_\mathrm{m}^*\nu_\mathrm{col}, \quad \tilde{\nu}_\mathrm{ion} = \tau_\mathrm{m}^*\nu_\mathrm{ion}. \tag{4.7}$$

where τ_m, $v_\mathrm{e,th}$, c_s and γ are the mean free time, electron thermal velocity, and electron acoustic velocity, and specific heat ratio respectively. Also, the electron number density n_e^*, electron temperature T_e^*, potential ϕ_a, and mean free path λ_m^* are the reference values. For simplified analysis the following values are assumed for all the

test calculations,

$$\tilde{n}_{\mathrm{e}} = 1, \qquad \tilde{T}_{\mathrm{e}} = 1, \qquad \tilde{\nu}_{\mathrm{col}} = 1, \qquad \tilde{\nu}_{\mathrm{ion}} = 0. \tag{4.8}$$

Finally, By adding the pseudo-time terms the simplified non-dimensional system of electron fluids for the Eq. (4.5) can be expressed as follows:

$$\begin{aligned} \frac{\partial \tilde{\phi}}{\partial \tilde{\tau}} - \sqrt{\frac{\gamma}{2}} \tilde{\nabla} \cdot \vec{\tilde{u}}_{\mathrm{e}} = 0, \\ \frac{\partial \vec{\tilde{u}}_{\mathrm{e}}}{\partial \tilde{\tau}} - \frac{1}{\sqrt{2\gamma}} \left[\tilde{\mu}\right] \tilde{\nabla} \tilde{\phi} = -\vec{\tilde{u}}_{\mathrm{e}}. \end{aligned} \tag{4.9}$$

The final non-dimensional hyperbolic equations are as follows:

$$\frac{\partial \mathbf{Q}}{\partial \tilde{\tau}} + \frac{\partial \mathbf{E_x}}{\partial \tilde{x}} + \frac{\partial \mathbf{E_y}}{\partial \tilde{y}} = S, \tag{4.10}$$

where the conservative variables, fluxes in x and y-direction and source terms are,

$$\mathbf{Q} = \begin{bmatrix} \tilde{\phi} \\ \tilde{u}_{\mathrm{x}} \\ \tilde{u}_{\mathrm{y}} \end{bmatrix}, \quad \mathbf{E_x} = \begin{bmatrix} \tilde{u}_{\mathrm{x}} \\ \phi \\ \phi \end{bmatrix}, \quad \mathbf{E_y} = \begin{bmatrix} \tilde{u}_{\mathrm{y}} \\ \phi \\ \phi \end{bmatrix}, \quad \mathbf{S} = \begin{bmatrix} 0 \\ -\tilde{u_{\mathrm{x}}} \\ -\tilde{u_{\mathrm{y}}} \end{bmatrix}. \tag{4.11}$$

4.1.1 Construction of hyperbolic scheme and preconditioned system

Due to the significant discrepancy between parallel, $\mu_{||} = 10^3$, and orthogonal, $\mu_{\perp} = 1$, mobilities, the condition number of the system increases significantly and degrades the convergence performance. Convergence can be made independent of mobility by altering the eigenvalues of the system such that all of them are of the same order. A popular approach is to multiply the system of equations by a preconditioning matrix to normalize the eigenvalues [65]. The system can be written in the preconditioned

form as,

$$\hat{\mathbf{P}}^{-\mathbf{1}}\frac{\partial \mathbf{Q}}{\partial \tilde{\tau}} + \frac{\partial \mathbf{E_x}}{\partial \tilde{x}} + \frac{\partial \mathbf{E_y}}{\partial \tilde{y}} = S, \tag{4.12}$$

where $\hat{\mathbf{P}} = \Theta^{-1} P \Theta$ is a preconditioning matrix which is derived based on the idea of electron mobility tensor rotation

$$P = \begin{pmatrix} \sqrt{\frac{2}{\gamma}} & 0 & 0 \\ 0 & \frac{\sqrt{2\gamma}}{\tilde{\mu}_{||}} & 0 \\ 0 & 0 & \frac{\sqrt{2\gamma}}{\tilde{\mu}_{\perp}} \end{pmatrix}, \qquad \Theta = \begin{pmatrix} 1 & 0 & 0 \\ 0 & \cos\theta & \sin\theta \\ 0 & -\sin\theta & \cos\theta \end{pmatrix}. \tag{4.13}$$

Finally, the preconditioned system of equations can be rewritten as follows:

$$\begin{aligned} \frac{\partial \tilde{\phi}}{\partial \tilde{\tau}} - \nabla \cdot \vec{\tilde{u}}_{\mathrm{e}} &= 0 \\ \frac{\partial \vec{\tilde{u}}_{\mathrm{e}}}{\partial \tilde{\tau}} - \nabla \tilde{\phi} &= -[g]\vec{\tilde{u}}_{\mathrm{e}}, \end{aligned} \tag{4.14}$$

where, [**g**] is a tensor which is written as follows:

$$[\mathbf{g}] = \frac{\sqrt{2\gamma}}{\tilde{\mu}_{||}} \begin{bmatrix} \cos^2\theta + \frac{\tilde{\mu}_{||}}{\tilde{\mu}_{\perp}}\sin^2\theta & (\frac{\tilde{\mu}_{||}}{\tilde{\mu}_{\perp}} - 1)\cos\theta\sin\theta \\ (\frac{\tilde{\mu}_{||}}{\tilde{\mu}_{\perp}} - 1)\cos\theta\sin\theta & \sin^2\theta + \frac{\tilde{\mu}_{||}}{\tilde{\mu}_{\perp}}\cos^2\theta \end{bmatrix}. \tag{4.15}$$

The flux Jacobian matrices and the corresponding eigenvalues for the preconditioned system of equations can be expressed as follows,

$$\hat{\mathbf{PJ}}_x = \begin{pmatrix} 0 & -1 & 0 \\ -1 & 0 & 0 \\ 0 & 0 & 0 \end{pmatrix}, \qquad \hat{\mathbf{PJ}}_y = \begin{pmatrix} 0 & 0 & -1 \\ 0 & 0 & 0 \\ -1 & 0 & 0 \end{pmatrix}, \quad \lambda = \pm 1, 0. \tag{4.16}$$

We can notice that the above Jacobian matrices are the same as that of the hyperbolic form of diffusion equation derived for the diffusion equation, Eq. (3.6). The upwind fluxes are the same for both set of equations, and by changing the source

terms and by using appropriate boundary conditions the magnetized electron fluid equations and diffusion can be simulated by the same code. Therefore, the Jacobian matrices are not affected by the magnetic field as they are included in the source terms and also the eigenvalues are significantly simplified which improves the convergence speed. Similarly to the anisotropic diffusion equation, the upwind flux for the magnetized electrons will be constructed by following the standard procedure of local preconditioning method [66], i.e., the preconditioned Jacobian is multiplied by $\mathbf{P}^{-1}$ to cancel the effect of $\mathbf{P}$,

$$\hat{E}_{i+\frac{1}{2},j} = \frac{1}{2}(\mathbf{E_L} + \mathbf{E_R}) - \frac{1}{2}\hat{\mathbf{P}}^{-\mathbf{1}}|\hat{\mathbf{P}}\hat{\mathbf{J}}_{\mathbf{x}}|(\mathbf{Q_R} - \mathbf{Q_L}), \tag{4.17}$$

4.1.2 Boundary conditions: WENO extrapolation

In situations where there are sharp gradients close to the boundary, the Lagrange extrapolation may result in severe oscillations. To overcome such difficulties a more robust WENO type extrapolation is proposed by Tan and Shu [60, 41]. Analogous to the idea of WENO, three polynomials are constructed for the extrapolation given by,

$$\begin{aligned} P_0(x) &= u_0, \\ P_1(x) &= \frac{(u_1 - u_0)}{\Delta x}x + u_0, \\ P_2(x) &= u_0 + \frac{-3u_0 + 4u_1 - u_2}{2\Delta x}x + \frac{u_0 - 2u_1 + u_2}{2\Delta x^2}x^2. \end{aligned} \tag{4.18}$$

Using the standard WENO procedure, the equation 3.23, Lagrange extrapolation, can be rewritten as,

$$u^k = \sum_{r=0}^{2} \omega_r \frac{d^k p_r(x)}{dx^k}, \quad at\ x = \frac{\Delta x}{2} \tag{4.19}$$

where ω_r are the typical nonlinear weights given by, $\omega_r = \frac{\alpha_r}{\sum_{r=0}^{2} \alpha_s}$ and $\alpha_r = \frac{d_r}{(\epsilon+\beta_r)^3}$, where the linear weights d_r are chosen as

$$d_0 = \Delta x^2, d_1 = \Delta x, d_2 = 1 - \Delta x - \Delta x^2, \tag{4.20}$$

and the smoothness indicators β_r are obtained by,

$$\beta_j = \sum_{l=1}^{2} \Delta x^{2l-1} \int_{-\Delta x}^{0} \left(\frac{d^l}{dx^l} p_j(x) \right)^2 dx. \tag{4.21}$$

When doing WENO extrapolation on left boundary, the smoothness indicators are listed below:

$$\begin{aligned}
\beta_1 =& \Delta x^2 \\
\beta_2 =& (u_0 - u_1)^2 \\
\beta_3 =& \frac{13}{12}(u_0 - 2u_1 + u_2)^2 + (2u_0 - 3u_1 + u_2)^2
\end{aligned}$$

The coefficients for right boundary extrapolation can be obtained by symmetry. Only 3^{rd} order WENO extrapolation is considered for all the simulations.

4.2 Numerical tests and discussion

The test calculation considered by Kawashima et al. [29] with uniformly angled Magnetic lines of force at 45° from the vertical, shown in Fig. 4.2, is considered here. For a Cartesian mesh, the condition of 45° magnetic lines of force can give significant false diffusion [67]. False diffusion will occur due to the oblique flow direction and non-zero gradient in the direction normal to the flow. As a consequence of false diffusion, non-physical local extrema can occur in regions in which the gradients of the solution are steep and not aligned with the orientation of grid, and the discretization method will

be unable to capture them properly. Results were obtained for three different values of magnetic confinements, $\mu_{||}/\mu_{\perp}$=100, 500 and 1000, which are uniform throughout the domain. Dirichlet boundary conditions for the non-dimensional space potential are defined at the left and right side boundaries and zero-flux conditions, which are also Dirichlet, are used for the top and bottom boundaries, shown in Eq. (4.22).

$$\tilde{\phi} = \begin{cases} 1, & x = 0 \\ 0, & x = 200 \end{cases} \qquad \tilde{u}_y = \begin{cases} 0, & y = 0 \\ 0, & y = 100 \end{cases} \tag{4.22}$$

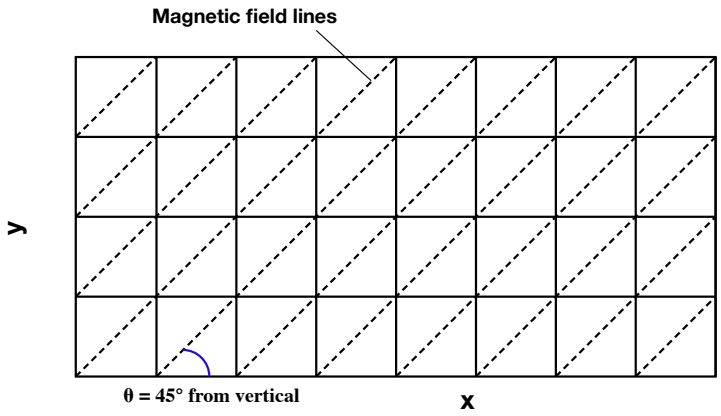

Figure 4.2: Sketch of the magnetic field lines for 45° angle.

Unlike the test cases of diffusion and advection-diffusion where the numerical schemes are compared with the analytical solutions, the linear and WENO upwind schemes are compared with the Magnetic Field Aligned Mesh (MFAM). MFAM is described by Mikellides et al. [26] and Kawashima et al. [29], which eliminates the false diffusion by aligning the mesh with the magnetic field. The simulations are conducted for both MFAM and the upwind schemes with grid refinements of NX, NY = [96, 48] to [768, 384] for all the values of $\mu_{||}/\mu_{\perp}$. For the upwind methods, the numerical solution is computed by explicit time marching with a constant CFL of 0.32. Regardless of the interior scheme, 3rd order accurate boundary conditions are considered for all

the upwind schemes for stable computation. The steady-state solution is deemed to be reached if the L_1 norms are below 10^{-12}. As far the MFAM approach, successive over-relaxation is used to numerically relax the solution until the L_2 norms are below 10^{-10} by second-order central discretization. Figs. 4.3 and 4.4 show the velocity streamlines computed by using different schemes for mobility ratios $\mu_{||}/\mu_{\perp}$=10, 500 and 1000. Velocity streamlines computed by MFAM are shown in Figs. 4.4(a), 4.4(b) and 4.4(c) respectively and we can see that as $\mu_{||}/\mu_{\perp}$ is increasing the plasma is more confined to the center. For $\mu_{||}/\mu_{\perp} = 100$ all the linear schemes and WENO has similar results compared to that of the MFAM whereas the Generalized MUSCL approach is showing unphysical streamlines even for such small anisotropies. From the Figs. 4.3(c) and 4.4(f), we can see that there are significant unphysical vortices in Upwind-3E for $\mu_{||}/\mu_{\perp} = 1000$. Results obtained by TVD-MUSCL are same as that of Upwind-3E scheme, similar to the results observed for isotropic diffusion problems. However, the fifth order schemes, Upwind-5C, Upwind-5E, and WENO-5Z-L, were able to reduce the unphysical oscillations significantly.

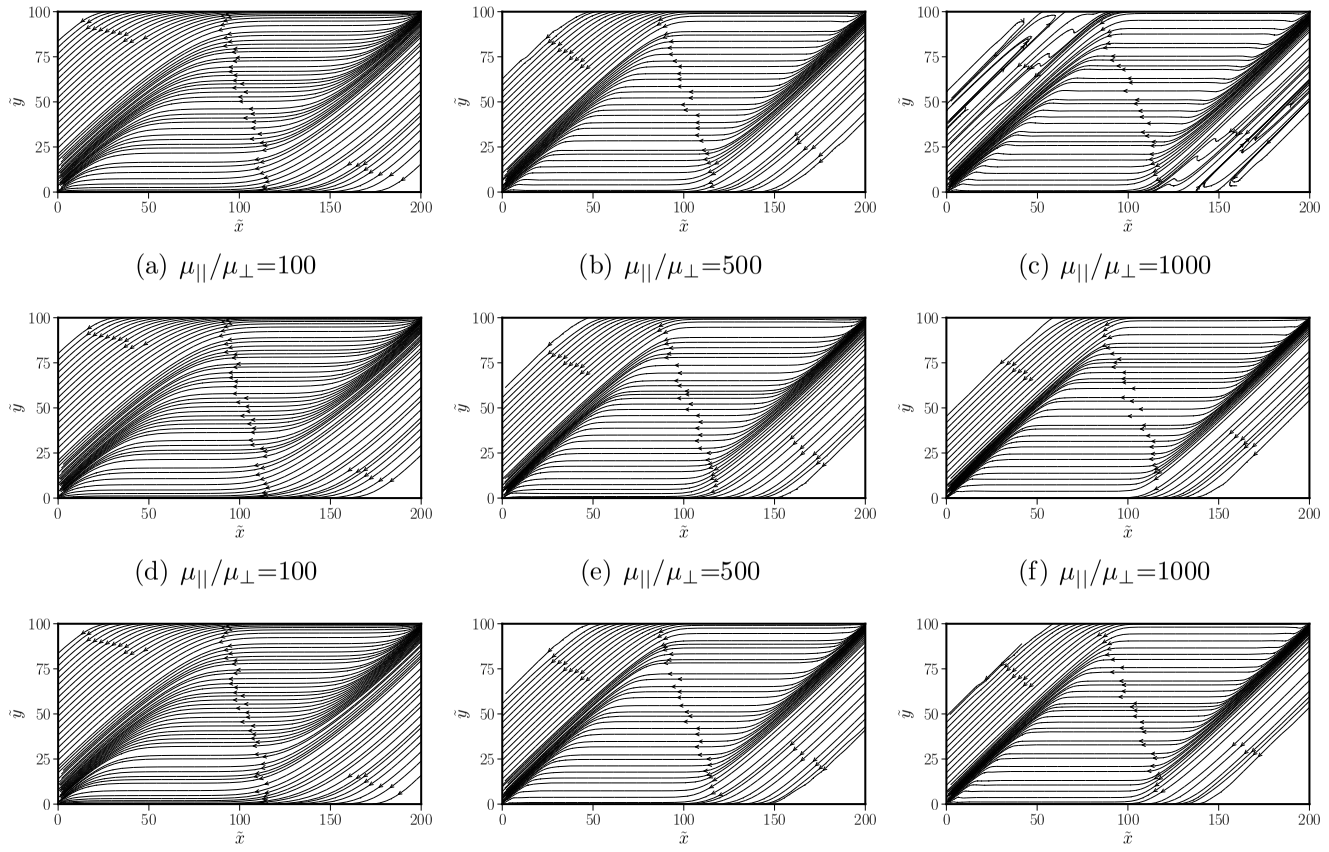

Figure 4.3: Comparison of velocity streamlines with increasing strength of magnetic confinement on a grid of 192 × 96. Top row: Upwind-3E; middle row: Upwind-5C; bottom row: Upwind-5E.

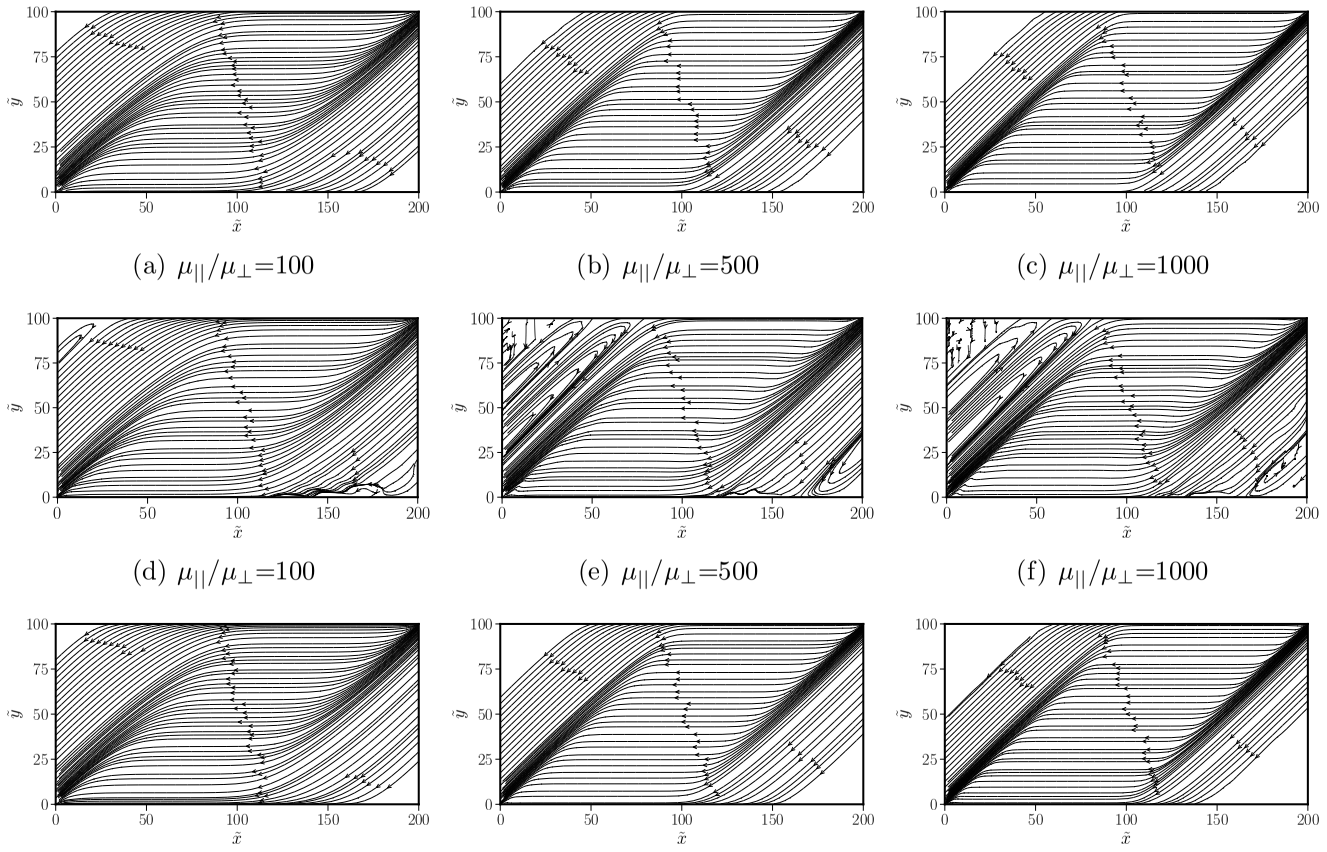

(a) $\mu_{||}/\mu_{\perp}$=100 (b) $\mu_{||}/\mu_{\perp}$=500 (c) $\mu_{||}/\mu_{\perp}$=1000

(d) $\mu_{||}/\mu_{\perp}$=100 (e) $\mu_{||}/\mu_{\perp}$=500 (f) $\mu_{||}/\mu_{\perp}$=1000

(g) $\mu_{||}/\mu_{\perp}$=100 (h) $\mu_{||}/\mu_{\perp}$=500 (i) $\mu_{||}/\mu_{\perp}$=1000

Figure 4.4: Comparison of velocity streamlines with increasing strength of magnetic confinement on a grid of 192 × 96. Top row: MFAM; Middle row: Generalized-MUSCL; bottom row: WENO-5Z-L.

We see from a series of Figs. $4.5(a) - 4.6(i)$, that there can be serious numerical oscillations in the solutions of the flow field with increasingly strong magnetic confinement. The main reason is not only the anisotropic diffusion itself but also because of the sharp gradients that are not aligned with the grid. In Fig. 4.6(c), MFAM approach do not show such behavior through an alignment of field lines with the grid and thereby captures the sharp gradient without numerical oscillations. If the angle between the field lines and the mesh is aligned, even the central scheme could also be easily implemented. As the gradient becomes more and more skewed, it diverges much more from the grid lines, thereby generating larger oscillations, as seen in Fig. 4.5(c). WENO-5Z was able to capture the gradients without significant oscillations as the disturbances in the y-velocity are minimal when the solution has reached the steady state.

Steady state solutions obtained for linear upwind schemes indicate that the disturbances behind the strong gradient have polluted the entire domain but similar to the boundary layer problem the solutions may be reduced with finer grids. Solutions obtained for diffusion, advection-diffusion, and magnetized electrons are indicating that the TVD- type schemes are not effective for the first order hyperbolic approach.

The oscillations due to sharp gradients can be drastically reduced with finer meshes by WENO-5Z. Even though MFAM approach did not show any spurious oscillations, such alignment may not be practical in many simulations with multiple sharp gradients. Furthermore, the boundary conditions and coding can be challenging to implement. Based on these simulations we can say that the non-oscillatory approach of WENO can be a reasonable and viable alternative.

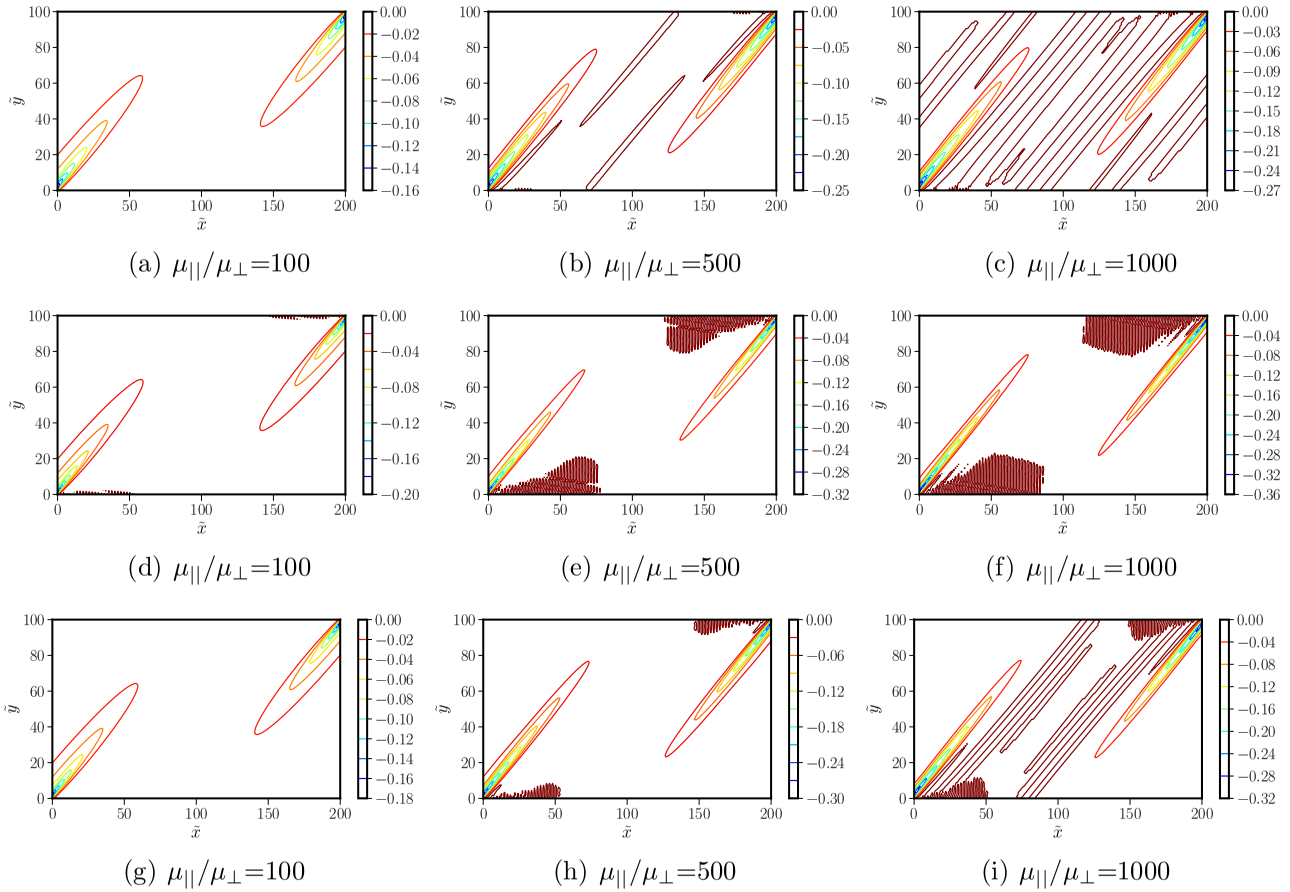

(a) $\mu_{||}/\mu_{\perp}$=100 (b) $\mu_{||}/\mu_{\perp}$=500 (c) $\mu_{||}/\mu_{\perp}$=1000

(d) $\mu_{||}/\mu_{\perp}$=100 (e) $\mu_{||}/\mu_{\perp}$=500 (f) $\mu_{||}/\mu_{\perp}$=1000

(g) $\mu_{||}/\mu_{\perp}$=100 (h) $\mu_{||}/\mu_{\perp}$=500 (i) $\mu_{||}/\mu_{\perp}$=1000

Figure 4.5: Comparison of normalized velocity in y-direction with increasing $\mu_{||}/\mu_{\perp}$on a 192 × 96 grid. Top row: Upwind-3E; middle row: Upwind-5C; bottom row: Upwind-5E.

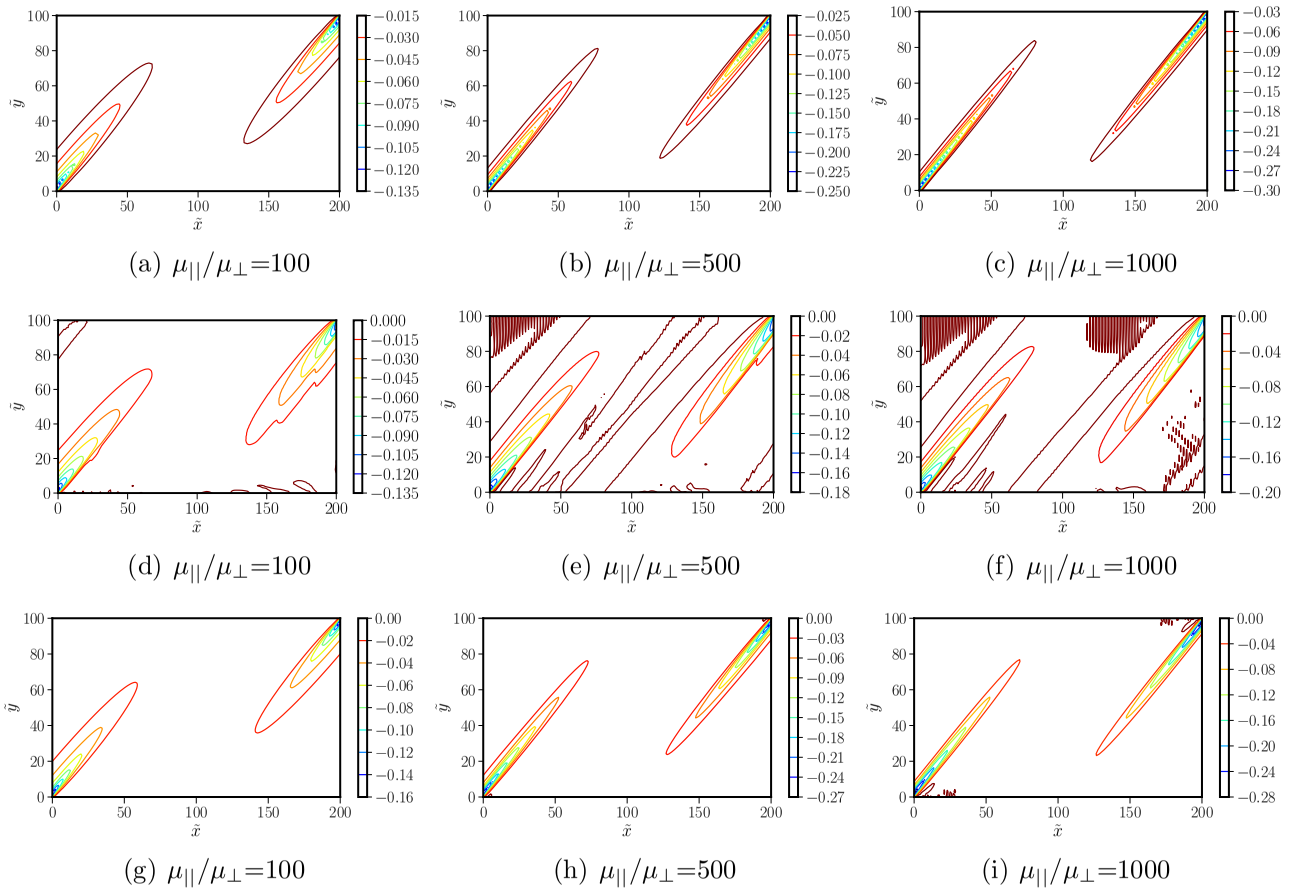

(a) $\mu_{||}/\mu_{\perp}$=100 (b) $\mu_{||}/\mu_{\perp}$=500 (c) $\mu_{||}/\mu_{\perp}$=1000

(d) $\mu_{||}/\mu_{\perp}$=100 (e) $\mu_{||}/\mu_{\perp}$=500 (f) $\mu_{||}/\mu_{\perp}$=1000

(g) $\mu_{||}/\mu_{\perp}$=100 (h) $\mu_{||}/\mu_{\perp}$=500 (i) $\mu_{||}/\mu_{\perp}$=1000

Figure 4.6: Comparison of normalized velocity in y-direction with increasing $\mu_{||}/\mu_{\perp}$on a 192 × 96 grid. Top row: MFAM; Middle row: Generalized-MUSCL; bottom row: WENO-5Z-L.

Similar patterns are also observed in potential distributions shown in Fig. 4.7. The maximum principle is violated as a consequence of these spurious oscillations as we can see the values of space potential are more than the theoretical bounds defined by the boundary conditions. Although the values are relatively smaller, it should be noted that the values are non-dimensionalized and the actual error can be much higher. On coarse grids, the entire domain can be polluted with unphysical extrema. The grid size of 192 × 96 is chosen in Fig. 4.7 is to reiterate the fact that the spurious oscillations can be reduced by the linear upwind schemes whereas they remain the same for the Generalized-MUSCL. Spurious oscillations in potential are comparatively smaller in the compact scheme than that of explicit schemes. As

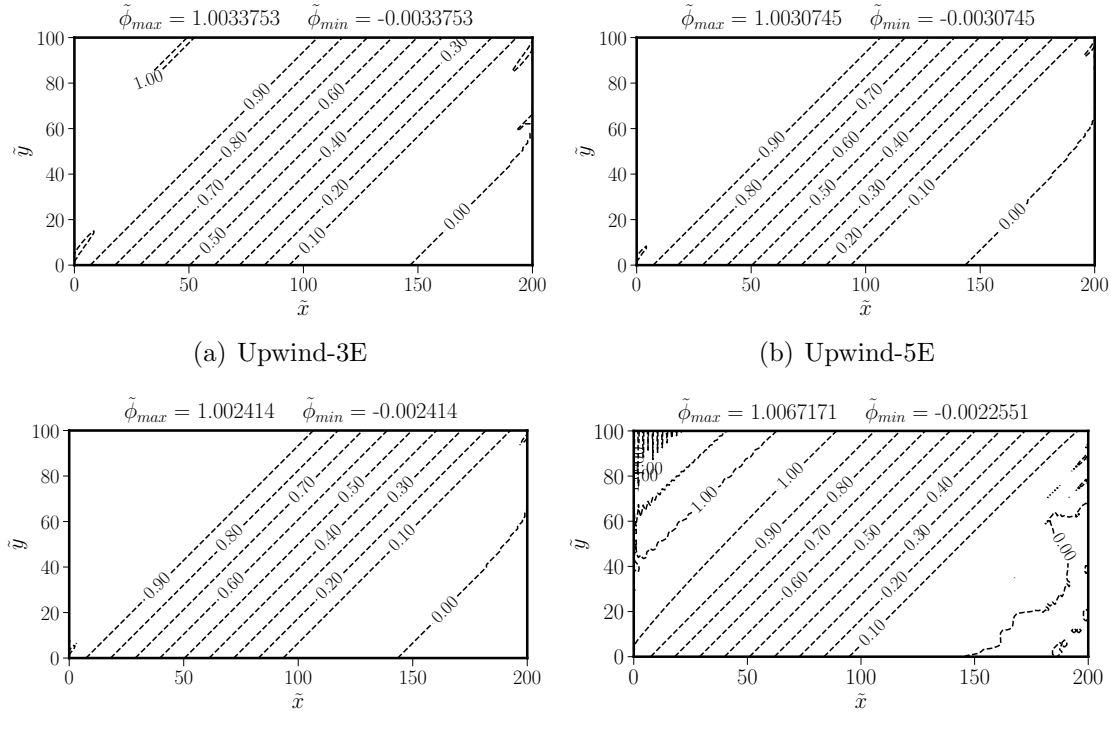

(a) Upwind-3E

(b) Upwind-5E

(c) Upwind-5C

(d) Generalized-MUSCL

Figure 4.7: Distribution of dimensionless space potential, calculated by using various schemes on a grid of 192 × 96 for $\mu_{||}/\mu_{\perp}$=1000.

explained earlier, the steady state is considered to be reached when the L_1 norms

attain negligibly small values in the order of 10^{-12}, that are defined by Eq. (4.23)

$$L_1 = \sqrt{\frac{1}{N_{\text{cell}}} \sum^{N_{\text{cell}}} (|Q^{n+1} - Q^n|)}, \tag{4.23}$$

where Q denotes each of the conservative variables $(\tilde{\phi}, \tilde{u}_{\text{x}}, \tilde{u}_{\text{y}})$. The convergence history of space potential for various schemes is shown in Fig. 4.8 when the test problem is calculated on a 192 × 96 grid. The residuals are monotonically decreasing and reached the limit as mentioned earlier for all the linear upwind schemes and WENO scheme. For the Generalized MUSCL scheme, the residual does not converge beyond four orders of magnitude.

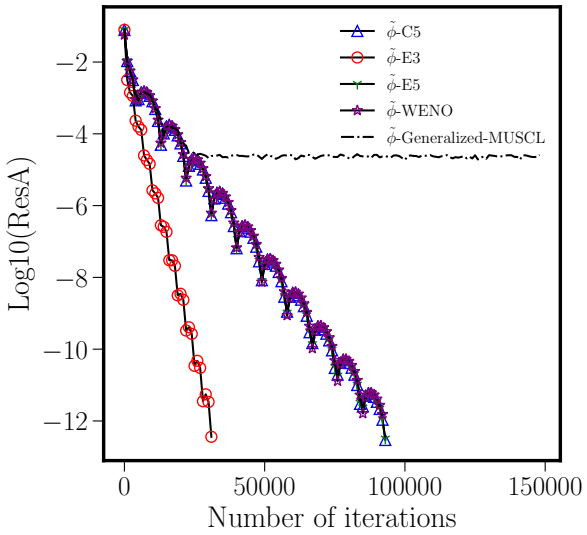

Figure 4.8: Convergence histories by all the upwind schemes on a grid size of 192 × 96 for $\mu_{||}/\mu_{\perp}$=1000 and θ =45°.

4.2.1 Effect of boundary conditions

Simulations carried out by WENO-5Z along with Lagrange extrapolation, WENO-5Z-L, for ghost cells are free of spurious values in space potential if $\mu_{||}/\mu_{\perp} \leq 500$. But with increasingly higher anisotropies small overshoots and undershoots, similar to those that are observed in linear upwind schemes, are also found in the cells next

to the boundary. By keeping the objective of the uniform grid, WENO extrapolation method, WENO-5Z-W, is used for computing the values in ghost-cells. The WENO-5Z-W scheme was able to adaptively reduce to lower accurate order boundaries and thereby prevented the unphysical oscillations in the flow field, as shown in Fig. 4.9. WENO extrapolation approach was also tested for smaller anisotropies, and

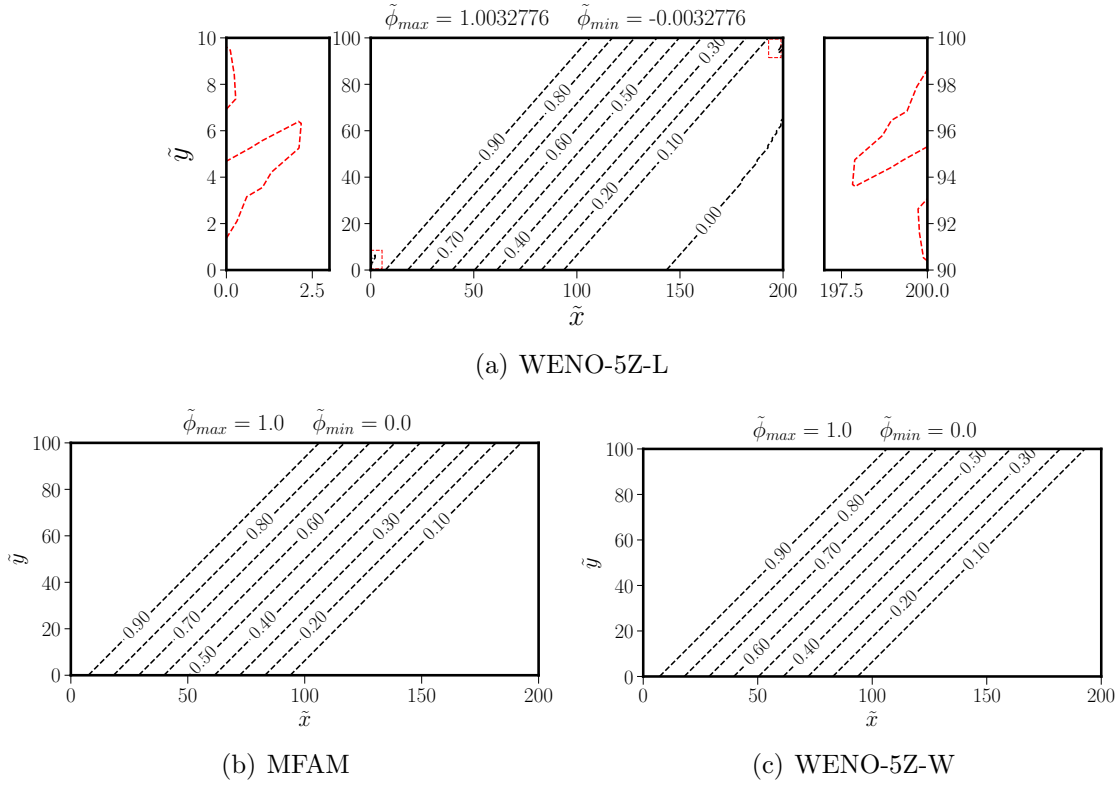

(a) WENO-5Z-L

(b) MFAM

(c) WENO-5Z-W

Figure 4.9: Distribution of dimensionless space potential computed by WENO extrapolation and Lagrange extrapolation in comparison with MFAM for $\mu_{||}/\mu_{\perp}$=1000 on a grid of 96 × 96. Dotted regions are enlarged and shown in Fig. 4.9(a).

the results indicated that the performances are similar to that of WENO-5Z-L and no unphysical extrema are generated. The minimum grid size required for WENO-5Z-W scheme to prevent unphysical extrema in space potential distribution is 16 × 16 for $\mu_{||}/\mu_{\perp} \leq 500$ and 96 × 96 if $\mu_{||}/\mu_{\perp} > 500$. Test calculations are also carried out for the cases when the magnetic field lines are aligned at an angle 60° from the vertical and even for complicated shapes constructed using the magnetic stream function, shown in Fig. 4.10(c). These results further confirm the fact that the WENO scheme

has better capabilities in capturing the sharp gradients without spurious oscillations even for complex magnetic field shapes shown 4.10(d) and 4.10(e).

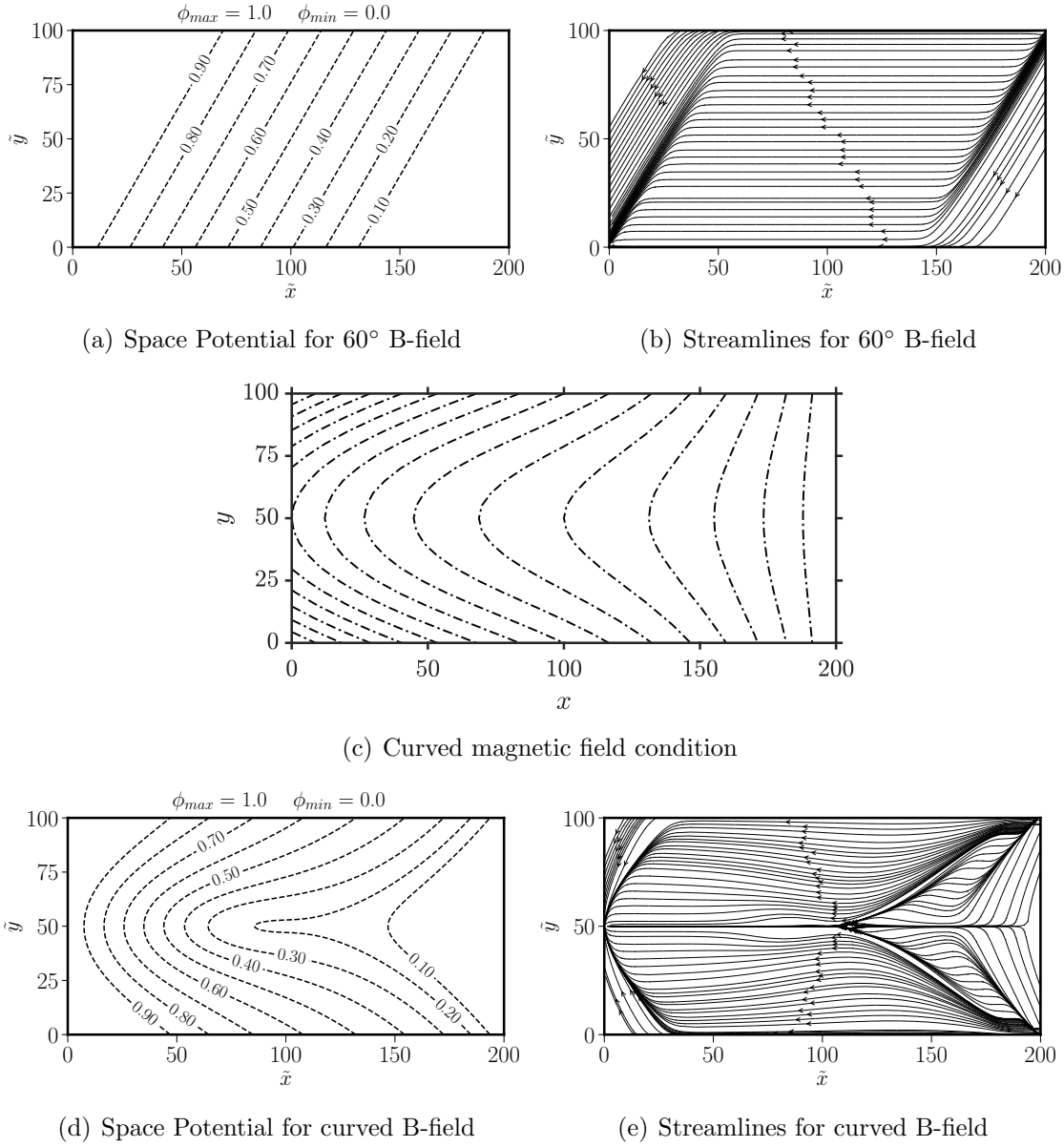

(a) Space Potential for 60° B-field

(b) Streamlines for 60° B-field

(c) Curved magnetic field condition

(d) Space Potential for curved B-field

(e) Streamlines for curved B-field

Figure 4.10: (a) and (b) Distribution of dimensionless space potential and streamlines for constant angle of 60°, (c) Curved magnetic field lines test case, (d) and (e) Distribution of dimensionless space potential and streamlines for curved magnetic field shape, computed by WENO-5Z-W on a grid of 96 × 96 for $\mu_{||}/\mu_{\perp}$=1000.

4.2.2 Mesh convergence and accuracy for electron fluids

The computational accuracy of anisotropic diffusion by HES approach is compared with that of MFAM by using the transverse electron flux which is defined as the total electron flux from right to left boundary given by Eq. (4.24),

$$\Gamma_{\mathrm{e}} = \int_{\Omega_L} (\tilde{u}_{\mathrm{e,x}})\, d\tilde{y}, \tag{4.24}$$

where Ω_L is the left boundary of the calculation field. The grid convergence of the calculated electron transverse flux is evaluated only for WENO-5Z-W and MFAM schemes as for the other schemes the solution is polluted due to spurious oscillations and might not be appropriate. Table 4.1 shows the difference between computed transverse electron fluxes by both the approaches. The error reduces from 1.12% to 0% on mesh refinement. Another criteria considered is the relative numerical error,

Table 4.1: Error in transverse electron flux for $\mu_{||}/\mu_{\perp}$=1000 and $\theta = 45°$.

Number of points	WENO-5Z-W		MFAM	
	Γ_{e}	Error %	Γ_{e}	Error %
96×48	-0.01861	1.12	-0.01878	0.21
192×96	-0.01878	0.21	-0.01879	0.16
384×192	-0.01881	0.05	-0.01882	0.0
768×384	-0.01882	0.0	-0.01882	0.0

$|l_2|$ error, which is defined as

$$|l_2| = \frac{1}{n}\left(\sum\left(\frac{Q_{WENO} - Q_{MFAM}}{Q_{MFAM}}\right)^2\right)^{0.5}, \tag{4.25}$$

where Q is each of the conservative variable. The relative errors are calculated in comparison with the field aligned mesh results. The Table 4.2 show thew relative l_2 errors computed for field aligned mesh and WENO-5Z-W and the results show that the solution seems to improve with finer grid resolution.

Table 4.2: Relative l_2 error for MFAM and WENO-5Z-W for $\mu_{||}/\mu_{\perp}$=1000.

Number of points	$\tilde{\phi}$	$\tilde{u}_x$	$\tilde{u}_y$
96×48	3.28E-03	1.01E-02	1.03E-02
192×96	2.62E-03	9.92E-03	1.02E-02
384×192	1.73E-03	8.71E-03	8.92E-03
768×384	9.82E-04	8.12E-03	8.35E-03

4.3 Summary

The important findings of this chapter are summarized as follows

1. Spurious oscillations due to sharp gradients are significantly reduced by using high-order schemes. For small anisotropies, linear upwind schemes as well as TVD-MUSCL employed can be appropriate. TVD schemes cannot reduce the oscillations for the magnetized electron fluids computations.

2. WENO approach is found to be more suitable and robust to reduce the spurious oscillations associated with the sharp gradients with increasing anisotropic diffusion in magnetized electrons. Significant improvement is achieved by utilizing WENO schemes for the simulation of magnetized electron fluids as the results are much closer to the field-aligned mesh.

3. Boundary conditions based on WENO extrapolation are found more appropriate to prevent unphysical extrema for anisotropies higher than 500.

4. For very high anisotropic diffusion problems, $\mu_{||}/\mu_{\perp}$ of the order from 10^4 to 10^9 that can be seen in practical applications like tokamaks and space propulsion devices, all the schemes would result in spurious oscillations on coarse meshes, say 96×96, and reducing such oscillations is the subject of future work.

CHAPTER V

Hyperbolic approach for Advection-Diffusion equation

Convection and diffusion are the two major transport phenomenon in fluid flow and most of the governing equations involve modeling the these processes. Convection and diffusion terms appear in energy equation of the magnetized plasma equations and this chapter is a preliminary step in that direction. The convection process is modeled using first-order spatial derivatives and various types of upwind schemes developed for the hyperbolic type of equations. On the other hand, diffusion terms are generally modelled using second-order spatial derivatives. In the previous chapter, high-order upwind schemes are presented for diffusion equation via hyperbolic system approach. Therefore, it is natural to unify the convection and diffusion terms and model them by a single scheme. In this chapter the first order hyperbolic approach is extended further to advection-diffusion equation.

5.1 Governing equations and construction of hyperbolic scheme

In this section, consider the advection-diffusion equation,

$$\frac{\partial u}{\partial t} + a\frac{\partial u}{\partial x} + b\frac{\partial u}{\partial y} = \nu(\frac{\partial^2 u}{\partial x^2} + \frac{\partial^2 u}{\partial y^2}), \tag{5.1}$$

where where u is the solution variable, (a,b) is a constant advection vector, and ν is a constant positive diffusion coefficient. Similar to the diffusion equation new variables $p = \frac{\partial u}{\partial x}$ and $q = \frac{\partial u}{\partial y}$ are defined and pseudo-time derivatives are introduced to obtain the following first order hyperbolic system:

$$\begin{aligned} \frac{\partial u}{\partial \tau} + a\frac{\partial u}{\partial x} + b\frac{\partial u}{\partial y} &= \nu(\frac{\partial p}{\partial x} + \frac{\partial q}{\partial y}), \\ \frac{\partial p}{\partial \tau} - \frac{\partial u}{\partial x} &= -p, \\ \frac{\partial q}{\partial \tau} - \frac{\partial u}{\partial y} &= -q. \end{aligned} \tag{5.2}$$

The Eq.(5.2) can be represented in vector form as,

$$\frac{\partial \mathbf{Q}}{\partial \tau} + \frac{\partial \mathbf{E_x}}{\partial x} + \frac{\partial \mathbf{E_y}}{\partial y} = \mathbf{S}, \tag{5.3}$$

where the conservative variables, fluxes in x and y-direction and source terms are,

$$\mathbf{Q} = \begin{bmatrix} u \\ p \\ q \end{bmatrix}, \mathbf{E_x} = \begin{bmatrix} au - \nu p \\ -u \\ 0 \end{bmatrix}, \mathbf{E_y} = \begin{bmatrix} bu - \nu q \\ 0 \\ -u \end{bmatrix}, \quad \mathbf{S} = \begin{bmatrix} 0 \\ -p \\ -q \end{bmatrix}, \tag{5.4}$$

respectively. The split hyperbolic formulation introduced by Nishikawa in Ref. [5] is considered in this section. The advection, E_x^a, and diffusion, E_x^d, fluxes in x-direction are separated as

$$\mathbf{E_x} = \mathbf{E_x^a} + \mathbf{E_x^d} = \begin{bmatrix} au \\ 0 \\ 0 \end{bmatrix} + \begin{bmatrix} -\nu p \\ -u \\ 0 \end{bmatrix}. \tag{5.5}$$

The absolute Jacobian matrix for the diffusive fluxes would be the same as in Eq. (3.7), which is written here for connivence, and the corresponding absolute Jacobian

matrix for the advection flux is straightforward,

$$|\mathbf{J_{ax}}| = \begin{bmatrix} |a| & 0 & 0 \\ 0 & 0 & 0 \\ 0 & 0 & 0 \end{bmatrix}. \quad |\mathbf{J_{dx}}| = \sqrt{\nu} \begin{bmatrix} 1 & 0 & 0 \\ 0 & 1 & 0 \\ 0 & 0 & 0 \end{bmatrix}. \tag{5.6}$$

and finally, the upwind flux can be constructed as,

$$\hat{E}_{i+\frac{1}{2},j} = \frac{1}{2}(\mathbf{E_L} + \mathbf{E_R}) - \frac{1}{2}|\mathbf{J_{dx}} + \mathbf{J_{ax}}|(\mathbf{Q_R} - \mathbf{Q_L}) \tag{5.7}$$

The upwind fluxes can also be constructed by the unified advection-diffusion approach proposed by Nishikawa in Ref. [4] and the numerical schemes presented here can be used in a straight forward manner and is discussed later.

5.2 Boundary conditions

Similar to the diffusion and anisotropic diffusion equations the Dirichelt boundary conditions are employed through Lagrange extrapolation. In this section outflow boundary conditions are also considered which are set as follows:

$$U_{-1} = U_0 = U_1 \tag{5.8}$$

5.3 Numerical tests

For the advection-diffusion equation, the numerical solutions are computed on a uniform Cartesian mesh. For the linear upwind schemes, depending on the order of the interior interpolation the corresponding r^{th} order extrapolation polynomial is used for the ghost boundary conditions. For WENO scheme both Lagrange and WENO extrapolations are considered for boundary conditions.

5.3.1 One-dimensional test cases

Example 5.1. The following one dimensional-advection diffusion equation is considered with the spatial domain of [0,1] and $u(0) = 0$ and $u(1) = 1$

$$u_\tau + au_x = \nu u_{xx} + s(x), \tag{5.9}$$

where, $s(x) = \pi Re[a\cos(\pi x) + \pi\nu sin(\pi x)$ and the Reynolds number, $Re = \frac{a}{\nu}$. The exact steady state solution is given by

$$u_{exact}(x) = \frac{exp(-Re) - exp(xRe - Re)}{exp(-Re) - 1} + \frac{\sin(\pi x)}{Re}. \tag{5.10}$$

The exact solution is a smooth sine curve for low Reynolds numbers, which are diffusion dominant, and develops a sharp gradient close to the boundary for high Reynolds numbers when advection becomes the dominant effect. The main objective of this test case to verify the design accuracy and implementation of the numerical schemes and also to show the advantage of WENO scheme over TVD-MUSCL in capturing the sharp gradients. The simulations are conducted on a uniform grid with grid refinements from $N = 8$ to 256 by all the upwind schemes. The numerical solution is computed by an explicit time-marching until the residuals are dropped below 10^{-10} in L_1 norm. A constant value of CFL is considered depending on the order of the scheme. Simulations are carried out for three Reynolds numbers: $Re = 0.1, 1, 10$.

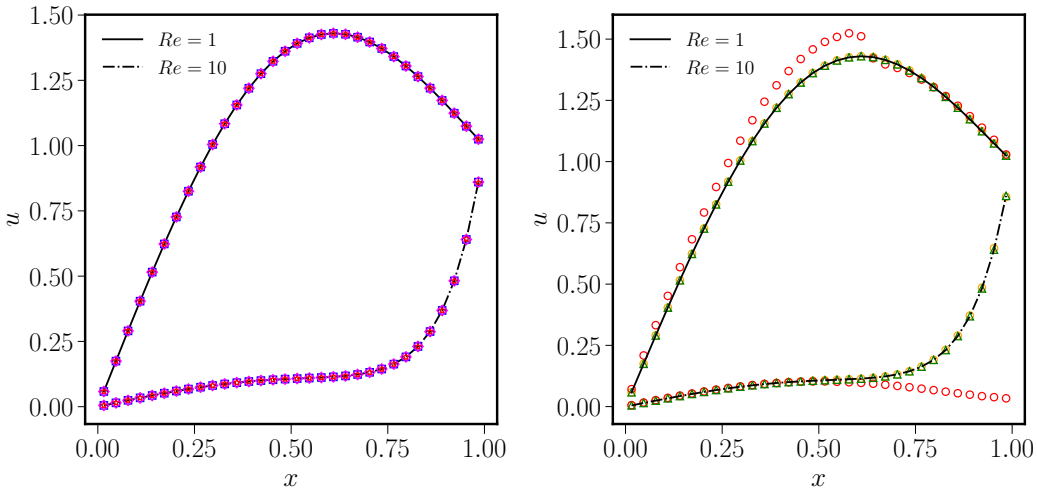

(a) Linear schemes

(b) Shock-capturing schemes

Figure 5.1: Numerical solutions obtained by using different schemes for $Re = 1$ and 10 for Example 5.1. Red circles: Generalized-MUSCL; purple stars: U-3E; orange squares: TVD-MUSCL; blue squares: U-5C; magenta diamonds: U-5E; green triangles: WENO-5Z.

Fig. 5.1 shows the solutions contours of various schemes in comparison with the analytical solution for the primary variable, u. From Fig. 5.1(b), it is obvious to notice that the Generalized MUSCL scheme can pollute the smooth profile whereas TVD-MUSCL reduces to linear 3rd order scheme. For Re = 1 there were unnecessary oscillations in the profile, and for the Reynolds number of 10, even though there are no oscillations, the sharp gradient has been completely cut-off. Numerical results obtained by linear upwind schemes were, in fact, better than the results obtained by Generalized MUSCL scheme. The design order of accuracy is obtained for all the schemes and all the Reynolds numbers and is shown in Fig. 5.2. The 5th order compact scheme is one order of magnitude more than the design accuracy for $Re = 0.1$.

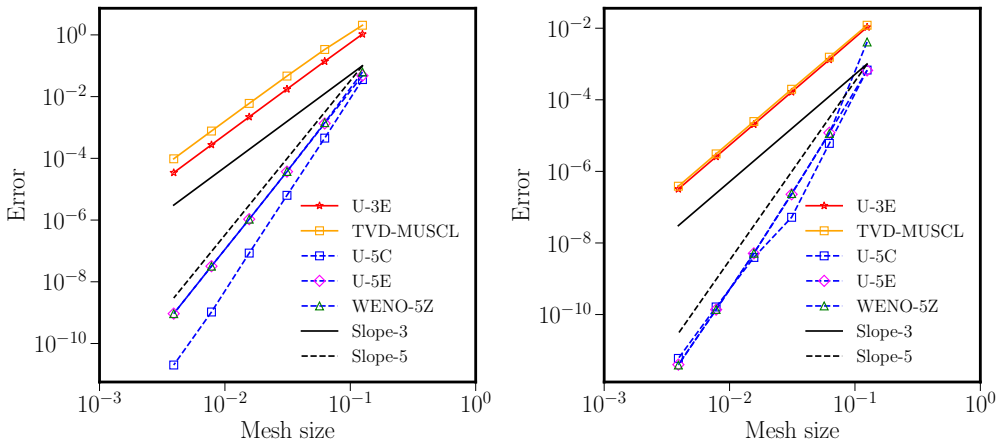

(a) $Re = 0.1$ (b) $Re = 1$

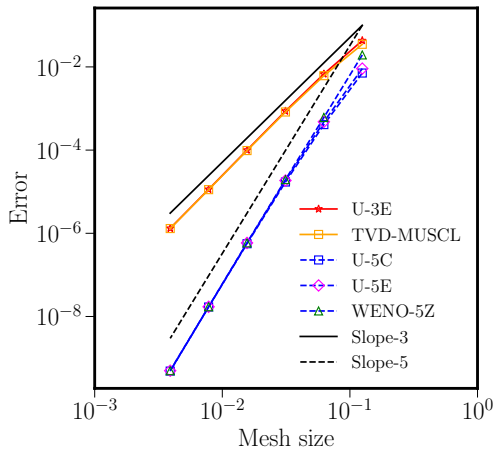

(c) $Re = 10$

Figure 5.2: Convergence of the L_2 error for upwind schemes for $Re = 0.1$, 1 and 10 for Example 5.1.

5.3.2 High-Reynolds number flows and Péclet number

The impact of convection and diffusion on the transport of a physical quantity is measured by the cell Reynolds number or the local Péclet number (Pe), which is defined as the ratio of convective flux to diffusive flux, To obtain the solution without oscillations in the case of high-Re, extremely fine grids are required to meet the well-known requirement on the mesh Reynolds-number, i.e., $Re < 2$, as explained by Nishikawa [4]. Computations are carried out by Nishikawa on substantially coarser

grids by grid stretching to meet the criteria. In this test case, the non-oscillatory schemes, WENO, are incorporated to capture the sharp gradients without oscillations on uniform meshes which might not satisfy the mesh Reynolds-number requirement. Simulations carried out for the Reynolds number of 500 on a uniform grid size of 256 has been shown in Fig. 5.3.

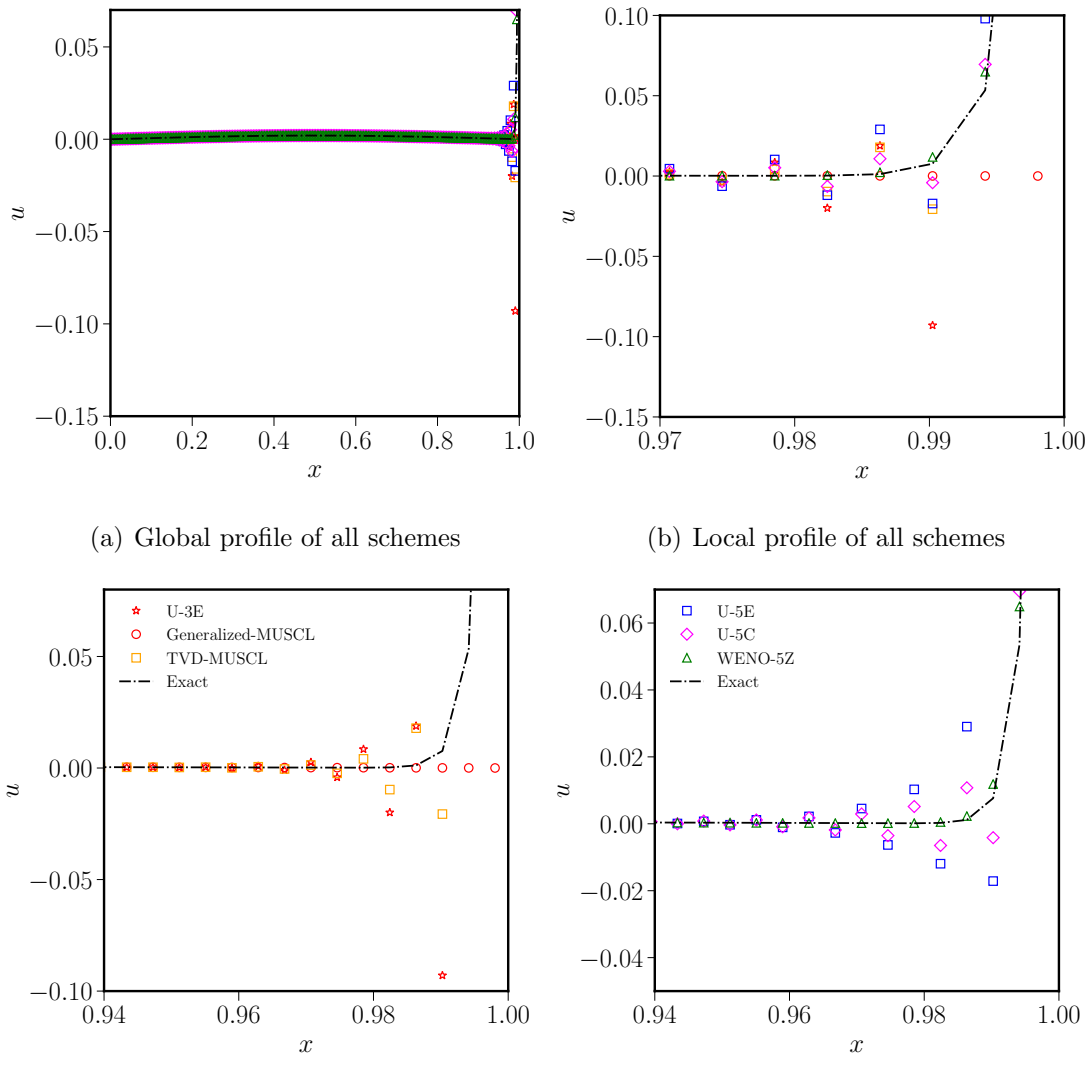

(a) Global profile of all schemes

(b) Local profile of all schemes

(c) Local profile third order schemes

(d) Local profile fifth order schemes

Figure 5.3: Numerical and exact (dotted line) solutions obtained by various schemes for $Re = 500$ on a grid of 256 points.

Generalized MUSCL scheme did not show any oscillations but completely cut-off

the sharp gradient and thereby failing to capture it. On the other hand TVD-MUSCL has reduced oscillations compared to that of linear 3rd order scheme. Oscillations are also observed in both 5th order schemes. However, the amplitude of the oscillations is much smaller for the compact scheme than the explicit scheme as expected. Finally, sharp gradient developed at $x = 1$ is easily captured by WENO scheme without spurious oscillations as shown in Fig. 5.3(d). Also, it is important to note that the linear schemes can also give oscillation free solutions on dense grids by satisfying the mesh-Reynolds number criteria. These important inferences were found to be useful for the simulation of magnetized electrons which can develop sharp gradients with increasing strength of magnetic confinement.

5.3.3 Two-dimensional test cases

Example 5.2. The two-dimensional advection-diffusion equation is solved by split flux approach for two test cases.

$$u_\tau + au_x + bu_y = \nu(u_{xx} + u_{yy}), \text{in domain (x,y)} \in [0,1] \times [0,1] \tag{5.11}$$

1. The first test case is an advection-dominated problem considered by Nishikawa and Liu [9] which has the following exact solution,

$$u_{exact}(x, y) = \cos(2\pi\eta) \exp\left(\frac{8^2\pi^2\mu\xi}{1 + \sqrt{1 + 16\pi^2\nu^2}}\right), \tag{5.12}$$

where ξ = ax + by, η = bx - ay and the viscosity, $\nu = 0.1$. The advection vector (a, b) is given by $(1.0, 1.0)$. This exact solution is given by Eq. (5.12) is very smooth and therefore can be used to verify the accuracy of numerical schemes. For the right boundary, outflow boundary conditions are used for this test case.

2. For the second test case the following exact solution is considered,

$$u_{exact}(x, y) = \cos(\pi\eta) \exp\left(\frac{-0.5\xi(1 + \sqrt{1 + 4^2\pi^2\nu^2})}{\nu}\right), \tag{5.13}$$

where the viscosity coefficient is $\nu = 0.1$, and the advection vector (a, b) is given by $(7.0, 4.0)$ respectively. This test case was originally proposed by Nishikawa and Roe in [68], where both advective and the diffusive terms are equally important which may exist in the middle of the boundary layer.

Computations are carried out with grid refinements from 8×8 to 128 × 128 for both the test cases. For all the numerical schemes, the simulations are carried out until the residuals are dropped below 10^{-14} in L_1 norm and CFL is dependent on the numerical scheme used, which is in between from 0.3 to 0.7. Both WENO extrapolation denoted as WENO-5Z-W, and Lagrange extrapolation, WENO-5Z-L, are implemented for the numerical boundary conditions for the WENO scheme, which are 3rd order accurate. Figures 5.4(a) and 5.4(b) show the velocity contours obtained by the upwind scheme, U-5E, for both the test cases on a 48 × 48 grid.

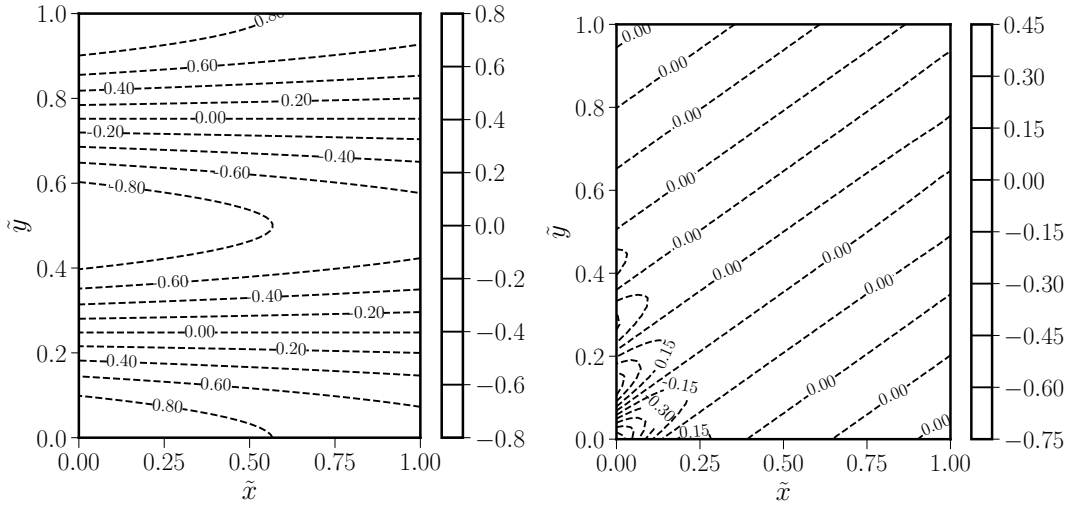

(a) Case-1 (b) Case-2

Figure 5.4: Comparison of velocity contours, on a grid size of 48 × 48, for test conditions given by Example 5.2.

Design accuracy is obtained for all the linear upwind schemes, shown in Fig. 5.5(a) and the implementation of boundary conditions for advection dominated problem are verified through this test case. First the first test condition, WENO scheme is third accurate for both WENO and Lagrange type extrapolations which is unlike the one-dimensional test case where the WENO scheme was fifth order accurate.

The second test case was found to be more challenging than the advection-dominant flow. Design accuracy is obtained for all the linear upwind schemes, shown in Fig. 5.5(b). For the WENO scheme, the WENO extrapolation technique for the boundary conditions was observed to be first order accurate whereas the Lagrange extrapolation is 3rd order accurate similar to the advection-dominated problem. Table 5.1 show the L_2 norms for both the test cases for both WENO implementations.

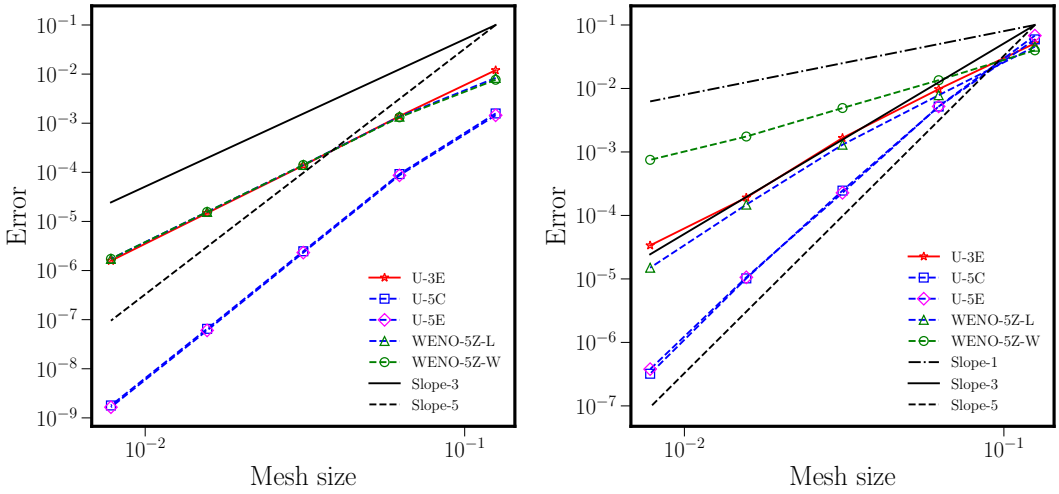

(a) Advection dominated (b) Both Advection-Diffusion dominant

Figure 5.5: Convergence of the L_2 error for all the upwind schemes for both the test conditions in Example 5.2.

Table 5.1: L_2 errors and order of convergence for Example 5.2 by using WENO scheme along with WENO and Lagrange extrapolation techniques for boundary conditions.

Number of points	Advection				Advection-Diffusion			
	WENO-5Z-L		WENO-5Z-W		WENO-5Z-L		WENO-5Z-W	
	error	order	error	order	error	order	error	order
8^2	7.52E-05		6.90E-05		4.55E-02		3.99E-02	
16^2	1.22E-05	2.62	1.19E-05	2.53	7.83E-03	2.54	1.35E-02	1.56
32^2	1.27E-06	3.27	1.27E-06	3.23	1.30E-03	2.59	4.92E-03	1.45
64^2	1.40E-07	3.18	1.40E-07	3.18	1.48E-04	3.14	1.75E-03	1.49
128^2	1.56E-08	3.17	1.56E-08	3.17	1.50E-05	3.30	7.51E-04	1.22

Example 5.3. In this test case, the steady state problem of the two-dimensional advection-diffusion equation is considered, with boundary layers along x = 1 and y = 1, considered by Chou and Shu [69] which has the following exact solution given by

$$u_{exact}(x, y) = e^{\frac{x-1}{\nu}+\frac{y-1}{\nu}}. \tag{5.14}$$

The viscosity coefficient ν is taken as 0.05, and the exact solution is imposed on the boundaries. Linear upwind schemes are not considered for this problem as they will produce spurious oscillations. Figure 5.6 shows the three-dimensional numerical solution contour. The numerical results are shown in Table 5.2 indicate that the third order accuracy is obtained for WENO-5Z-L whereas the accuracy of WENO-5Z-W is reduced to first order. This test case demonstrates that the WENO scheme can resolve the boundary layers by using first-order hyperbolic approach.

Table 5.2: L_2 errors and order of convergence for Example 5.3 by using WENO scheme along with WENO and Lagrange extrapolation techniques for boundary conditions.

Number of points	WENO-5Z-W		WENO-5Z-L	
	error	order	error	order
20^2	2.21E-03		1.91E-03	
40^2	1.07E-03	1.04	2.00E-04	3.26
80^2	4.60E-04	1.22	2.34E-05	3.09
160^2	1.99E-04	1.21	2.59E-06	3.18
320^2	9.06E-05	1.14	2.68E-07	3.27

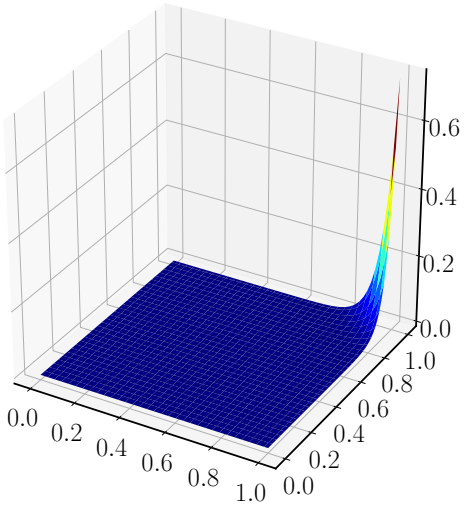

Figure 5.6: Three-dimensional plot of numerical solution by WENO scheme with 64×64 cells Example 5.3.

5.4 Summary of the chapter

- First order hyperbolic approach developed for diffusion equation is extended to advection-diffusion equation.

- All the upwind schemes are consistently high-order accurate for all the problems. For smooth solutions compact schemes have better accuracy than explicit schemes.

- An important contribution in this chapter is the successful implementation of weighted non-oscillatory schemes to capture the sharp gradients without spurious oscillations for boundary layer type problem for advection-diffusion equation.

CHAPTER VI

Conclusions

6.1 Summary

In this thesis, high-order schemes using a hyperbolic approach are proposed for diffusion dominated flows. Several new tools, like boundary conditions and new hyperbolic formulations, are developed and described in this thesis. Various problems encountered are examined in detail and resolutions are discussed.

In chapter-3 high-order and high-resolution methods for the diffusion equation in the hyperbolic form on uniform meshes are proposed and investigated. Design order of accuracy is obtained for all the schemes for all the test problems considered. Shock-capturing schemes are found to be unnecessary for simple diffusion equation, and through various test cases, the inapplicability of specific TVD schemes is explained. In particular Generalized MUSCL scheme is found to be unsuitable. Even though the WENO scheme is a shock-capturing scheme the steady-state solutions are not contaminated and are similar to the linear upwind schemes. Ghost cell approach is found to be more accurate and stable than the weak boundary implementation, especially on coarse meshes. Linear upwind schemes are consistently stable with the corresponding higher order boundary conditions whereas WENO schemes were stable only with reduced order boundary conditions due to their inherent non-linearity. Appropriate relaxation time and length scales are found to be important for dimensional

equations and design accuracy is also achieved such problems. Fifth or higher order schemes are recommended for diffusion equation in hyperbolic form.

In chapter-4 the hyperbolic approach for anisotropic diffusion equation is implemented. Firstly, the ideas and lessons learnt from isotropic diffusion are found useful for anisotropic diffusion equation. Significant improvement is achieved by utilizing WENO scheme for the simulation of magnetized electron fluids as the results are much closer to the field-aligned mesh. Similar to the boundary layer problem WENO approach is found to be more suitable and robust to reduce the spurious oscillations associated with the sharp gradients with increasing anisotropic diffusion in electron fluid equations. For small anisotropies, linear upwind schemes as well as TVD-MUSCL employed can be appropriate. Generalized MUSCL is found inappropriate for the magnetized electron fluids computations similar to the hyperbolic diffusion equation.

Secondly, an alternate formulation is proposed for the anisotropic transport equation with appropriate length scale, L_r, and relaxation time, T_r, and the numerical results indicate that the simulations are independent not only of degree of anisotropy and but also angle of misalignment. Preconditioned form of the hyperbolic system is found suitable for anisotropic diffusion with significant improvement in accuracy and steady state convergence. Consistent high-order accuracy was achieved for test cases with variable diffusion coefficients. Boundary conditions based on WENO extrapolation are found more suitable to prevent unphysical extrema, for both the formulations in case of sharp gradients, for anisotropies higher than 500. For very high anisotropic diffusion problems, $\mu_{||}/\mu_{\perp}$ from 10^4 to 10^9 that can be seen in practical applications like tokamaks and space propulsion devices, all the schemes resulted in spurious oscillations on coarse meshes, say 96×96.

In chapter-5 the hyperbolic approach is further extended to advection-diffusion equation. Design order of accuracy is obtained for all the higher order methods for

smooth solutions. Unlike the diffusion equation the compact schemes are slightly more accurate than explicit schemes. The advantage of compact schemes may be more pronounced if the current approach is extended to time-dependent problems and also to hyperbolic compressible and incompressible Navier-Stokes equations proposed by Nishikawa [70]. An important finding from chapter-5 is that the weighted essentially non-oscillatory schemes can capture the sharp gradients without spurious oscillations for boundary layer type problem for advection-diffusion equation, without grid stretching and satisfaction of mesh Reynolds number.

In conclusion, fifth order accurate results are obtained for various kinds of diffusion dominated flows by using appropriate boundary conditions and preconditioning method. Hy- perbolic approach along with these high-order upwind schemes are recommended for practical plasma simulations.

6.2 Recommendations for Future Work

During this research, several areas have been identified that can lead to further improvement of hyperbolic approach for diffusion and its applications

6.2.1 Optimum length scale for higher order schemes

Optimal values for length scale, L_r, and relaxation time, T_r, may be derived for the anisotropic diffusion equation by following the procedure described in Ref.[2]. In brief, we substitute a Fourier mode into the first-order version of the finite-difference scheme in the semi-discrete form to derive a pseudo-time evolution of the amplitude of the Fourier mode, and derive the optimal values by requiring that the eigenvalues of the evolution matrix become complex, so that the Fourier mode will propagate rather than purely get damped. By propagating the Fourier mode the scheme can have a property of removing errors by propagation along with damping. It may be

beneficial if they are derived for high-order schemes, 3^{rd} and greater.

6.2.2 Positivity preserving

Another important aspect of the anisotropic diffusion equation is the positivity of the temperature or space potential. A numerical scheme should be robust against the development of nonphysical negative temperatures during the simulation and must satisfy positivity and monotonicity. For example negative temperatures, T, in Hall thruster modeling can lead to decreased electron currents and negative Joule power density near the cathode region. A possible alternative to the nonlinear limiters is the high order positivity preserving WENO schemes developed by Zhang and Shu [71, 72] and Hu et al. [73] which are both high-order accurate and also positivity preserving at the same time. The numerical schemes may be developed along with the appropriate boundary conditions for consistent and accurate simulations.

All the numerical schemes presented in this thesis were one-dimensional, i.e. the reconstructions and interpolations are performed dimension by dimension, whereas the flow features are multidimensional. An alternative is to develop a truly multidimensional solver that incorporates the multi-dimensional effects which are also immune to mesh irregularities and alignment. Such schemes proposed in the literature, e.g. Residual Distribution schemes proposed in Ref. [2] for the hyperbolic approach of diffusion equation, multi-dimensional Riemann solver developed for Magnetohydrodynamics [74, 75], and high-order Residual distribution WENO schemes [69], can be explored. Combining Asymptotic preserving schemes and hyperbolic approach can be an alternative to mitigate the issue of positivity [21, 22].

6.2.3 Other system of equations

1. **Electron energy equation for magnetized electrons:** In this thesis the hyperbolic approach for magnetized electrons models only mass and momentum

conservation equations. To simulate plasma devices, the hyperbolic approach should include the energy conservation equation to obtain the electron temperature. Such a model proposed by Kawashima et al. [30] constructs the upwind fluxes by using the flux vector splitting approach. It may be interesting to develop a method based on Roe solver proposed in this thesis to compare the two approaches. Also, optimal values for the relaxation time, T_r, and length scales, L_r, discussed in earlier chapters may be explored further for improved accuracy and faster convergence.

2. **Compressible Navier-Stokes equations:** The non-oscillatory schemes implemented for advection-diffusion equation readily extended to Navier-Stokes equations. It may be particular beneficial for boundary-layer type problems, without grid stretching and satisfaction of mesh Reynolds number. Another challenging application could be employing such approach for problems involving sharp gradients and discontinuities (shock waves).

3. **Multi-component plasma:** The proposed method has wide ranging practical applications and one such area interest that has not be explored yet is multi-component plasma [76]. The methodology proposed by Parent et al.[77, 78] can be a good starting point due to its similarities to hyperbolic formulation.

APPENDICES

APPENDIX A

Verification of numerical methods

In this appendix, the following Euler equations for inviscid and compressible flows are computed to verify the numerical schemes presented in chapter-2.

$$\begin{aligned} \frac{\partial \rho}{\partial t} + \frac{\partial}{\partial x}\left(\rho u\right) &= 0, \\ \frac{\partial \rho u}{\partial t} + \frac{\partial}{\partial x}\left(\rho u^2 + p\right) &= 0, \\ \frac{\partial E}{\partial t} + \frac{\partial}{\partial x}\left(u\left(E + p\right)\right) &= 0, \end{aligned} \tag{A.1}$$

where ρ, u, p and E are the density, velocity vector, pressure, and total energy per unit volume respectively. The total energy per unit volume is given by,

$$E = \frac{p}{\gamma - 1} + \frac{\rho u^2}{2}, \tag{A.2}$$

where γ is the specific heat ratio of the gas.

A.1 One-dimensional test cases

First, Sod's shock-tube problem [79] is computed to verify the shock-capturing ability of MUSCL and WENO-5Z schemes. The initial conditions for the Sod problem are

given below.

$$(\rho, u, p) = \begin{cases} (0.125, \quad 0, \quad 0.1), & 0 < x < 0.5, \\ (1, \quad 0, \quad 1), & 0.5 < x < 1; \end{cases} \tag{A.3}$$

The ratio of specific heats γ is 1.4 and the computational domain is [-0.5,0.5]. In the test case, grid points are set to be 100 and the CFL number 0.5. Exact solution is computed on a grid size of 1000 points by exact Riemann solver [80]. Numerical results of the density, pressure, velocity and internal energy obtained from WENO-5Z and Generalized MUSCL schemes at time $t = 0.2$ are shown in Fig A.1. It can be seen that there are no overshoots at the contact discontinuities and WENO-5Z has less dissipation than MUSCL scheme as expected.

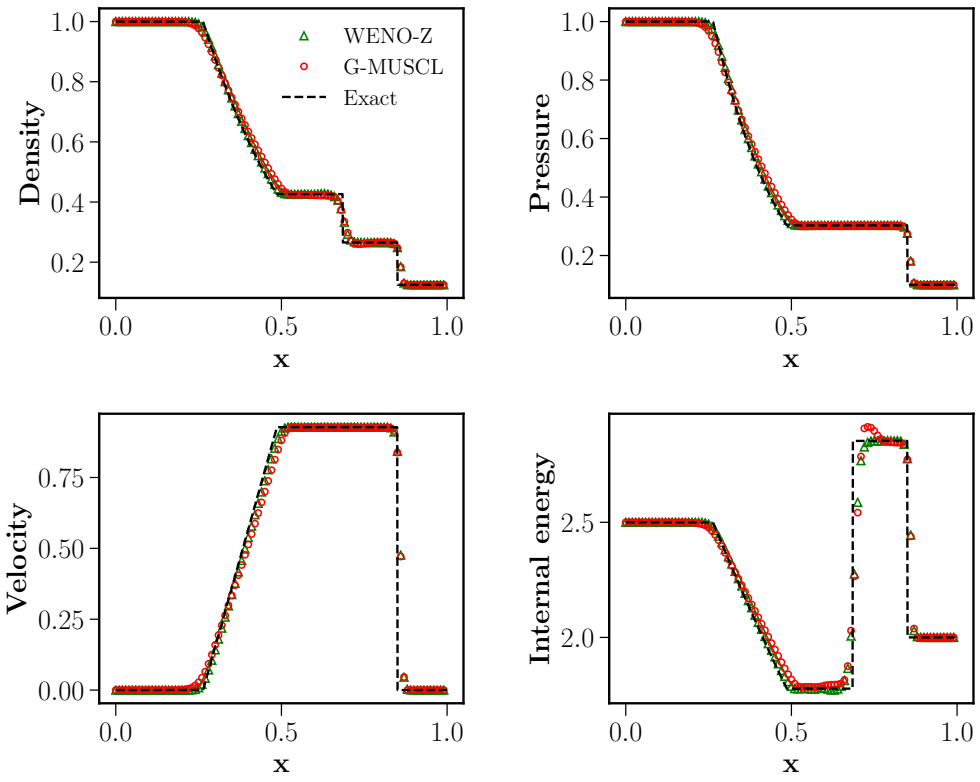

Figure A.1: Sod shock tube problem at $t = 0.2$ for WENO5-Z and Generalized MUSCL

Second, the Shu-Osher problem [81] is computed. The following initial data is considered,

$$(\rho, u, p) = \begin{cases} (3.857143, \quad 2.629369, \quad 10.3333), & -5 < x < -4, \\ (1 + 0.2\sin(5x), \quad 0, \quad 1), & -4 < x < 5, \end{cases} \tag{A.4}$$

with zero-gradient boundary conditions. This problem simulates the interaction of a right-moving Mach 3 shock with a perturbed density structure. Figure A.2 show the numerical results of the 5th-order WENO-5Z and WENO-JS schemes at time $t = 1.8$ with grids of $N = 200$. The "exact" solution is computed by WENO-CU6 [82] with a fine grid $N = 2000$. It is shown that all schemes give satisfactory approximations of the wavelike structures behind the shock. It can be observed that WENO-5Z has lower dissipation and resolves the wave phenomenon better than WENO-JS.

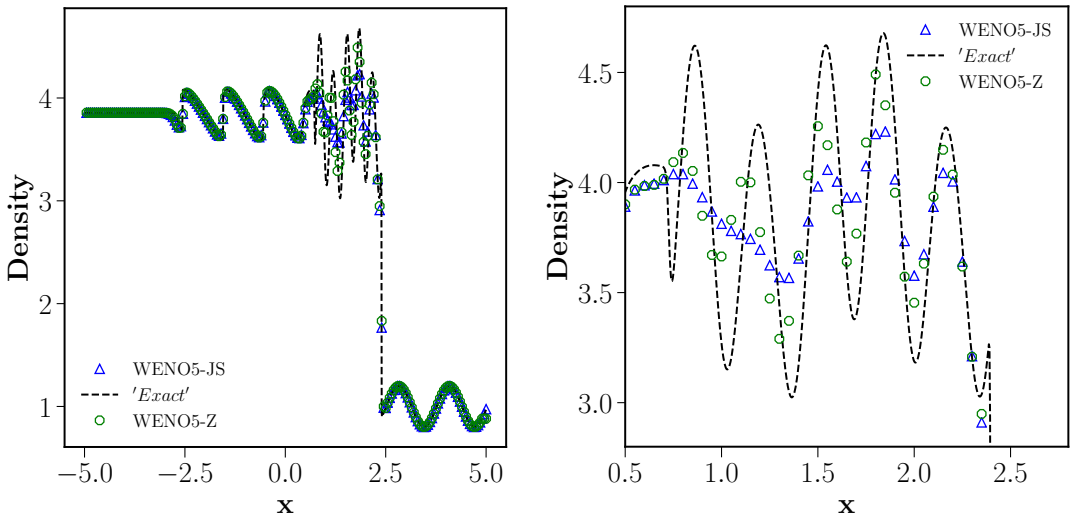

(a) Global density profile

(b) Local density profile

Figure A.2: Density distribution of the Shu-Osher problem: (a) Global profile and (b) enlarged figure for the post- shock region.

A.2 Two-dimensional test cases

In this section, two-dimensional numerical tests of WENO schemes are conducted to verify the resolution and robustness. All the simulations are carried out by Local Lax splitting approach. First, the double Mach reflection is investigated. The problem simulates the interaction of a shock wave of Mach number $M = 10$ with a wall at a 60 angle. The initial conditions for the problem are as follows,

$$(\rho, u, v, p) = \begin{cases} (8,\ 8.25\cos 30^0,\ -8.25\sin 30^0,\ 116.5), & x < 1/6 + \frac{y}{\tan 60^0}, \\ (1.4,\ 0,\ 0,\ 1), & x > 1/6 + \frac{y}{\tan 60^0}, \end{cases} \tag{A.5}$$

The initial and boundary conditions as same as that of Woodward and Collela [83] and the computation is conducted until t = 0.2, on a grid size of 960 240. At the bottom boundary, reflecting boundary conditions are used for $x \geq 1/6$ and the slip wall condition is imposed at $x \in [0, 1/6]$. The left boundary is set at the post-shock flow conditions and zero-gradient conditions are applied at the right boundary. Time-dependent boundary conditions are employed on the top boundary.

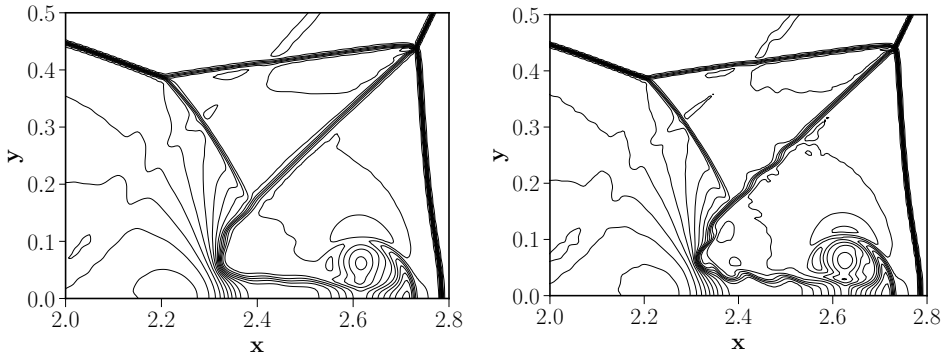

(a) WENO-JS (b) WENO-5Z

Figure A.3: 34 equally spaced contours of density at t = 0.2 for WENO-JS and WENO-5Z schemes in the blown-up region around the Mach stem.

In Fig.A.3, WENO-JS is too dissipative to produce any rolled-up vortices along

the slip line and the resolution is improved in WENO-5Z simulations.

Second, Rayleigh-Taylor instability, which occurs at an interface between fluids of different densities when an acceleration is directed from the heavy fluid to the light fluid, is computed. The objective of this test case is to show the feature of dissipation, with bubbles of light fluid rising into the ambient heavy fluid and spikes of heavy fluid falling into the light fluid and resulting in fingering like structure, in two dimensions. The initial conditions of Rayleigh-Taylor instability are [84]

$$(\rho, u, v, p) = \begin{cases} (2.0,\ 0,\ -0.025\sqrt{\frac{5p}{3\rho}\cos(8\pi x)},\ 2y+1), & 0 \le y < 0.5, \\ (1.0,\ 0,\ -0.025\sqrt{\frac{5p}{3\rho}\cos(8\pi x)},\ y+1.5), & 0 \le y \le 0.5, \end{cases} \tag{A.6}$$

and the computation is conducted until t = 1.95, on a grid size of 120 × 480.

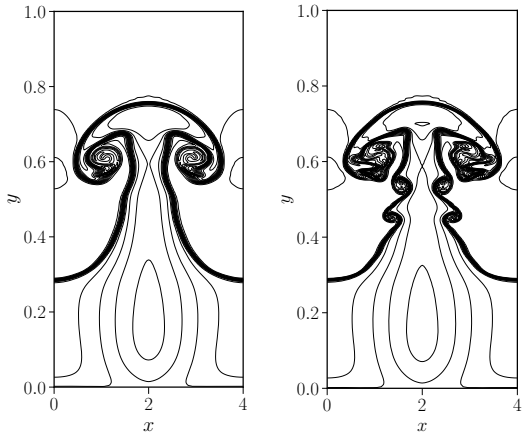

(a) WENO-JS (b) WENO-5Z

Figure A.4: Comparison of density contours obtained by WENO-JS and WENO-5Z on a grid size of 120 × 480.

Reflective boundary conditions are imposed on the right and left boundaries by ghost cells. The flow conditions are set to ρ=1, p=2.5, and $u = v$=0 on top boundary and ρ=2, p=1.0, and $u = v$=0 on bottom boundary. Figure A.4 indicates the density distribution of the Rayleigh-Taylor instability problem and it can be seen that WENO-5Z resolved the finer structures in comparison with WENO-JS.

BIBLIOGRAPHY

BIBLIOGRAPHY

[1] H. Nishikawa, First-, second-, and third-order finite-volume schemes for diffusion, Journal of Computational Physics 256 (2014) 791–805.

[2] H. Nishikawa, A first-order system approach for diffusion equation. I: Second-order residual-distribution schemes, Journal of Computational Physics 227 (1) (2007) 315–352.

[3] E. Lee, H. T. Ahn, H. Luo, Cell-centered high-order hyperbolic finite volume method for diffusion equation on unstructured grids, Journal of Computational Physics 355 (2018) 464 – 491.

[4] H. Nishikawa, A first-order system approach for diffusion equation. II: Unification of advection and diffusion, Journal of Computational Physics 229 (11) (2010) 3989–4016.

[5] H. Nishikawa, First, second, and third order finite-volume schemes for advection-diffusion, Journal of Computational Physics 273 (2014) 287–309.

[6] A. Mazaheri, H. Nishikawa, First-order hyperbolic system method for time-dependent advection-diffusion problems, NASA-TM–2014–218175.

[7] H. Nishikawa, Two ways to extend diffusion schemes to navier-stokes schemes: Gradient formula or upwind flux, 20th AIAA Computational Fluid Dynamics Conference 2011 (2011) 27–30.

[8] H. Baty, H. Nishikawa, Hyperbolic method for magnetic reconnection process in steady state magnetohydrodynamics, Monthly Notices of the Royal Astronomical Society 459 (1) (2016) 624–637. doi:10.1093/mnras/stw654.

[9] H. Nishikawa, Y. Liu, Hyperbolic advection-diffusion schemes for high-reynolds-number boundary-layer problems, Journal of Computational Physics 352 (2018) 23 – 51.

[10] H. Nishikawa, On hyperbolic method for diffusion with discontinuous coefficients, Journal of Computational Physics 367 (2018) 102–108.

[11] S. Braginskii, Transport processes in a plasma, Reviews of plasma physics 1.

[12] P. Perona, J. Malik, Scale-space and edge detection using anisotropic diffusion, IEEE Transactions on pattern analysis and machine intelligence 12 (7) (1990) 629–639.

[13] P. J. Basser, D. K. Jones, Diffusion-tensor mri: theory, experimental design and data analysis–a technical review, NMR in Biomedicine: An International Journal Devoted to the Development and Application of Magnetic Resonance In Vivo 15 (7-8) (2002) 456–467.

[14] R. Marchand, M. Dumberry, Carre: a quasi-orthogonal mesh generator for 2d edge plasma modelling, Computer Physics Communications 96 (2-3) (1996) 232–246.

[15] L. Degtyarev, S. Y. Medvedev, Methods for numerical simulation of ideal mhd stability of axisymmetric plasmas, Computer Physics Communications 43 (1) (1986) 29–56.

[16] S. Gnter, Q. Yu, J. Krger, K. Lackner, Modelling of heat transport in magnetised plasmas using non-aligned coordinates, Journal of Computational Physics 209 (1) (2005) 354 – 370.

[17] C. Sovinec, A. Glasser, T. Gianakon, D. Barnes, R. Nebel, S. Kruger, D. Schnack, S. Plimpton, A. Tarditi, M. Chu, et al., Nonlinear magnetohydrodynamics simulation using high-order finite elements, Journal of Computational Physics 195 (1) (2004) 355–386.

[18] B. van Es, B. Koren, H. J. de Blank, Finite-difference schemes for anisotropic diffusion, Journal of Computational Physics 272 (2014) 526–549.

[19] D. Kuzmin, M. Shashkov, D. Svyatskiy, A constrained finite element method satisfying the discrete maximum principle for anisotropic diffusion problems, Journal of Computational Physics 228 (9) (2009) 3448 – 3463.

[20] P. Sharma, G. W. Hammett, Preserving monotonicity in anisotropic diffusion, Journal of Computational Physics 227 (1) (2007) 123–142.

[21] L. Chacón, D. Del-Castillo-Negrete, C. D. Hauck, An asymptotic-preserving semi-Lagrangian algorithm for the time-dependent anisotropic heat transport equation, Journal of Computational Physics 272 (2014) 719–746. doi:10.1016/j.jcp.2014.04.049.

[22] M. Tang, Y. Wang, An asymptotic preserving method for strongly anisotropic diffusion equations based on field line integration, Journal of Computational Physics 330 (2017) 735–748. doi:10.1016/j.jcp.2016.10.062.

[23] J.-P. Boeuf, Tutorial: Physics and modeling of hall thrusters, Journal of Applied Physics 121 (1) (2017) 011101.

[24] K. Komurasaki, Y. Arakawa, Two-dimensional numerical model of plasma flow in a hall thruster, Journal of Propulsion and Power 11 (6) (1995) 1317–1323.

[25] J. M. Fife, Hybrid-pic modeling and electrostatic probe survey of hall thrusters, Ph.D. thesis, Massachusetts Institute of Technology (1998).

[26] I. G. Mikellides, I. Katz, Numerical simulations of hall-effect plasma accelerators on a magnetic-field-aligned mesh, Phys. Rev. E 86 (2012) 046703.

[27] H. C. Dragnea, K. Hara, I. D. Boyd, Development of a 2d axisymmetric electron fluid model in hall thrusters, in: 53rd AIAA/SAE/ASEE Joint Propulsion Conference, 2017, p. 4632.

[28] J. Geng, L. Brieda, L. Rose, M. Keidar, On applicability of the thermalized potential solver in simulations of the plasma flow in hall thrusters, Journal of Applied Physics 114 (10) (2013) 103305.

[29] R. Kawashima, K. Komurasaki, T. Schönherr, A hyperbolic-equation system approach for magnetized electron fluids in quasi-neutral plasmas, Journal of Computational Physics 284 (2015) 59 – 69.

[30] R. Kawashima, K. Komurasaki, T. Schönherr, A flux-splitting method for hyperbolic-equation system of magnetized electron fluids in quasi-neutral plasmas, Journal of Computational Physics 310 (2016) 202–212.

[31] P. L. Roe, Approximate riemann solvers, parameter vectors, and difference schemes, Journal of computational physics 43 (2) (1981) 357–372.

[32] A. Harten, P. D. Lax, B. van Leer, On upstream differencing and godunov-type schemes for hyperbolic conservation laws, SIAM Review 25 (1) (1983) 35–61.

[33] M.-S. Liou, A sequel to ausm, part ii: Ausm+-up for all speeds, Journal of computational physics 214 (1) (2006) 137–170.

[34] J. L. Steger, R. Warming, Flux vector splitting of the inviscid gasdynamic equations with application to finite-difference methods, Journal of Computational Physics 40 (2) (1981) 263 – 293.

[35] S. K. Godunov, A difference method for numerical calculation of discontinuous solutions of the equations of hydrodynamics, Matematicheskii Sbornik 89 (3) (1959) 271–306.

[36] B. Van Leer, Towards the ultimate conservative difference scheme. iv. a new approach to numerical convection, Journal of computational physics 23 (3) (1977) 276–299.

[37] G.-S. Jiang, C.-W. Shu, Efficient Implementation of Weighted ENO Schemes, Journal of Computational Physics 126 (126) (1995) 202–228.

[38] A. K. Henrick, T. D. Aslam, J. M. Powers, Mapped weighted essentially non-oscillatory schemes: Achieving optimal order near critical points, Journal of Computational Physics 207 (2) (2005) 542–567. doi:10.1016/j.jcp.2005.01.023.

[39] N. K. Yamaleev, M. H. Carpenter, A systematic methodology for constructing high-order energy stable WENO schemes, Journal of Computational Physics 228 (11) (2009) 4248–4272. doi:10.1016/j.jcp.2009.03.002.

[40] R. Borges, M. Carmona, B. Costa, W. S. Don, An improved weighted essentially non-oscillatory scheme for hyperbolic conservation laws, Journal of Computational Physics 227 (6) (2008) 3191–3211.

[41] S. Tan, C. W. Shu, A high order moving boundary treatment for compressible inviscid flows, Journal of Computational Physics 230 (15) (2011) 6023–6036.

[42] S. K. Lele, Compact finite difference schemes with spectral-like resolution, Journal of computational physics 103 (1) (1992) 16–42.

[43] S. Pirozzoli, Conservative hybrid compact-weno schemes for shock-turbulence interaction, Journal of Computational Physics 178 (1) (2002) 81 – 117.

[44] D. Ghosh, J. D. Baeder, Compact reconstruction schemes with weighted eno limiting for hyperbolic conservation laws, SIAM Journal on Scientific Computing 34 (3) (2012) A1678–A1706.

[45] Y. Guo, T. Xiong, Y. Shi, A positivity-preserving high order finite volume compact-weno scheme for compressible euler equations, Journal of Computational Physics 274 (2014) 505–523.

[46] X. Deng, H. Zhang, Developing High-Order Weighted Compact Nonlinear Schemes, Journal of Computational Physics 165 (1) (2000) 22–44.

[47] S. Zhang, S. Jiang, C. W. Shu, Development of nonlinear weighted compact schemes with increasingly higher order accuracy, Journal of Computational Physics 227 (15) (2008) 7294–7321.

[48] T. Nonomura, S. Morizawa, H. Terashima, S. Obayashi, K. Fujii, Numerical (error) issues on compressible multicomponent flows using a high-order differencing scheme: Weighted compact nonlinear scheme, Journal of Computational Physics 231 (8) (2012) 3181–3210.

[49] M. L. Wong, S. K. Lele, High-order localized dissipation weighted compact nonlinear scheme for shock- and interface-capturing in compressible flows, Vol. 339, Elsevier Inc., 2017. doi:10.1016/j.jcp.2017.03.008.

[50] T. Nonomura, N. Iizuka, K. Fujii, Freestream and vortex preservation properties of high-order WENO and WCNS on curvilinear grids, Computers and Fluids 39 (2) (2010) 197–214. doi:10.1016/j.compfluid.2009.08.005.

[51] X. Liu, S. Zhang, H. Zhang, C. W. Shu, A new class of central compact schemes with spectral-like resolution II: Hybrid weighted nonlinear schemes, Journal of Computational Physics 284 (2015) 133–154.

[52] T. Nonomura, K. Fujii, Robust explicit formulation of weighted compact nonlinear scheme, Computers and Fluids 85 (2013) 8–18.

[53] E. Johnsen, T. Colonius, Implementation of weno schemes in compressible multicomponent flow problems, Journal of Computational Physics 219 (2) (2006) 715–732.

[54] F. Jia, Z. Gao, W. S. Don, A spectral study on the dissipation and dispersion of the weno schemes, Journal of Scientific Computing 63 (1) (2015) 49–77.

[55] V. Titarev, E. Toro, Finite-volume weno schemes for three-dimensional conservation laws, Journal of Computational Physics 201 (1) (2004) 238 – 260.

[56] V. Coralic, T. Colonius, Finite-volume weno scheme for viscous compressible multicomponent flows, Journal of computational physics 274 (2014) 95–121.

[57] A. S. Chamarthi, Z. Wang, R. Kawashima, K. Komurasaki, Weighted nonlinear schemes for magnetized electron fluid in quasi-neutral plasma, in: 2018 AIAA Aerospace Sciences Meeting, 2018, p. 2194.

[58] B. Cockburn, S.-Y. Lin, C.-W. Shu, Tvb runge-kutta local projection discontinuous galerkin finite element method for conservation laws iii: one-dimensional systems, Journal of Computational Physics 84 (1) (1989) 90–113.

[59] H. Nishikawa, P. L. Roe, Third-order active-flux scheme for advection diffusion: Hyperbolic diffusion, boundary condition, and Newton solver, Computers and Fluids 125 (2016) 71–81.

[60] S. Tan, C.-W. Shu, Inverse lax-wendroff procedure for numerical boundary conditions of conservation laws, Journal of Computational Physics 229 (21) (2010) 8144 – 8166.

[61] Y. Morinishi, T. S. Lund, O. V. Vasilyev, P. Moin, Fully conservative higher order finite difference schemes for incompressible flow, Journal of computational physics 143 (1) (1998) 90–124.

[62] H. Nishikawa, Y. Nakashima, Dimensional scaling and numerical similarity in hyperbolic method for diffusion, Journal of Computational Physics 355 (2018) 121–143.

[63] J. W. Koo, I. D. Boyd, Modeling of anomalous electron mobility in hall thrusters, Physics of Plasmas 13 (3) (2006) 033501.

[64] A. J. Chorin, A numerical method for solving incompressible viscous flow problems, Journal of computational physics 2 (1) (1967) 12–26.

[65] E. Turkel, Preconditioning techniques in computational fluid dynamics, Annual Review of Fluid Mechanics 31 (1) (1999) 385–416.

[66] H. Nishikawa, P. Roe, Y. Suzuki, B. van Leer, A general theory of local preconditioning and its application to 2d ideal mhd equations, in: 16th AIAA Computational Fluid Dynamics Conference, p. 3704.

[67] S. Patankar, Numerical Heat Transfer and Fluid Flow, Series in computational methods in mechanics and thermal sciences, Taylor & Francis, 1980.

[68] H. Nishikawa, P. Roe, High-order fluctuation-splitting schemes for advection-diffusion equations, in: H. Deconinck, E. Dick (Eds.), Computational Fluid Dynamics 2006, Springer Berlin Heidelberg, Berlin, Heidelberg, 2009, pp. 77–82.

[69] C.-S. Chou, C.-W. Shu, High order residual distribution conservative finite difference weno schemes for convection–diffusion steady state problems on non-smooth meshes, Journal of Computational Physics 224 (2) (2007) 992–1020.

[70] H. Nishikawa, Y. Liu, Hyperbolic navier-stokes method for high-reynolds number boundary layer flows, in: 55th AIAA Aerospace Sciences Meeting, 2017, p. 0081.

[71] X. Zhang, C.-W. Shu, Maximum-principle-satisfying and positivity-preserving high-order schemes for conservation laws: survey and new developments, Proceedings of the Royal Society A: Mathematical, Physical and Engineering Sciences 467 (2134) (2011) 2752–2776. doi:10.1098/rspa.2011.0153.

[72] X. Zhang, C. W. Shu, On maximum-principle-satisfying high order schemes for scalar conservation laws, Journal of Computational Physics 229 (9) (2010) 3091–3120. doi:10.1016/j.jcp.2009.12.030.

[73] X. Y. Hu, N. A. Adams, C. W. Shu, Positivity-preserving method for high-order conservative schemes solving compressible Euler equations, Journal of Computational Physics 242 (2013) 169–180. arXiv:1203.1540, doi:10.1016/j.jcp.2013.01.024.

[74] D. S. Balsara, A two-dimensional HLLC Riemann solver for conservation laws: Application to Euler and magnetohydrodynamic flows, Journal of Computational Physics 231 (22) (2012) 7476–7503. arXiv:0911.1613, doi:10.1016/j.jcp.2011.12.025.

[75] D. S. Balsara, M. Dumbser, Divergence-free MHD on unstructured meshes using high order finite volume schemes based on multidimensional Riemann solvers, Journal of Computational Physics 299 (2015) 687–715. doi:10.1016/j.jcp.2015.07.012.

[76] S. T. Surzhikov, J. S. Shang, Two-component plasma model for two-dimensional glow discharge in magnetic field, Journal of Computational Physics 199 (2) (2004) 437–464.

[77] B. Parent, M. N. Shneider, S. O. Macheret, Generalized Ohm's law and potential equation in computational weakly-ionized plasmadynamics, Journal of Computational Physics 230 (4) (2011) 1439–1453. doi:10.1016/j.jcp.2010.11.012.

[78] B. Parent, M. N. Shneider, S. O. Macheret, Sheath governing equations in computational weakly-ionized plasmadynamics, Journal of Computational Physics 232 (1) (2013) 234–251. doi:10.1016/j.jcp.2012.08.011.

[79] G. A. Sod, A survey of several finite difference methods for systems of nonlinear hyperbolic conservation laws, Journal of computational physics 27 (1) (1978) 1–31.

[80] E. Toro, Riemann Solvers and Numerical Methods for Fluid Dynamics: A Practical Introduction, Springer Berlin Heidelberg, 2009.

[81] C. W. Shu, S. Osher, Efficient implementation of essentially non-oscillatory shock-capturing schemes, Journal of Computational Physics 77 (2) (1988) 439–471. doi:10.1016/0021-9991(88)90177-5.

[82] X. Y. Hu, Q. Wang, N. A. Adams, An adaptive central-upwind weighted essentially non-oscillatory scheme, Journal of Computational Physics 229 (23) (2010) 8952–8965. doi:10.1016/j.jcp.2010.08.019.

[83] P. Woodward, P. Colella, The numerical simulation of two-dimensional fluid flow with strong shocks, Journal of Computational Physics 54 (1) (1984) 115–173. arXiv:arXiv:1011.1669v3, doi:10.1016/0021-9991(84)90142-6.

[84] C. Gardner, J. Glimm, O. McBryan, R. Menikoff, D. Sharp, Q. Zhang, The dynamics of bubble growth for rayleigh–taylor unstable interfaces, The Physics of fluids 31 (3) (1988) 447–465.